UNIVERSITÀ
DEGLI STUDI
DI PADOVA

Università degli Studi di Padova

Department of Chemical Sciences

PhD courses in: Scienza ed Ingegneria dei Materiali e delle Nanostrutture (XXXIV)

Cu-activated poly cationic oxides as catalysts for sustainable development: from energy conversion to abatement of pollutants, from *ex situ to in situ* preparation

Coordinator: Prof. Giovanni Mattei

Supervisor: Prof. Antonella Glisenti

PhD Student: Giovanni Carollo

Table of Contents

Abstract

"What did you ask at school today?"

R. P. Feynman

The constant rise of global energy demand will lead to an inevitable increase of pollutants spilled into the atmosphere, if we do not change the strategy to transform energy moving towards a cleaner way. This work will illustrate three possible ways to overcome the energy demand and air pollution problem will be illustrated. In particular, the focus will be on Three Way Catalysts (TWC), Solid Oxide Cell (SOC), and Water Gas Shift Catalyst (WGS). The basic idea is to keep an open-minded approach: Three Way Catalysts are greatly relevant because at the present moment a significant part of pollution derives from transportation. Electric or hydrogen fuelled vehicles are not of rapid application or diffusion: natural gas or gasoline or diesel-based vehicle will continue to be the main way for people and goods transportation and until a revolutionary change, noble metals will be fundamental for TWC. In a medium-range vision, Solid Oxide Cells (Fuel Cells and Electrolysers) can be a very valuable opportunity to convert and store energy in an efficient, safe, and economic way. Finally, if we look further away the sustainable production of hydrogen from water will be a winning strategy.

Chapter 1 of this thesis is devoted to explaining and showing all the technologies and scientific ideas behind the motivation that drive the choices I made during my Ph.D.

Chapter 2 will be presented the characterization methodology used to study all the materials synthesized: spinels based on Cu and Fe with different aluminium doping, perovskites based on La and Fe nano decorated with copper.

Chapter 3 and Chapter 4 will be dedicated to the 6 months spent at the Paul Sherrer Institut (PSI) under the supervision of Dr. Davide Ferri. The materials were characterized more exhaustively with *in situ* XRD and X-ray Absorption Spectroscopy (XAS) using the Swiss Light Synchrotron (SLS). Eventually, the catalysts were tested for Water Gas Shift Reaction and Three-Way Catalysis reaction evaluating the dependency of aluminium content in the spinel system and copper activation in the perovskite system. The foundations and the questions that will drive this research are: "*are pulses conditions useful to activate the catalyst in TWC application?*"" and "*initial synthesis of the catalyst is crucial to provide the desired properties, or it is only the combination of synthesis and reaction process that is possible to achieve what is wanted?*"

Chapter 5 will present the spinels that stand out from the WGSR process and are tested as Fuel Electrode for SOC application. From the preparation of the button cells to the electrochemical process involved.

Eventually Chapter 6 showcases, the possibility that some cobalt perovskites seem to display to change their crystallographic structure under specific conditions, in function of A-site doping with different concentration of Sr and B-site doping with Fe. The data were recorded at the European Synchrotron Radiation Facilities (ESRF) at the beamline ID15.

Introduction

"To infinity, and beyond!"

Buzz lightyear

1.1 Overview

The transition towards higher shares of renewable energies will simplify achieving access to clean and affordable energy, reducing the total amount of greenhouse gases emission and limiting the usage of fresh water in thermal power plant [1]. Renewable energy sources (hydro, wind, solar, geothermal, biofuels) have been proposed as a possible and partial solution to meet the constantly growing energy demands and to spread electricity over less developed countries. During 2019, only 27% of the total global electricity was provided from renewable sources. Thanks to cost reductions, renewable electricity is increasingly cost-competitive with conventional thermal power plants: in some regions, renewable energy cost is lower than running costs of existing fossil and nuclear power plants [2], and solar photovoltaics has emerged as the least-cost source of electricity production in the history of mankind. In the heat sector, a similar tendency is observed: about 10% of the heat used worldwide in 2019 was produced from sustainable sources, including renewable electricity. Based on a wide-ranging set of assumptions, methods, and targets from a global perspective [3], various energy scenarios have tried to project the future transition of energy systems. Most of the global energy transition studies present pathways that result in CO_2 emissions even in 2050. The diffusion of technology for renewable energy is slowed down by their intrinsic intermittent energy production [4]. Consequently, electricity storage has strategic importance.

Changing the ways to transform energy from not renewable to renewable sources is necessary for air pollution. The greenhouse effect is the most influential problem that we have to face, from now, to the next years to come [5]. Svante Arrhenius was the first man to quantify how CO_2 in the atmosphere can increase ground temperature [6]. It was not until

1901 that the atmosphere was compared to a greenhouse, a definition we owe to Swedish meteorologist Nils Ekholm [7]. Molecules that compose the atmosphere can absorb solar radiation and this is the very simple mechanism that governs the greenhouse effect. The primary greenhouse gases in Earth's atmosphere are water vapor (H_2O), carbon dioxide (CO_2), methane (CH_4), and nitrous oxide (N_2O). Without greenhouse gases, the average temperature of Earth's surface would be about −18 °C rather than the present average of 15 °C. The relative concentrations are extremely important for these gases and just a few changes in the total percentage may lead to severe and dramatic modification of the environment, as we know.

The constant rise of global energy demand will lead to an inevitable increase of pollutants spilled into the atmosphere, if we do not change the strategy to transform energy moving toward a cleaner way. In the following part of the Introduction, the three possible ways adopted in this thesis to overcome the energy demand and air pollution problem will be illustrated. In particular, the focus will be on Three Way Catalysts (TWC), Solid Oxide Cell, and Water Gas Shift Catalyst. The basic idea Is to keep an open mind approach: Three Way Catalysts are greatly relevant because at the present moment a significant part of pollution derives from transportation: electric vehicles or hydrogen fueled ones are not of rapid application or diffusion: natural gas or gasoline or diesel-based vehicle will continue to be the main way for persons and goods transportation and until a revolutionary change, noble metals will be fundamental for TWC. This requirement can affect the competitiveness and Independence of European Industries and the Economy. The first contribution to sustainable mobility can be the development of more efficient, low-cost, Critical Raw Materials-free catalysts. It deserves to be considered that a catalytic system In TWC works in harsh conditions and thus the catalysts developed for this application can easily be applied to

stable production plants. In a medium-range vision, Solid Oxide Cells (Fuel Cells and Electrolysers) can be a very valuable opportunity to convert and store energy in an efficient, safe, economic way. Finally, if we look further away the sustainable production of hydrogen from water will be a winning strategy. So the final part of the thesis will consider new materials to make possible the dream of obtaining hydrogen from water cleanly and efficiently.

1.2 Solid Oxide Cell

Fuel cells are great tools in helping the task of reducing the environmental impact of our energy sources. Very briefly, a fuel cell is an electrochemical device that can transform chemical energy into electrical energy. As a battery, a more mainstream apparatus, a fuel cell has a cathode and anode separated by a non-electrical conductor, the electrolyte. Unlike batteries, the fuel cell system can operate endlessly by the continuous fresh reactants that reach the electrodes. Very important, a fuel cell is not a closed system due to the continuous mass exchange with the environment. So, the only limitation is the depletion and degradation of the electrodes and electrolytes. A scheme of a fuel cell is presented in Figure 1, representing a Solid Oxide Cell (SOC), which is the type of cell studied during this thesis.

Their very peculiar characteristic is the presence of a solid electrolyte that needs a high temperature (600-900 ºC) to conduct the ions through them.

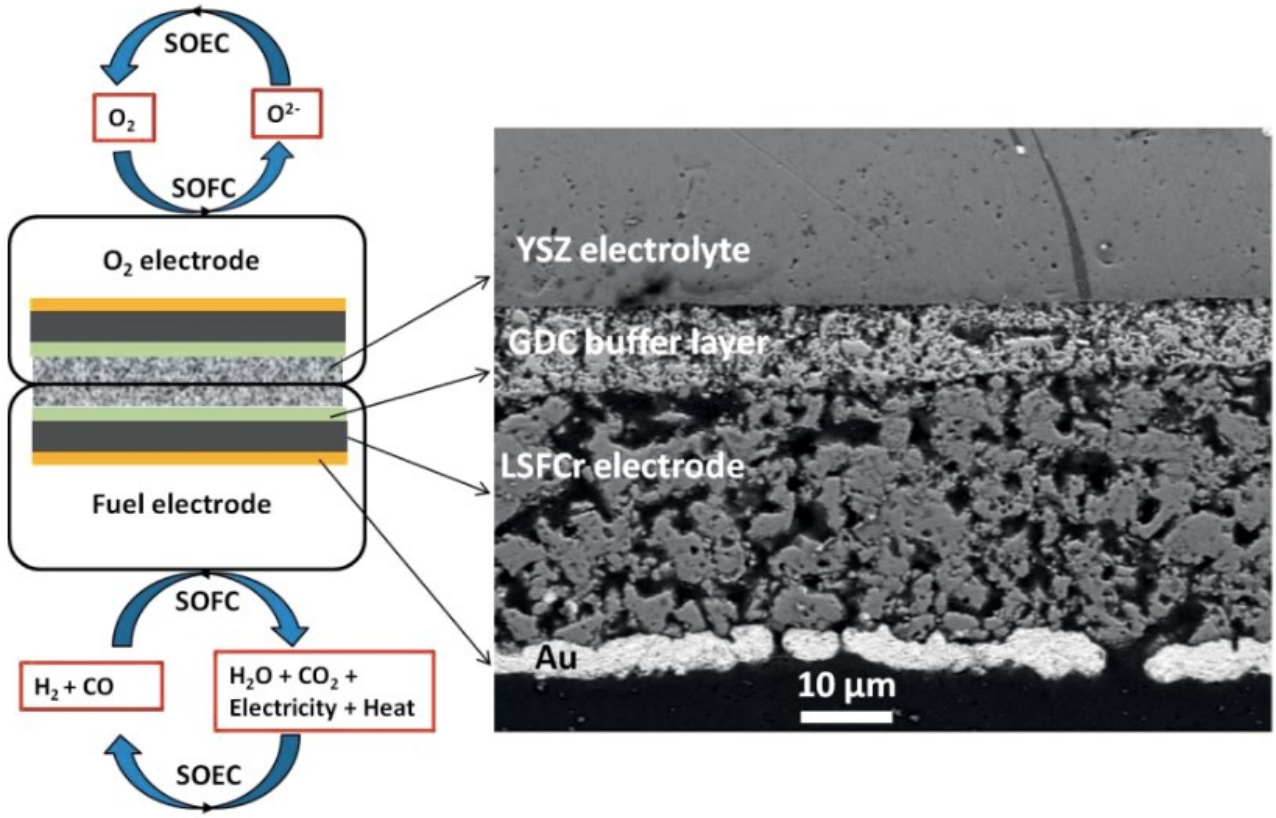

Figure 1 Left: Scheme of a SOC operating as Fuel Cell or Electrolyzer.

Right: Scanning electron microscopy image of a real SOC. [8]

The operative function of a SOC is very simple:

- Fuel cell mode: hydrogen at the fuel electrode is oxidized, oxygen at the O_2 electrode is reduced and the circuit is closed by the oxygen ions moving, through the electrolyte, from the fuel to the O_2 electrode.

- Electrolyser mode: water (and/or CO_2) molecules are reduced at the fuel electrode, gaseous oxygen forms at the O_2 electrode, and the circuit is closed by the oxygen ions going through the electrolyte from the fuel to the O_2 electrode.

So oxidized hydrogen form water that is expelled as a product, if we operate the cell as a Fuel Cell; quite the opposite occurs during the Electrolyser mode, where pure H_2 and O_2 form from water.

Solid Oxide Cells are electrochemical devices, so they are not bounded by thermodynamical limits expressed by Carnot's law. The real efficiency depends on the architecture of the cell and by the material optimization but never goes below 60%. As said before, hydrogen is the main fuel (or product) and it is considered the cleanest vector due to its oxidized form, water. Unfortunately, due to its very low weight, hydrogen in gaseous form (H_2) is not available on Earth and the quickest way to produce it, is from the reforming of fossil fuel. In any case, the combined efficiency of a reforming process and a SOC, is higher than using a plain and flavorless combustion route. So, Fuel Cell, indeed, configures, also in terms of fuel versatility, transportation, sustainability, as a valuable and rapid way to contribute to the solution of environmental problems.

1.2.1 Fuel Cell thermodynamics

The reaction that governs a Fuel Cell using hydrogen as combustible is very simple:

$$2\,H_2 + O_2 \rightarrow 2H_2O$$

For any reaction, from the enthalpies of formation of the reactants and products is possible to calculate the heat enthalpy.

$$\Delta_r H^{\ominus} = \Delta_f H^{\ominus}_{liquid}(H_2O) - 1/2\ \Delta_f H^{\ominus}(O_2) - \Delta_f H^{\ominus}(H_2) = -286\ kJ/mol$$

The negative sign resulting from the previous equation indicates the exothermic nature of the reaction, which is expected to be combustion. In the same way, it is possible to determine the standard entropy of formation.

$$\Delta_r S^{\ominus} = S^{\ominus}_{liquid}(H_2O) - 1/2\ \ S^{\ominus}(O_2) - S^{\ominus}(H_2) = -0.1633\ kJ/(mol\ K)$$

And, to complete the sequence, the free Gibbs energy:

$$\Delta_r G^{\ominus} = \Delta_r H^{\ominus} - T\Delta_r S^{\ominus} = -237.34\ kJ/mol$$

It is possible to imagine the entropy as a figure of how much of the free Gibbs energy is irreversibly lost and, considering this, to calculate a first efficiency of the cell. The ratio connecting enthalpy and Gibbs free energy is called Gibbs efficiency.

$$\eta_G(25°C) = \Delta rG^{\ominus}/\ \Delta rH^{\ominus} = 0.83$$

As an example, purely theoretical, the efficiency of a fuel cell at 25 ºC.

In view of the fact that $-\Delta_r G = nFE$, it is possible to calculate the standard electromotive force:

$$\Delta_{rev}E\ (25°C) = -\Delta rG^{\ominus}\ /\ \mathrm{nF} = 1.23\ \mathrm{V}$$

With temperature, reaction enthalpy, and reaction entropy change. Their variation is related to the heat capacities of the chemical species.

$$\left(\frac{\partial \Delta_r H^{\ominus}}{\partial T}\right)_p = \Delta_r C_p \quad \left(\frac{\partial \Delta_r S^{\ominus}}{\partial T}\right)_p = \frac{\Delta_r C_p}{T}$$

And the variation of the free Gibbs energy:

$$\left(\frac{\partial \Delta_r G^{\ominus}}{\partial T}\right)_p = \Delta_r S^{\ominus}$$

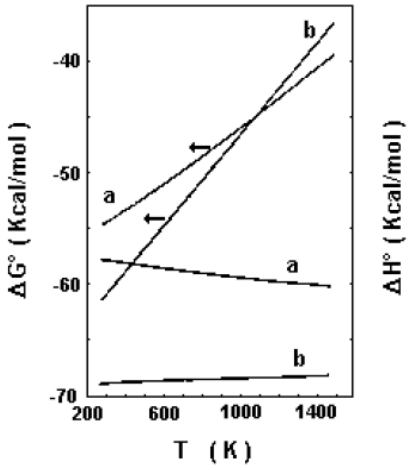

Figure 2 Variations of standard free Gibbs energy and enthalpy depending on temperature for oxidation: H_2 (a) , CO (b)

In Figure 2 is showed how thermodynamical functions for H_2 vary with the temperature up to 1200 ºC. Considering the general view, free Gibbs energy increases, and the enthalpy barely decreases.

The second parameter of efficiency that it is possible to determine is its behavior as a function of voltage, or potential. The Open Circuit Voltage (OCV) or Open Circuit Potential (OCP) is the potential calculated in ideal conditions. The ratio between the actual OCV of a cell and the ideal one defines the voltage efficiency:

$$\eta_V = \frac{\Delta V}{\Delta_{rev} E}$$

The loss of potential can be described by internal resistances of the cell:

$$R_{tot} = R_0 + R(i)$$

R_o is independent from the current intensity, quite the opposite for R(i).

If it is plausible to neglect R(i) by comparison to R_o, is possible to express the voltage loss in form of R_o x I:

$$\eta_V = \frac{\Delta_{rev} E - R_0 I}{\Delta_{rev} E} = 1 - \frac{R_0 I}{\Delta_{rev} E}$$

From a practical point of view, the biggest resistance R_o, can be related to the resistance of the electrolyte. R(i) is the activation polarization and is evident only when the fuel cell is operating near voltage as its OCP. At small values, it can be possible to represent overpotential using the Tafel equation:

$$\eta = b \cdot ln \frac{i}{i_0}$$

In the last equation, is fundamental to recognize the nomenclature change, where η represents the overpotential and not efficiency. The values of the two currents are respectively *i* the current and i_o the exchange current. The parameter *b* derives from the well-known Butler-Volmer equation and can be expressed as:

$$b = \frac{RT}{\alpha nF}$$

R is the universal gas constant, T temperature expressed in K, F is the Faraday constant, n number of electron exchange and α the charge transfer coefficient. Analyzing the last equation, R and F are constants, T is determined from experimental condition and α is the only factor influenced by the cell itself. More specific, from the material and thus from the catalytic performance of the electrodes. The nature of the electrodes can also influence i_o so an electrode able to fast electrons or ions transport, ergo high exchange current, avoids high loss of efficiency.

The last efficiency discussed in this thesis, concern the fuel consumption. It is defined as the ratio of the fuel the cell is fed with and the real fuel consumption. Now is possible to define an overall efficiency as the product of all three efficiencies listed so far.

1. Gibbs efficiency,
2. Voltage efficiency,
3. Fuel consumption.

Without a clear knowledge of thermodynamics, it could be apparent that high temperature is permanently detrimental due to the Gibbs efficiency. For our fortune, the temperature is, one more time, hidden also in the voltage efficiency: from a general point of view, activation processes are easier (no need of noble metals) and in general internal resistances are lower (O^{2-} diffusion).

1.2.2 Solid Oxide Cells materials

Solid oxide cells are cell characterized by having ceramic materials with a solid electrolyte Figure 1. The operating temperature is between 700 ºC and 1000 ºC and mostly, as we will see next, depends on the nature of the electrolyte.

As mention before, the system can both work in Fuel Cell mode or Electrolyzer mode [9]. In Fuel Cell mode, oxygen is reduced at the O_2 electrode and incorporated into the crystalline lattice of the electrolyte. The ions journey toward the anode, can be possible thanks to the hopping mechanism where the O^{2-} jumps from vacancy to vacancy [10]. The oxygen ions, with their double negative charge, are extremally bulky: this is the main reason of why is needed such high operative temperature. There are Solid Oxide Cell where the transported ions through the electrolyte is the smaller H^+ [11]. Sadly, those type of cell are still facing the stability problem [12]. The semi-reactions at the electrodes are the following:

$2H_2 + 2O^{2-} \rightarrow 2H_2O + 4e^-$ (Fuel Electrode)

$O_2 + 4e^- \rightarrow 2O^{2-}$ (O_2 Electrode)

Thanks to the remarkable high working temperature and their intrinsic robustness, Solid Oxide cells can work with different fuel, both in Fuel Cell mode as Electrolyzer mode. The most commons fuel can be hydrocarbons [13] [14] [15] (e.g. methane, methanol, heavier hydrocarbon, etc.) or ammonia [16] [17].

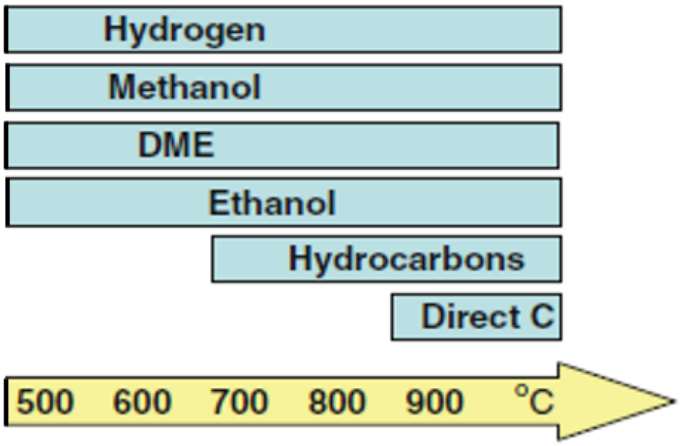

Figure 3 Fuel flexibility of Solid Oxide Cell in Fuel Cell mode.

Mechanical stability is a problem due of the high temperatures. SOC can be made only of ceramic materials, whose mechanical properties are modest [16]. In particular, ceramics are brittle and when subjected to mechanical stress, cracks may lead to the complete failure of the system. One of the main factors to consider is the different Thermal Expansion Coefficient (TEC) of the cell components. Commercial SOCs are engineered towards the more accurate uniformity of the TEC possible, in order to minimizes stresses. The choice of which cell component provides mechanical support is critical and early cells used a supporting thick electrolyte. This geometry provides the fastest and easily fabrication. It is possible to press some electrolyte powder into a die to form a pellet and sinterized it at high temperature; then, the two electrodes are deposited on the sides of the electrolyte. From Figure 1, is possible to see a dense layer: the electrolyte. This geometry is able to provide

extreme mechanical stability. Regrettably, an electrolyte supported cell has a tremendous drawback: for the cell efficiency, the electrolytic layer is a purely resistive element, so its resistance is directly proportioned to its thickness.

The easiest and more industrial approach to reduce the thickness of the electrolyte is to allocate the mechanical support to another layer: an anode supported Fuel Cell is the result. In any case, the anode is a catalytic layer which interacts with the gas phase and must, consequently, be porous. The thickness and porosity of the anode are then a compromise between the mechanical properties and a sufficient gas diffusion. A common way to produce the anode involve two stages: the anode powder is pressed to secure a thick substrate able to provide mechanical support, successively, the electrochemically functional anode layer, more porous, is deposited. The anode, then, is subject to a first sintering process. A layer of dense electrolyte is deposited, and the cell is fired again. The final deposition is done for the cathode, on the other side of the electrolyte and the cell is cooked a last time [18]. A supporting cathode is theoretically possible, but this is not the optimal choice due to the slow reaction speed, and significant decrease of the cell power.

The search for new and cheap materials able to meet the needs of SOCs is of extreme importance to improve and sustain their commercialization. From an industrial point of view, two different approaches are used to enhance the efficiency of a SOC. First, which is preferred in SOC cermet-based Fuel electrode, consists in maximizing the three phase boundaries (TPB) area using different approaches of synthesis and nano-decoration. Second, which seems more actable, is the use of mixed ionic electron conducting (MIEC) electrode. The use of mixed ionic electron conducting electrode allows an extraordinary enhancement of the active area. In this way the electrochemical reactions and the oxygen ion can take part in the whole surface of electrode.

The TPB is the site where ions, electrons and gas molecules must be in contact simultaneously. The phenomenon was observed for the first time in 1920s by Alfred Schmidt. In the state-of-the-art materials, as Ni-YSZ cermet, where nickel is only electronic conductors and YSZ (Yttria Stabilized Zirconia) is pure ionic conductor, the electrochemical reactions occur only at the intersection of them. The gas presence and adoption to these intersections is fundamental to permit the electrochemical processes. In Figure 4 is reported the proposed mechanism for the TPB in a O_2 electrode.

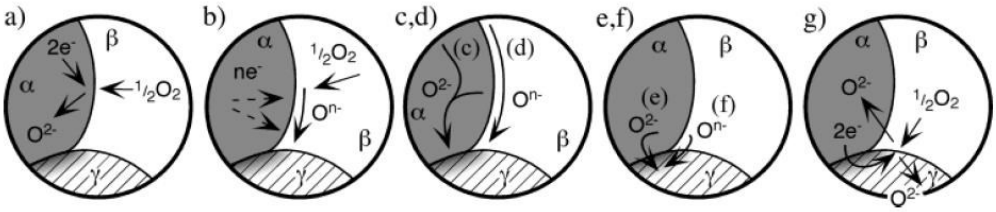

Figure 4 TPB mechanisms for oxygen reaction in a SOFC cathode. α is the cathode, β is the gas phase and γ is the electrolyte. From [19]

TPB-based layers are extensively present in many Fuel electrodes and O_2 electrodes with good results. The main drawback is where the electrochemical reactions take act, namely only in the restricted TPB region. This limit can be solved, just partially, improving the microstructure of electrodes using technique as infiltration [20] or nano-decoration [21]. A more elegant solution to this problem is the use of mixed ion-electron conductors (MIECs). These marvelous materials present electronic and ionic conductivity by default, as an intrinsic characteristic lead by the *ad hoc* design. This peculiarity allows to overcome the limit of three boundaries phase. In so doing, the material active sites significantly increases and the whole surface can be a potential candidate site for the reaction. The mixed ion conductor feature may enhance the electrochemical reaction on the electrode surface so avoiding the problems of gas diffusion thought the porous electrode [22].

Electrolyte materials

Commercial SOCs employ YSZ (Yttria Stabilized Zirconia) as electrolyte and, even if this material is being used from the early stage of SOC technology, it is still on top and far from being obsolete. It has a decent ionic conductivity, and zero electronic conductivity. YSZ is the industrial favorite because it is cheap, and its components are abundant. Zirconium Oxyde (ZrO_2) face two phase transitions during heating: from monoclinic to tetragonal at 1170°C and from tetragonal to cubic (fluorite) at 2370°C. The addition of yttria stabilizes the fluoritic structure also at lower temperatures, necessary for SOC application. The presence of yttria, also generates oxygen vacancies in the crystalline structure, which are fundamental for the ionic conduction, according to the reaction:

$$Y_2O_3 \rightarrow 2\,Y'_{Zr} + 3\,O_O^x + V_O^{\cdot\cdot}$$

The stabilization with scandium instead of yttrium further improves conduction. The reason is the very similar radius between Sc^{3+} and Zr^{4+}. Sadly, this system possesses a high amount of ordered and metastable phases that lead to instability [23]. Another reason to discourage scandium use, is the cost far higher compared to yttrium and insufficient abundance. Because of this, YSZ is still the most used electrolyte material in SOCs.

Ceria is another oxide with fluoritic structure. Oxygen vacancies in ceria are generated from the natural presence of Ce^{3+} and Ce^{4+}. Anyway, analogously with zirconia, the doping with proper metal cation can boost the oxygen vacancies. The most common substitution is with gadolinium, to form Gadolinium Doped Ceria (GDC).

$$Gd_2O_3 \rightarrow 2\,Gd'_{Ce} + 3\,O_O^x + V_O^{\cdot\cdot}$$

In high oxygen partial pressure GDC is a pure ionic conductor, but Ce^{4+} is easily reduced to Ce^{3+} when oxygen partial pressure decreases. This peculiar characteristic brings to the conclusion that the material can be an electronic conductor. The presence of electronic conduction is an enormous drawback, due to the possible short-circuits of the electrodes, to the decrease of available potential and therefore general efficiency. For this reason, cells with ceria electrolyte should not be operated at temperatures above 600°C [24].

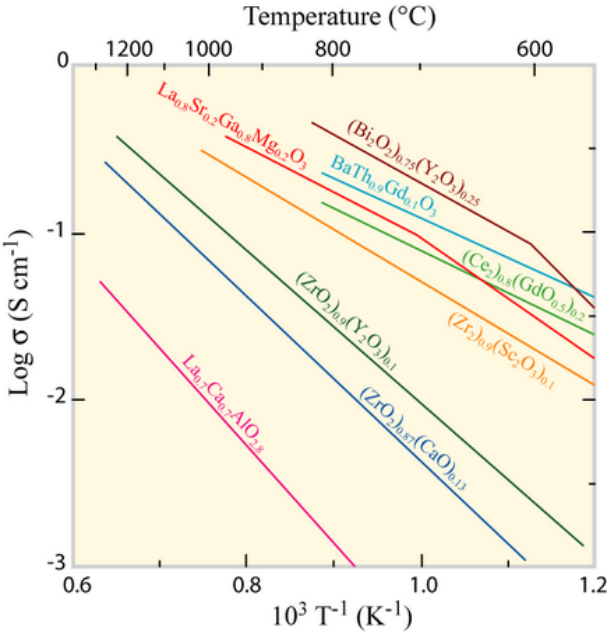

Figure 5 Ionic conductivity of different materials used as electrolyte [25]

Fuel electrode materials

SOCs need high temperature for their function, so noble metals to catalyze reactions are not essentials. The standard Fuel electrode catalyst is nickel, which is not expensive and show

good activity in SOC application. This electrode is in form of a cermet: nickel particles are mixed with the ceramic matrix made of the same material of the electrolyte (e.g. YSZ). Its preparation begins with the mixing of NiO and YSZ, normally in the ratio 40:60 (Ni:YSZ) and then the powder is used to prepare the Fuel electrode. The reduction from NiO to Ni is made using wet or dry hydrogen, during the warming-up procedure. The Fuel electrode must be an electronic conductor, so the metallic part (e.g. Ni) amount must be enough to allow electronic percolation in the entire volume of the cermet. Besides, nickel works as a catalyst, so its superficial area is extremely essential. Thus, an excessive concentration of Ni would lead to the formation of bigger agglomerate with loss of superficial area. The particles size of the YSZ powder is very important to obtain an appropriate porosity. Porosity must be adequate to allow an easy gas diffusion inside the electrode, but an excess of it, could cause a difficult electronic percolation pathway. Ni cermet anodes do not possess mixed conductivity, so the building of the three-phase boundary must be calculated meticulously. For a Ni cermet electrode, it is good to have TPBs as large as possible. So, Ni cermets are very complicated systems, in which a lot of parameters can be varied, affecting several characteristics of the final material. The classical material Ni/YSZ cermet, has been studied and several reports are available. [26] [27]. Even if nickel cermet Fuel Electrode are the standard for current SOCs, they have some drawbacks. At 800°C, metallic nickel has a $16 \cdot 10^{-6}$ K^{-1} TEC [28], while YSZ has 10 K^{-1} [29]. Nickel particles are subjected to slow degradation due of the sintering of Ni particles that leads to progressive loss of surface area (thus, also TPB is lost), and fast more disruptive degradation overdue to RedOx cycles [30] (Figure 6). Nickel tends to be poisoned by carbon during the oxidation of organic compounds. The process is irreversible if the Fuel electrode is always under critical reducing environment; this relegates the SOCs practically to the only use of hydrogen as fuel because hydrocarbons or

other C-containing molecules, would lead to the electrode deactivation. This is probably the biggest drawback of nickel as Fuel electrode. Just as reminder, the nomenclature SOC comprehend Fuel Cell mode and Electrolyzer and the cermet Ni/YSZ works fine with both the modality.

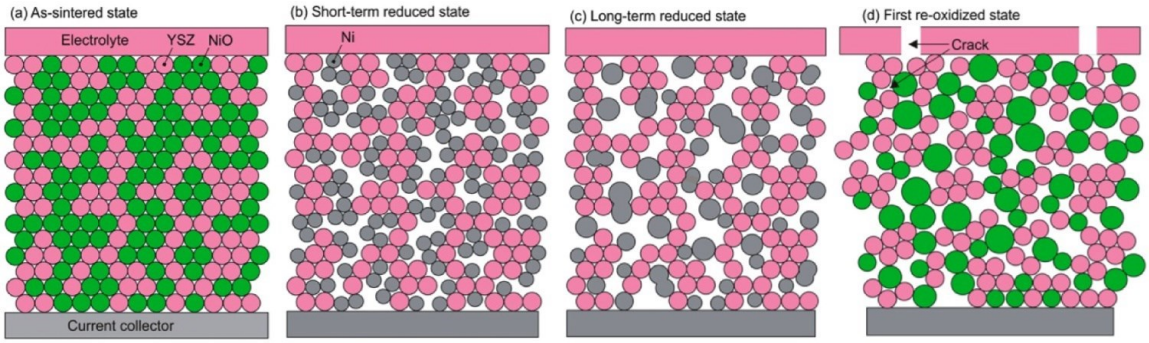

Figure 6 Coarsening and expansion of Ni in a cermet following a RedOx cycle [30].

O_2 electrode materials

The O_2 electrode is the place where oxygen reduction is performed. Like the Fuel electrode, this part of a SOC must achieve many features: good activity concerning the oxygen reduction, remarkable electronic conduction, chemical compatibility with the electrolyte and a suitable thermal expansion. Lanthanum strontium manganites $(La_{1-x}Sr_x)MnO_3$, (LSM) were the first materials studied due to their fine activity and optimal compatibility with YSZ [31]. LSM has a good electronic conductibility but has a weak ionic conductibility. Because of this, LSM must be mixed with a good ion conductor and normally it is the electrolyte used in the SOC. As for the cermet anode, also the LSM/YSZ cathode suffers from three phase boundaries limit. New promising materials have been developed paying particular attention to the limitation from the cermet LSM/YSZ: $(La_{1-x}Sr_x)CoO_3$ (LCF), $(La_{1-x}Sr_x)FeO3$ (LSF) and $(La_{1-x}Sr_x)(Co_{1-y}Fe_y)O_3$ (LSCF) [32]. The innovative characteristics of these new materials are mainly focused on two aspects: the ability to be electrocatalytically really more active than

LSM and the possibility to operate as MIEC, solving the limitation due the TPB. Despite this, all lanthanum and strontium containing electrodes, suffer of reactivity toward YSZ: $La_2Zr_2O_7$ and $SrZrO_3$ are formed at the interface creating insulating phase. The use of LSF, LSC and LSCF with YSZ electrolyte is compulsory coupled with an interlayer of gadolinium doped ceria [33].

1.2.3 Therefore, why SOC?

The electrochemical part of this thesis, related to SOCs world, will be present in Chapter 5. The materials designed and synthesized during my PhD, presented in Chapter 3, will be finally adopted as Fuel Electrodes in a device. From my point of view, researching a new Fuel Electrode is the easiest way to conduct SOCs toward a rapid global expansion as new way to transform energy. These devices need new formulation for the Fuel Electrode to become a strong technology and be coupled to renewable energy sources (solar or wind). Following this disrupting strategy, it will be possible to create a completely new system capable of conversion, storage and transportation of energy: from a centralized concept, subject to monopole, to a novel capillary system where SOC technology that can configurates as a system for power generation (Fuel Cell Mode) or storage (Electrolyzer Mode). Using this marvelous idea [34], it is possible to deliver and produce energy all over the world without be completely dependent from an external source. All over the world, it means also in the rural or poor area where, nowadays, neither few kWs of electric power are available to light up hospital or heat a house in a safe way. It also needs to be underlined that in the Electrolyzer Mode exceeding energy can be converted in high added value chemical for industry: this can contribute to the whole sustainability of products production.

1.3 Three Way Catalyst

1.3.1 What is a catalyst?

Catalysts are the anonymous heroes of the chemical reactions that allow us to dare. From a general point of view, catalyst is a material that speeds up a particular chemical reaction. With the vital help from the catalyst world, molecules that might take years to react can do that in seconds. Factories must be thankful to catalysts because their using them to make everything: from polymer [35] to drugs [36]. Catalysts help process petroleum and coal into liquid fuels [37]. They are the critical key players in new technologies for a cleaner environment. A chemical reaction is when molecules break chemical bonds between their atoms. Consequently, atoms could make new bonds with other fresh new friends. This is like switching partners during a dance. Sometimes, those partnerships are easy to break. But when the relationship is stable, the molecules are delighted as they are. Catalysts make happen the process of breaking and rebuilding more efficiently by decreasing the activation energy for the chemical reaction. The catalyst is able to changes the path to the new chemical product. It is like the equivalent of choosing a highway instead of a bumpy dirt road.

1.3.2 TWC technology

The purpose of a Three Way Catalyst (TWC) is the conversion of pollutants from the internal combustion engine exhaust. The development of new formulations is an important step for automotive industry and development of new TWC technology has been critical in the past few years due to the newer stringent regulations [38]. Indeed, the development of more efficient catalysts depends on a complete understanding of the various parameters related to three-way catalyst design and formulation [39]. Normally, gasoline engine exhaust

composition can vary based on the engine and driving conditions, but typical values of the exhaust gases are 0.5 vol% CO, 3500 ppm HCs, 900 ppm NO_x, 0.17 vol% H2, 10 vol% H2O, 10 vol% CO2, 0.5 vol% O2, and the balance N_2 [40].

Satisfactory control of the previous emission can be achieved with a TWC via the simultaneous oxidation of carbon monoxide and hydrocarbons to carbon dioxide and water, and the reduction of nitrogen oxides to nitrogen gas.

$$2\,CO + O_2 \rightarrow 2\,CO_2$$

$$C_xH_y + O_2 \rightarrow CO_2 + H_2O$$

$$2\,NO \rightarrow O_2 + N_2$$

It is evident that these reactions cannot be performed simultaneously unless some conditions are decided from the beginning. To oxidize CO and the various hydrocarbons, a certain volume of oxygen is required: this condition is called lean environment (fuel/oxygen >1) [41]. However, oxygen presence inhibits the reduction of NO_x and for this reason the first generation of emission control devices were done with separate processes chambers: first performing the reduction in rich conditions (fuel/oxygen <1) [41] and only after this step, air injection for the oxidations of CO and HCs is performed. Studies on the air/fuel ratio in real engines manage to understand much better the reaction, thus discover a narrow range of compositions where there is simultaneous conversion of the main three pollutants, as illustrated in Figure 7.

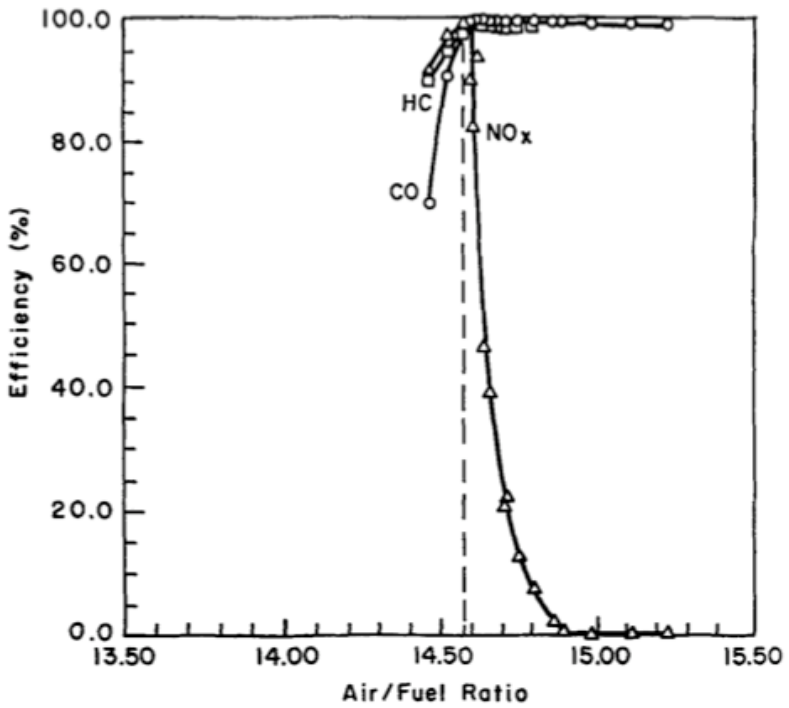

6

Figure 7 Yield efficiency for main pollutants (CO, HC, NOx) at different Air/Fuel ratios [42]

To maintain stoichiometric conditions ($\lambda = 1$) a probe is inserted before the catalytic muffler and constantly analyzes the oxygen concentration. A feedback loop circuit is mounted to control and adjusts the injection of fuel inside the engine to make sure that the air/fuel ratio stays as constant as possible. Other pollutants, such sulfur oxides and lead, are much more difficult to manage and particularly dangerous, mostly because poison irreversibly all catalysts. Thus, their control is obtained by another route: removing them directly from the fuel. Tetraethyl lead was used as an explosion-suppressor and has been banished by regulations and replaced with other compounds.

1.3.3 Platinum Group Metal: here we go again

Platinum Group Metals (PGMs) were found to be good candidates for the role of heroes of catalysis: platinum and palladium are able to be steady and durable either under reductive or

oxidizing conditions [43]. Pt and Pd (in their oxidated form) are more effective in oxidation reactions, whereas Rh is one of the best catalysts for reduction of NOx. Why this exceptional behavior?

It is possible to answer with the help of the Sabatier principle. The thought is: the best catalysts should bind atoms or molecules with an intermediate strength. The interaction should not be too weak in order to activate the reactants, and not too strong to be able to allow the products desorption. This leads to a volcano-type correlation between activity and bond strength (Figure 8).

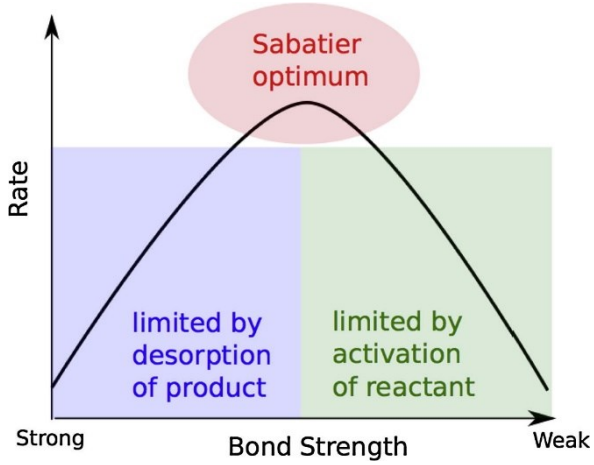

Figure 8 Schematic representation of the Sabatier principle [44]

The position of the maximum in terms of adsorption energies (or bond strength) depends slightly on the structure. This fact is related to the influence of the structure on the relationship between adsorption energy and activation energy. It can be seen that the metals, which corresponding to a particular adsorption energy shift, is controlled by the coordination number of the metal atom thus their electronic configuration. As example, in Figure 9 is possible to notice the far more reactivity toward CO oxidation by PGMs transition metals respect other elements.

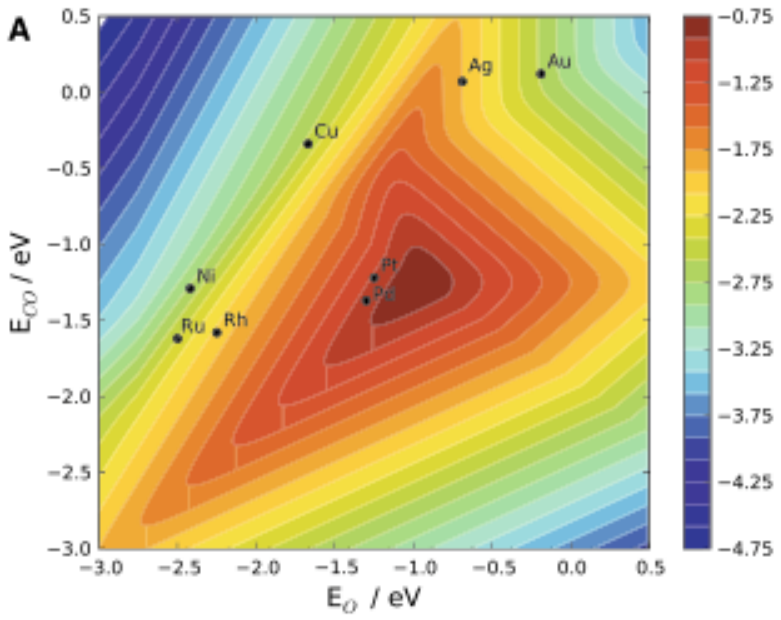

Figure 9 Transition metals representation of the 2D volcano-plot for CO oxidation [45]

1.3.4 TWC materials: state of the art and beyond

Copper and nickel-based catalysts were used as first catalytic converter in exhaust abatement. Unfortunately, the stability was weak under the conditions encountered in combustion engines. A well-done catalyst for TWC applications should be active at low temperatures (~150°-200°C) and stable up to 600°C, unfailing a wide range of oxidizing or reducing atmospheres.

As saw in paragraph 1.3.3, the well-known PGMs are widely use as active catalytic part of the system. To optimize the catalytic performance, it is convenient to divide the catalytic coating into two layers: rhodium on the part more exposed to the reductant species (CO and HCs) which allow Improving the conversion of nitrogen oxides; platinum and palladium should be confined in the regions of the catalytic system less exposed to the gas; here , after diffusion, CO and HCs can be oxidized. To help keeping the desired stoichiometric amount of oxygen,

a cerium oxide coating is added to the catalyst layer. The intrinsic characteristic of this compound is to have a high oxygen storage capacity (OSC) [46], so it retains oxygen in lean environments to release it when the exhaust mixture becomes fuel rich. TWC systems are commonly wash coated over monolithic honeycomb structures. For its exceptionally low thermal expansion coefficient and natural abundancy, common material chosen for monoliths is cordierite [47].

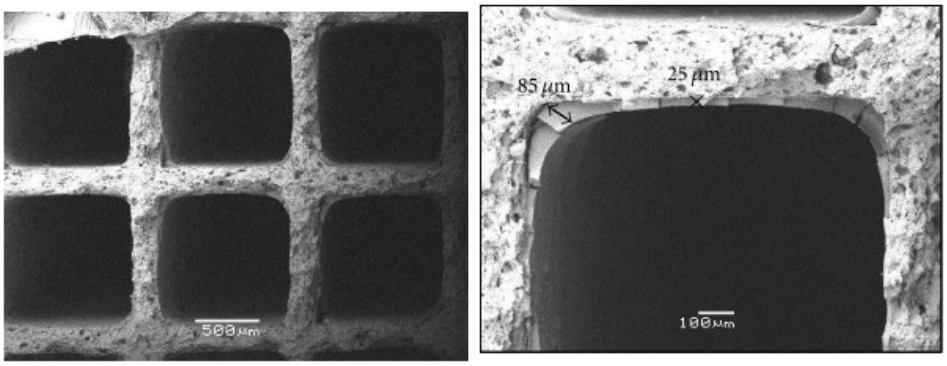

Figure 10 Example of wash coating layer on honeycomb structure [47].

Sad to say, all PGMs are listed in the European Union document called Critical Raw Materials [48]. First introduced in 2008, this document gathers all those raw materials with a high risk of supply, as they represent the first steps of the manufacturing value chain. As European Union needs to rely almost entirely on import to supply these materials, instabilities in the international political and/or economical scenario could stall the entire production. For this reason, as far as automotive pollution control is concerned, it is in the best interest of EU to replace PGMs with appropriate non-critical materials that can exhibit comparable catalytic properties. Amongst the materials studied for a possible application as TWCs there is a class of oxidic materials known as perovskites.

1.3.5 Perovskite: old but gold

Perovskites is a particular crystallographic arrangement of general formula ABX_3. In general, X in an anion and the perovskites studied in this thesis are oxides. Basically, a perovskite could be described as a cubic arranging octahedrals of formula BO_6 in a BCC (Body Cubic Centered) A-cation lattice.

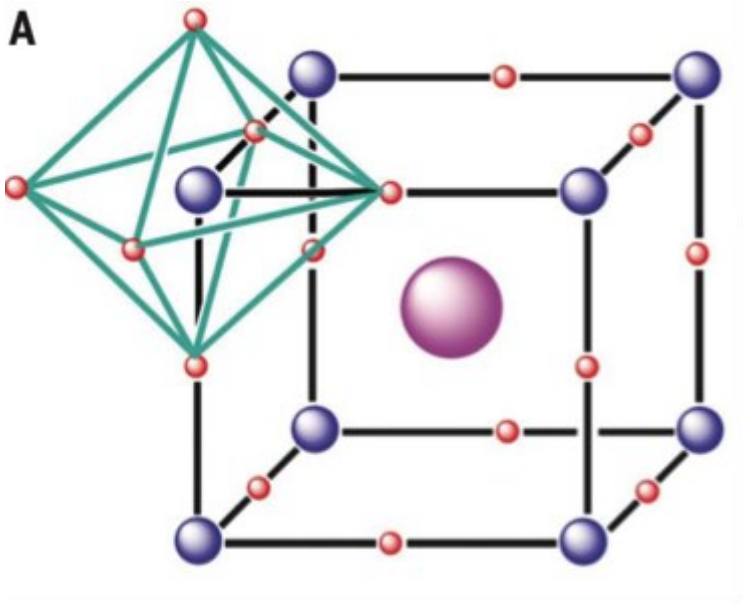

Figure 11 Cubic perovskite structure

.

Goldschmidt theorized the t-factor rule relating the stability of the cubic-perovskite phase to the empirical ionic radii of the ions inside the crystal structure.

$$t = \frac{r_A + r_O}{\sqrt{2}\,(r_B + r_O)}$$

Perovskite arrangement can be possible for t values oscillating from 0.75 to 1.05. Nonetheless, the perfect ideal cubic structure range is narrower: from 0.97 to 1.05. For lower

t values a distorted structure can be obtained: orthorhombic, rhombohedral, monoclinic, triclinic or tetragonal. Recent calculations prove that cubic structures may be formed even at higher t values [49]. With the continuous improvement of computing power, models allow to calculate the possible existence and stability for no less than 23000 different perovskite [50]. With this high number of possibilities, it is optimistic to think that one can precisely tweak the composition to generate the properties needed. To succeed strategic "doping" of a starting compound, has to be designed and optimized.

To dope a perovskite means to alter its charge neutrality and to provoke some rearrangements in the lattice. As an example, the substitution in A-site of La (III) with Sr (II) creates an excess of negative charge in the material, so the perovskite has two ways to re-equilibrate itself:

- if the element in the B-site has a certain flexibility in terms of oxidation state, it can go to a higher one. Some transition metals (e.g Mn – Fe – Cr – etc.) may do the magic, as they can be present in +2, +3 and +4 oxidation state. In addition, the ions metal creates redox couples that can boost the catalytic activity.
- by creating oxygen vacancies in the perovskite lattice. Oxygen vacancies are crucial for the catalytic activity, as they allow oxide anions to move across the material or, toward the surface, where they act as reactive sites for the molecules adsorption and activation. NOx dissociative chemisorption on surface oxygen vacancies, as an example, is the Rate Determining Step for DeNOx reactions in perovskites. A superficial vacancy can be filled by an oxide anion migrating from the bulk, or with chemisorption of oxygen, with the addition of two electrons from the material conduction band. This creates activated oxygen species on the surface, that enhance catalytic activity, especially towards oxidation reactions (e.g. CO conversion to CO_2)

As possible explanation of perovskites' activity in oxidation catalysis, the Mars von Krevelen mechanism has to be considered [51]: the catalyst directly oxidizes the reactant, and then oxygen vacancies are filled by molecular oxygen from the environment (Figure 12). Considering this mechanism, the relevance of oxygen vacancies both in surface and in the bulk and their mobility does not need to be underlined anymore.

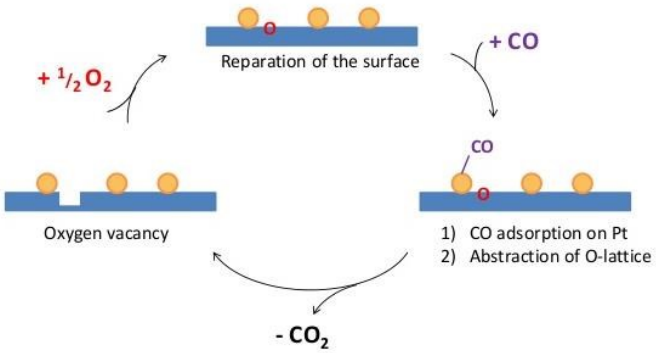

Figure 12 Mars von Krevelen mechanism illustrated for a oxide based system. The CO molecule is coordinated to the catalyst active sites (Pd nanoparticles in this case) and oxygen molecules are chemisorbed and activated by the surface vacancy. The same consideration hold for all oxides capable of allowing the formation of oxygen vacancies and their migration toward the surface. This scheme can be equally applied to perovskites that easily host oxygen vacancies.

1.3.6 Top-down nano-decoration

Until this point, we have discussed only the oxidation function of a material for TWC application. Several studies explored the possibility of NO_x reduction by metal particles supported on perovskites [52].

The Wet Impregnation procedure is the simplest way to obtain a composite catalyst where the metal catalyst is deposited on a substrate [53]. Traditionally impregnation was

introduced in catalysis to take advance of the mechanical and thermal properties of a support; the deposition of active catalyst support, moreover, allows to save precious material and to reduce the cost of the catalytic system. [H.H. Kung; Transition metal oxides: Surface Chemistry and Catalysis; Elsevier 1989 Chap. 8] The methodology is straightforward and do not need any specific fancy equipment:

- metal precursor solution,
- suspension of the substrate inside the solution,
- aging overnight to allow a better intimacy for the metal ions and the support,
- the solution is dried and the metal oxide particles are formed,
- the material may be calcined at properly temperatures and atmospheres to obtain the desired metal phase.

In recent advanced catalysis, however, impregnation has been notably improved and also the catalytic properties of the support are exploited. So nanocomposites systems In which both the oxide and metal nanoparticles are exposed to the reactants and which synergically operate to promote reactions, are developed. However, this easy procedure does not allow a precise control of the particle's dimensions and distribution. Other declinations that derive from the Wet Impregnation synthesis, required a template molecule; this modified procedures add some complexity but allow to accurately control the particles dispersion. The idea is to use a molecule as a spacer between ions thus, the final particles, may be more dispersed on the substrate surface and have smaller dimension. Some example of molecules may be ammonium [54] or citric acid [55].

The materials synthetized for TWC application during this thesis, were made, however, with a simple Wet Impregnation. The reason is to have the highest accuracy for comparison with literature and the commercial material, used as benchmark. Moreover, with the aim of Industrial application, I finally decided for the easier procedure to evaluate the better performance obtainable with this traditional procedure, knowing that they can be improved by Templated Deposition Procedure.

1.4 Water Gas Shift Reaction

The water-gas shift (WGS) is a reversible, exothermic chemical reaction. It is the combination of steam with carbon monoxide to produce carbon dioxide and hydrogen:

$$CO + H_2O \rightleftharpoons CO_2 + H_2$$

The water-gas shift reaction is a fundamental stage in many industrial processes, from ammonia to hydrogen production. As a case in point, in ammonia production the CO levels must be low, otherwise the deactivation of the synthesis catalyst may occur. Hence, the WGSR is employed as a phase in the synthesis to reduce the CO levels and produce additional hydrogen.

1.4.1 Thermodynamics of WGSR

The water-gas shift is a chemical reaction controlled mostly by equilibrium [56]. The equilibrium constant K_p as a function of temperature is shown in Figure 13

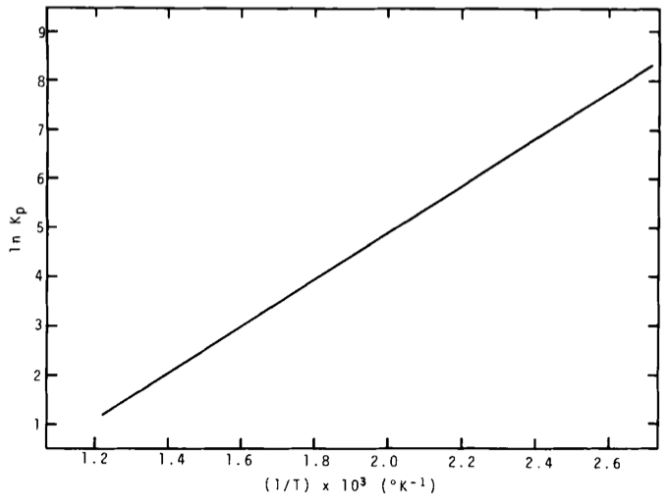

Figure 13 Equilibrium constant as function of temperature [56].

The K_p can be estimate by the following empirical formula:

$$K_p = e^{\frac{4577.8}{T} - 4.331}$$

In a simpler way, Figure 13 and the last equation state that K_p decrease with the temperature. *Ergo*, if the aim is hydrogen production, it is desirable to conduct the reaction at low temperatures. Alternatively, if the goal is to reduce the CO_2 with H_2, reaction called Reverse Water Gas Shift, low temperature must be avoided. From a practical point of view, is is Interesting that pressure does not have any effect on the equilibrium of the shift reaction.

1.4.2 Carboxyl mechanism vs Redox mechanism

In the associative mechanism carbon monoxide and water are adsorbed onto the surface of the catalyst. Eventually, the formation of an intermediate and the desorption of hydrogen and carbon dioxide occurs. In a manner of fact, H_2O dissociates on the surface of the catalyst

to yield adsorbed OH* and H*. The dissociated water reacts with CO to form a carboxyl or formiate intermediate. The intermediate, subsequently dehydrogenates to yield CO_2 and adsorbed H*. In the end, two adsorbed H* atoms recombine to form H_2.

redox mechanism	carboxyl mechanism
$CO + * \rightarrow CO*$	$CO + * \rightarrow CO*$
$H_2O + * \rightarrow H_2O*$	$H_2O + * \rightarrow H_2O*$
$H_2O* + * \rightarrow H* + OH*$	$H_2O* + * \rightarrow H* + OH*$
$OH* + * \rightarrow O* + H*$	$CO* + OH* \rightarrow COOH* + *$
$OH* + OH* \rightarrow H_2O* + O*$	$COOH* + * \rightarrow CO_2* + H*$
$CO* + O* \rightarrow CO_2* + *$	$COOH* + OH* \rightarrow CO_2* + H_2O*$
$CO_2* \rightarrow CO_2 + *$	$CO_2* \rightarrow CO_2 + *$
$H* + H* \rightarrow H_2 + 2*$	$H* + H* \rightarrow H_2 + 2*$

[a] Steps in italics highlight differences between the two mechanisms. * Indicates a vacant site. X* denotes an adsorbed X species.

Figure 14 Redox mechanism VS Carboxyl mechanism [57]

The redox mechanism, instead, involves a change in the oxidation state of the surface of material where the reaction is taking place. In this mechanism, CO is oxidized by an oxygen atom directly from the catalyst. A water molecule undergoes dissociative adsorption at the newly formed oxygen vacancy to form two OH*. The hydroxyls disproportionate to form H_2. The last step is the restoring of the starting oxidation state of the surface of the catalyst.

1.4.3 WGSR materials: reinventing the past

The water gas shift reaction can be catalyzed by both metals and metal oxide.

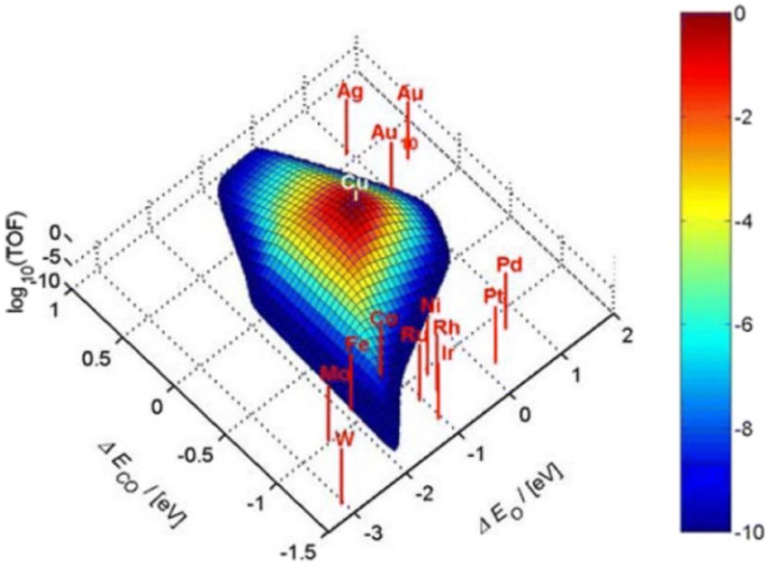

Figure 15 3D volcano plot for WGSR vs O and CO adsorption energies [58].

Figure 15 shows a 3D volcano plot for WGSR rate over the surfaces of transition metals as a function of the binding energies of atomic oxygen and carbon monoxide. The figure reveals Cu to be the most active among the more common catalysts, by being at the center with optimum adsorption energies for O and CO interactions [58].

The most used materials for WGSR are metal supported metals, as Cu/Al_2O_3 or PGM over a substrate. Less common, at least from an industrial point of view, is a class of material call spinels.

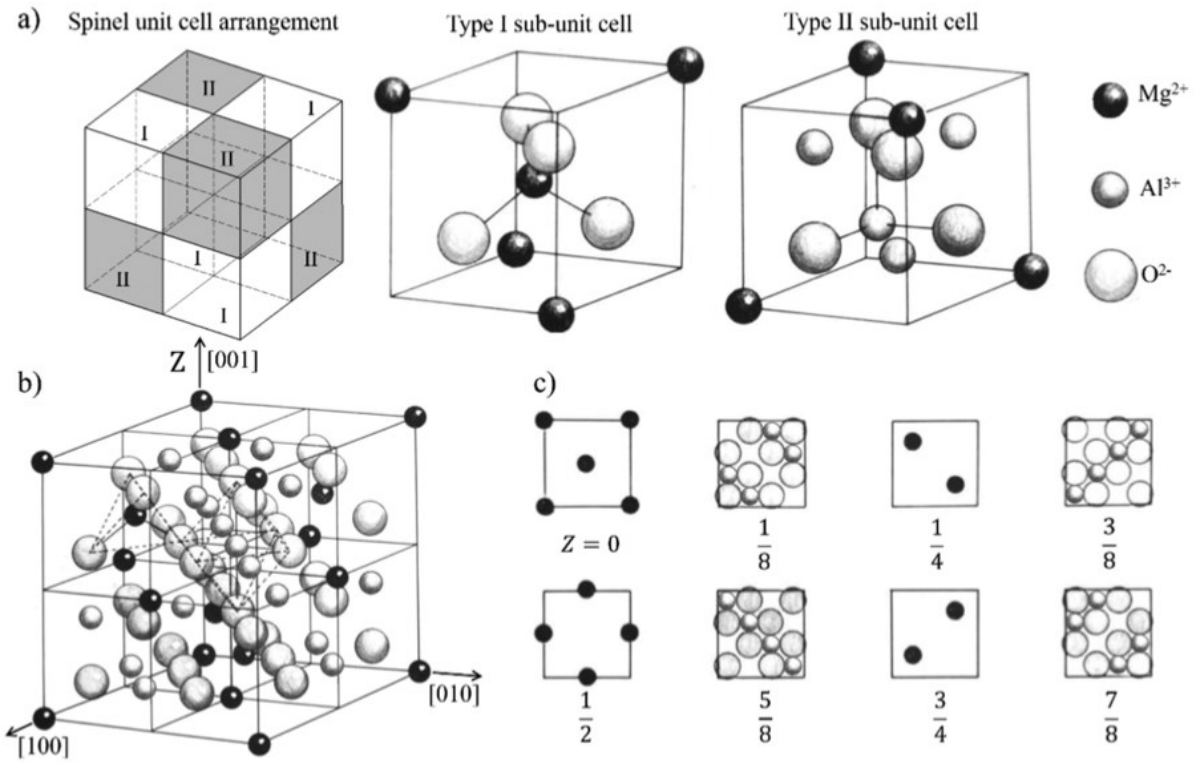

Figure 16 Crystal structure of spinel unit cell: a) two types of sub-unit cell and their arrangement in a spinel unit cell; b) a complete spinel unit cell; c) atoms arrangement in different layers of a spinel unit cell.

The spinel-type crystallographic structure characterizes many compounds having the formula AB_2O_4. Normally, A and B are a bivalent and a trivalent cation. The cations occupy 1/4 of the tetrahedral interstices and 1/2 of the octahedral interstices in the cubic close packed array of oxide ions [59]. Two possible ways or arranging are possible:

- normal spinels have bivalent ions in tetrahedral sites and trivalent ions in octahedral sites,
- inverse spinels have bivalent ions in octahedral sites and trivalent ions in both tetrahedral and octahedral sites.

In any case, most frequently spinel structures are only partially normal or inverse, with significant disorder in cation distribution. Defective spinel-type structures with both octahedrally and tetrahedrally-coordinated cations are taken by some metastable polymorphs of the sesquioxides M_2O_3 (M = Al, Fe, Cr, Ga) [60]. The thermodynamically stable forms have the corundum-type structure where only octahedral coordination for cations occurs. $A_xB_2O_{3+X}$ ($0 < x < 1$) nonstoichiometric spinels are also known and can be considered as solid solutions of the defective spinels-type M_2O_3 oxides and the stoichiometric spinels AB_2O_4.

1.4.4 Bottom-up nano-decoration

The exsolution is a process well known in geology [61] but in the catalytic world just in 2002 Nishihata *et al.* [62] reported the possible exsolution of Pd from $LaFe_{0.57}Co_{0.38}Pd_{0.05}O_3$. However, it was with the work of Neagu, Irvine *et al.* [63] that exsolution started to obtain its deserved stage. Exsolution is a phenomenon where metal catalysts are segregated from an oxide lattice to an oxide surface under specific condition, as it is possible to see in Figure 17. Unlike the conventional deposition techniques, exsolution is particularly attractive for its time efficiency due to the possibility to avoid another synthesis step.

The most used way to extract the metal particle from the matrix is the gas/temperature route. In particular, more the matrix is stable and more the condition of temperature and gas must be severe.

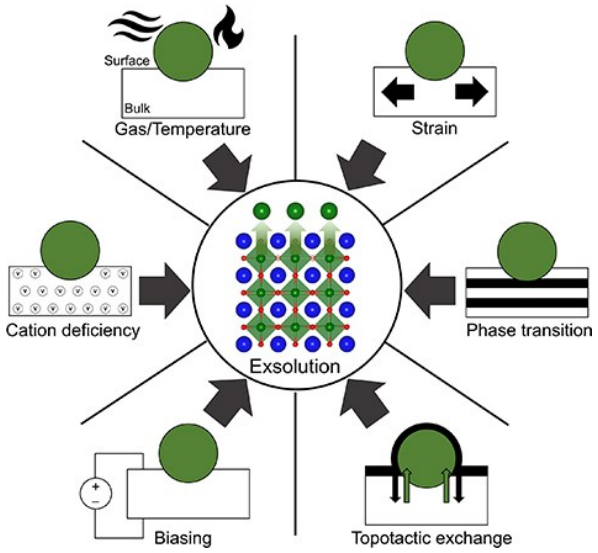

Figure 17 Possible ways to achieve the exsolution process [64].

After the exsolution process, the particles are not free to move on the surface like it can happen with the deposited metals deposited by different procedures (sub-chapter 1.3.6). Rather, they remain partially embedded in the matrix. The interaction at the interface is thus maximized, inducing completely different lattice strain effects that may modify the catalytic activity.

1.5 Outline and aim of this thesis

To summarize, let me resume the technologies and strategies presented in the previous pages that were chosen as possible solutions to the energy demand and air pollution in the world.

First, Solid Oxide Cells (SOCs) where illustrated with the aim to show how this technique is extremely efficient to transform chemical energy into electrical energy (Fuel Cell mode) and *vice versa* (Electrolyzer mode). From thermodynamics fundamental (1.2.1) to the state of the

art of the materials (1.2.2): a short walk to eventually, try to answer the question of why this incredible technology deserves to be investigated (1.2.3).

From energy transformation to air pollution dilemma, the Introduction chapter continue with Three Way Catalysts (TWCs). This technology is fundamental to avoid harmful emission from vehicle that use internal combustion engine. Nowadays is the rising age of electric car but the problems behind the use of batteries are significant and the Fuel Cell technology it is not a ready on market technology. Moreover, the technology behind TWCs can be an extremely useful starting point to developed new materials which can be used in different applications (abatement of exhausts in stable plants, development of catalyst for highly demanding application). During the engine function, as mentioned in the sub-chapter 1.3.2, the λ probe is responsible to adjust the fuel/oxygen ration in the gas mixture. In other word, the catalyst is constantly subjected to changing atmosphere, thus to a continuous change of a sort of equilibrium [65]. The know-how developed in the last 50 years can be extremely helpful to enrich the database of new materials that can benefit from an oscillating dis-equilibrium to perform in a better way and of synergic mechanisms in complex reactions.

To conclude, two main aspects unify the research presented in this thesis: the care for environment and the idea of developing innovative materials by slight and careful modification of spinel and perovskite system. Care of environment: to demonstrate that progress is sustainable, that energy can be converted minimizing the generation of pollutants.

Spinel and perovskite crystallographic structure are a tremendously simple way elaborate by nature to arrange some metal ions (sub-chapter 1.4.3 and 1.3.5). It is possible to bestow to spinel and perovskite the specific behavior that a specific application needed, adjusting with

craftiness the composition. More important, it is possible to elaborate a starting material that can completely change his catalytic behavior, transforming itself in a new *in situ* catalyst.

In detail, the outline of the thesis:

1. In Chapter 2 will be present the methodology used to characterize and tested all the materials synthesized: spinels based on Cu and Fe, perovskites based on La and Fe.
2. Chapter 3 and Chapter 4 will be dedicated to the 6 months passed at the Paul Sherrer Insitut (PSI) under the supervision on Dr. Davide Ferri. The materials were characterized more exhaustively with *in situ* XRD, X-ray Absorption Spectroscopy (XAS) using the Swiss Light Synchrotron (SLS). Eventually, the materials were tested for Water Gas Shift Reaction and Three Way Catalyst reaction.
3. In Chapter 5 will be presented the spinels that outstand from the WGSR process and tested as Fuel Electrode for SOC application. From the preparation of the button cells to the electrochemical process involved.
4. In Chapter 6 the showcase, still under construction, of the possibility that have some perovskite to change their crystallographic structure under specific condition. The data were recorded at the European Synchrotron Radiation Facilities (ESRF) at the beamline ID15.

1.6 Bibliography

[1] D. Bogdanov *et al.*, "Low-cost renewable electricity as the key driver of the global energy transition towards sustainability," *Energy*, vol. 227, p. 120467, 2021.

[2] M. Ram, M. Child, A. Aghahosseini, D. Bogdanov, A. Lohrmann, and C. Breyer, "A comparative analysis of electricity generation costs from renewable, fossil fuel and nuclear sources in G20 countries for the period 2015-2030," *J. Clean. Prod.*, vol. 199, pp. 687–704, 2018.

[3] O. Koskinen and C. Breyer, "Energy Storage in Global and Transcontinental Energy Scenarios: A Critical Review," *Energy Procedia*, vol. 99, no. March, pp. 53–63, 2016.

[4] P. A. Narbel, "Rethinking how to support intermittent renewables," *Energy*, vol. 77, pp. 414–421, 2014.

[5] A. Mikhaylov, N. Moiseev, K. Aleshin, and T. Burkhardt, "Global climate change and greenhouse effect," *Entrep. Sustain. Issues*, vol. 7, no. 4, pp. 2897–2913, 2020.

[6] S. Arrhenius, "On theInfluence of Carbonic Acid in the Air upon the Temperature of the Ground," *Philos. Mag. J. Sci.*, vol. 41, no. 251, pp. 237–279, 1896.

[7] N. Ekholm, "On the Variations of the Climate of the Geological and Historical Past and Their Causes," *Q. J. R. Meteorol. Soc.*, vol. 27, no. 117, pp. 1–62, 1901.

[8] P. K. Addo, B. Molero-Sanchez, M. Chen, S. Paulson, and V. Birss, "CO/CO2 study of high performance Lao.3Sro.7Feo.7Cro.3O3-δ reversible SOFC electrodes," *Fuel Cells*, vol. 15, no. 5, pp. 689–696, 2015.

[9] D. M. Bastidas, S. Tao, and J. T. S. Irvine, "A symmetrical solid oxide fuel cell demonstrating redox stable perovskite electrodes," *J. Mater. Chem.*, vol. 16, no. 17, pp.

1603–1605, 2006.

[10] C. León, M. Lucía, and J. Santamaría, "Correlated ion hopping in single-crystal yttria-stabilized zirconia," *Phys. Rev. B - Condens. Matter Mater. Phys.*, vol. 55, no. 2, pp. 882–887, 1997.

[11] L. Lei, J. Zhang, Z. Yuan, J. Liu, M. Ni, and F. Chen, "Progress Report on Proton Conducting Solid Oxide Electrolysis Cells," *Adv. Funct. Mater.*, vol. 29, no. 37, 2019.

[12] I. T. Bello, "Scientometric review of proton-conducting solid oxide fuel cells," *International Journal of Hydrogen Energy*, vol. 46. pp. 37406–37428, 2021.

[13] L. Carrette, K. A. Friedrich, and U. Stimming, "Fuel Cells: Principles, Types, Fuels, and Applications," *ChemPhysChem*, vol. 1, no. 4, pp. 162–193, 2000.

[14] J. J. Lee, E. W. Park, and S. H. Hyun, "Performance and evaluation of Cu-based nano-composite anodes for direct utilisation of hydrocarbon fuels in SOFCs," *Fuel Cells*, vol. 10, no. 1, pp. 145–155, 2010.

[15] C. Jin, C. Yang, F. Zhao, A. Coffin, and F. Chen, "Direct-methane solid oxide fuel cells with Cu1.3Mn 1.7O4 spinel internal reforming layer," *Electrochem. commun.*, vol. 12, no. 10, pp. 1450–1452, 2010.

[16] N. Hedayat, Y. Du, and H. Ilkhani, "Review on fabrication techniques for porous electrodes of solid oxide fuel cells by sacrificial template methods," *Renew. Sustain. Energy Rev.*, vol. 77, no. 1, pp. 1221–1239, 2017.

[17] A. Afif, N. Radenahmad, Q. Cheok, S. Shams, J. H. Kim, and A. K. Azad, "Ammonia-fed fuel cells: A comprehensive review," *Renew. Sustain. Energy Rev.*, vol. 60, pp. 822–835, 2016.

[18] M. F. Han, H. Y. Yin, W. T. Miao, and S. Zhou, "Fabrication and properties of anode-supported solid oxide fuel cell," *Solid State Ionics*, vol. 179, no. 27–32, pp. 1545–1548,

2008.

[19] S. B. Adler, "Factors governing oxygen reduction in solid oxide fuel cell cathodes," *Chem. Rev.*, vol. 104, no. 10, pp. 4791–4843, 2004.

[20] H. Fan, M. Keane, N. Li, D. Tang, P. Singh, and M. Han, "Electrochemical stability of Lao.6Sro.4Co 0.2Feo.8O3-δ-infiltrated YSZ oxygen electrode for reversible solid oxide fuel cells," *Int. J. Hydrogen Energy*, vol. 39, no. 26, pp. 14071–14078, 2014.

[21] S. Wang, H. Tsuruta, M. Asanuma, and T. Ishihara, "Ni-Fe-La(Sr)Fe(Mn)O3 as a new active cermet cathode for intermediate-temperature CO2 electrolysis using a LaGaO3-based electrolyte," *Adv. Energy Mater.*, vol. 5, no. 2, pp. 1–10, 2015.

[22] A. Kulkarni *et al.*, "Mixed ionic electronic conducting perovskite anode for direct carbon fuel cells," *Int. J. Hydrogen Energy*, vol. 37, no. 24, pp. 19092–19102, 2012.

[23] H. Huang, C. H. Hsieh, N. Kim, J. Stebbins, and F. Prinz, "Structure, local environment, and ionic conduction in scandia stabilized zirconia," *Solid State Ionics*, vol. 179, no. 27–32, pp. 1442–1445, 2008.

[24] A. J. Jasper, J. A. Kilner, and D. W. Mccomb, "Probing Interfaces in Gd-doped Ceria Electrolytes," vol. 161, no. 2003, p. 53502, 2007.

[25] T. Ishihara, N. M. Sammes, and O. Yamamoto, "Electrolytes," *High-temperature Solid Oxide Fuel Cells Fundam. Des. Appl.*, pp. 83–117, 2003.

[26] M. B. Mogensen *et al.*, "Ni migration in solid oxide cell electrodes: Review and revised hypothesis," *Fuel Cells*, vol. 21, no. 5, pp. 415–429, 2021.

[27] W. Yue *et al.*, "Enhancing coking resistance of Ni/YSZ electrodes: In situ characterization, mechanism research, and surface engineering," *Nano Energy*, vol. 62, no. December 2018, pp. 64–78, 2019.

[28] F. C. Nix and D. MacNair, "The thermal expansion of pure metals: Copper, gold,

aluminum, nickel, and iron," *Phys. Rev.*, vol. 60, no. 8, pp. 597–605, 1941.

[29] H. Hayashi, T. Saitou, N. Maruyama, H. Inaba, K. Kawamura, and M. Mori, "Thermal expansion coefficient of yttria stabilized zirconia for various yttria contents," *Solid State Ionics*, vol. 176, no. 5–6, pp. 613–619, 2005.

[30] A. Faes, A. Hessler-Wyser, A. Zryd, and J. Van Herle, "A review of RedOx cycling of solid oxide fuel cells anode," *Membranes (Basel).*, vol. 2, no. 3, pp. 585–664, 2012.

[31] M. Backhaus-Ricoult, "Interface chemistry in LSM-YSZ composite SOFC cathodes," *Solid State Ionics*, vol. 177, no. 19-25 SPEC. ISS., pp. 2195–2200, 2006.

[32] M. Shah, P. W. Voorhees, and S. A. Barnett, "Time-dependent performance changes in LSCF-infiltrated SOFC cathodes: The role of nano-particle coarsening," *Solid State Ionics*, vol. 187, no. 1, pp. 64–67, 2011.

[33] D. Tian *et al.*, "Enhanced performance of symmetrical solid oxide fuel cells using a doped ceria buffer layer," *Electrochim. Acta*, vol. 208, pp. 318–324, 2016.

[34] K. Al-Khori, Y. Bicer, and M. Koç, "Comparative techno-economic assessment of integrated PV-SOFC and PV-Battery hybrid system for natural gas processing plants," *Energy*, vol. 222, p. 119923, 2021.

[35] M. Seth and T. Ziegler, "Polymerization properties of a heterogeneous Ziegler-Natta catalyst modified by a base: A theoretical study," *Macromolecules*, vol. 36, no. 17, pp. 6613–6623, 2003.

[36] N. Adsorbent, R. During, I. Potable, and W. Reuse, "Nano-Based Adsorbent And Photo Catalyst : Pharmaceutical Contaminants Removal During Indirect Potable Water Reuse," vol. 2, no. 1, pp. 5–11, 2021.

[37] E. Iglesia, "Design, synthesis, and use of cobalt-based Fischer-Tropsch synthesis catalysts," *Appl. Catal. A Gen.*, vol. 161, no. 1–2, pp. 59–78, 1997.

[38] R. García-Contreras *et al.*, "Impact of regulated pollutant emissions of Euro 6d-Temp light-duty diesel vehicles under real driving conditions," *J. Clean. Prod.*, vol. 286, 2021.

[39] M. Giuliano *et al.*, "Characterization of the evolution of noble metal particles in a commercial three-way catalyst: Correlation between real and simulated ageing," *Catalysts*, vol. 11, no. 2, pp. 1–15, 2021.

[40] S. Rood, S. Eslava, A. Manigrasso, and C. Bannister, "Recent advances in gasoline three-way catalyst formulation: A review," *Proc. Inst. Mech. Eng. Part D J. Automob. Eng.*, vol. 234, no. 4, pp. 936–949, 2020.

[41] M. Wang, P. Dimopoulos Eggenschwiler, D. Ferri, and O. Kröcher, "Experimental and modeling-based analysis of reaction pathways on catalysts for natural gas engines under periodic lean/rich oscillations," *Chem. Eng. J.*, vol. 430, 2022.

[42] P. Taylor, M. Shelef, and G. W. Graham, "Why Rhodium in Automotive Three-Way Catalysts?," *Catal. Rev. Sci. Eng.*, vol. 36, pp. 433–457, 1994.

[43] S. K. Matam *et al.*, "Thermal and chemical aging of model three-way catalyst Pd/Al 2O 3 and its impact on the conversion of CNG vehicle exhaust," *Catal. Today*, vol. 184, no. 1, pp. 237–244, 2012.

[44] A. J. Medford *et al.*, "From the Sabatier principle to a predictive theory of transition-metal heterogeneous catalysis," *J. Catal.*, vol. 328, pp. 36–42, 2015.

[45] L. C. Grabow, B. Hvolbæk, and J. K. Nørskov, "Understanding trends in catalytic activity: The effect of adsorbate-adsorbate interactions for Co oxidation over transition metals," *Top. Catal.*, vol. 53, no. 5–6, pp. 298–310, 2010.

[46] M. Sugiura, "Oxygen storage materials for automotive catalysts: Ceria-zirconia solid solutions," *Catal. Surv. from Asia*, vol. 7, no. 1, pp. 77–87, 2003.

[47] M. Adamowska and P. Da Costa, " Structured Pd/ γ -Al 2 O 3 Prepared by

Washcoated Deposition on a Ceramic Honeycomb for Compressed Natural Gas Applications ," *J. Nanoparticles*, vol. 2015, pp. 1–9, 2015.

[48] M. Girtan, A. Wittenberg, M. L. Grilli, D. P. S. De Oliveira, C. Giosu, and M. L. Ruello, "The Critical Raw Materials Issue between Scarcity, Supply Risk, and Unique Properties," *Materials (Basel).*, vol. 14, pp. 1–18, 2021.

[49] S. C. Tidrow, "Mapping comparison of goldschmidt's tolerance factor with perovskite structural conditions," *Ferroelectrics*, vol. 470, no. 1, pp. 13–27, 2014.

[50] C. J. Bartel *et al.*, "New tolerance factor to predict the stability of perovskite oxides and halides," *Sci. Adv.*, vol. 5, no. 2, pp. 1–10, 2019.

[51] P. Schlexer, D. Widmann, R. J. Behm, and G. Pacchioni, "CO Oxidation on a Au/TiO2 Nanoparticle Catalyst via the Au-Assisted Mars-van Krevelen Mechanism," *ACS Catal.*, vol. 8, no. 7, pp. 6513–6525, 2018.

[52] Q. Yang, G. Liu, and Y. Liu, "Perovskite-Type Oxides as the Catalyst Precursors for Preparing Supported Metallic Nanocatalysts: A Review," *Ind. Eng. Chem. Res.*, vol. 57, no. 1, pp. 1–17, 2018.

[53] A. Gurbani, J. L. Ayastuy, M. P. González-Marcos, J. E. Herrero, J. M. Guil, and M. A. Gutiérrez-Ortiz, "Comparative study of CuO-CeO2 catalysts prepared by wet impregnation and deposition-precipitation," *Int. J. Hydrogen Energy*, vol. 34, no. 1, pp. 547–553, 2009.

[54] G. Carollo *et al.*, "CuO/Lao.5Sro.5CoO3 nanocomposites in TWC," *Appl. Catal. B Environ.*, vol. 255, no. January, 2019.

[55] G. Carollo, A. Garbujo, A. Bedon, D. Ferri, M. M. Natile, and A. Glisenti, "Cu/CGO cermet based electrodes for Symmetric and Reversible Solid Oxide Fuel Cells," *Int. J. Hydrogen Energy*, vol. 45, no. 25, pp. 13652–13658, 2020.

[56] P. Taylor and D. S. Newsome, "The Water-Gas Shift Reaction Conditions," *Catal. Rev. Sci. Eng.*, vol. 21, no. 2, pp. 275–318, 1980.

[57] A. A. Gokhale, J. A. Dumesic, and M. Mavrikakis, "On the mechanism of low-temperature water gas shift reaction on copper," *J. Am. Chem. Soc.*, vol. 130, no. 4, pp. 1402–1414, 2008.

[58] P. Ebrahimi, A. Kumar, and M. Khraisheh, "A review of recent advances in water-gas shift catalysis for hydrogen production," *Emergent Mater.*, vol. 3, no. 6, pp. 881–917, 2020.

[59] G. Busca, V. Lorenzelli, G. Ramis, and R. J. Willey, "Surface Sites on Spinel-Type and Corundum-Type Metal Oxide Powders," *Langmuir*, vol. 9, no. 6, pp. 1492–1499, 1993.

[60] B. Lavina, G. Salviulo, and D. Della Giusta, "Cation distribution and structure modelling of spinel solid solutions," *Phys. Chem. Miner.*, vol. 29, no. 1, pp. 10–18, 2002.

[61] R. A. Yund and R. H. McCallister, "Kinetics and mechanisms of exsolution," *Chem. Geol.*, vol. 6, no. C, pp. 5–30, 1970.

[62] Y. Nishihata *et al.*, "Self-regeneration of a Pd-perovskite catalyst for automotive emissions control," *Nature*, vol. 418, no. 6894, pp. 164–167, 2002.

[63] J. H. Myung, D. Neagu, D. N. Miller, and J. T. S. Irvine, "Switching on electrocatalytic activity in solid oxide cells," *Nature*, vol. 537, no. 7621, pp. 528–531, 2016.

[64] O. Kwon, S. Joo, S. Choi, S. Sengodan, and G. Kim, "Review on exsolution and its driving forces in perovskites," *JPhys Energy*, vol. 2, no. 3, 2020.

[65] D. Ferri, M. Elsener, and O. Kröcher, "Methane oxidation over a honeycomb Pd-only three-way catalyst under static and periodic operation," *Appl. Catal. B Environ.*, vol. 220, pp. 67–77, 2018.

Chapter 2

"You cannot create experience. You must undergo it."

Albert Camus

2.1 Powder preparation

If not otherwise stated spinel-type and perovskite-type metal oxides were synthesized using the amorphous citrate-based process. The citric acid is used as a complexing agent for metal cations in aqueous solution [1] [2] [3]. The thorough, homogeneous mixing of precursors in solution allows for the formation of phase pure crystal at lower calcination temperatures compared to solid state methods. In this way, the resulting materials have a comparably higher specific surface area (10 - 40 m^2g^{-1}) [4].With respect to other sol-gel procedures (such as Pechini method, as an example) the citric acid route requires less reactants and has been considered more adequate to the Industrial up-scale.

Depending on requested composition, suitable amounts of metal oxides were dissolved in nitric acid (or metal nitrates were dissolved in deionized water) and mixed to form a homogeneous solution. The second step is to dissolve the correct amount of citric acid. The overall molar ratio of metal cations to citric acid was kept constant at 1:1.9. The resultant solution was stirred at room temperature for 60 min before drying overnight at 70°C. The brownish precursor, after increasing the plate temperature to 270 ºC, ignites itself burning all the organic components. The resulted precursor was then crushed to a fine powder and subjected to temperature programmed calcination.

Copper impregnated perovskite were prepared from Cu-free supports synthesized according to the procedure above. Appropriate amounts of $Cu(NO_3)_2$ were dissolved in deionized water before being mixed to the perovskitic support. The drying process was again conducted under constant stirring overnight at 50°C followed by calcination in air [5].

2.2 Specific surface area determination

Nitrogen physisorption at -196°C was used to determine the specific surface area (SSA) based on the theory of Brunauer-Emmett-Teller [6] (BET) using a ASAP 2020 instrument from Micromeritics. The measurements were conducted on 0.5 g of powder sample, which was outgassed at 300°C for 6 h. Seven-point adsorption isotherms were collected in the pressure range of 0.05 - 0.3 P/P_0, as typically values applied for mesoporous materials.

2.3 X-ray diffraction

2.3.2 *Ex situ* measurements

The crystal structure of powder samples was investigated by *ex situ* powder X-ray diffraction (XRD) using a diffractometer (Bruker D8 Advance) equipped with Ni filtered Cu Kα radiation, variable slits and energy sensitive line detector (LynxEye). Diffractograms were collected at an acquisition time of 3 s and a step size of $\Delta 2\theta$ = 0.02 º in the range 20-70 º. Background fitting, peak parameter determination and phase identification were performed using the EVA software from Bruker.

The Scherrer equation [7] was used to estimate the perovskite and spinel crystallite size (d):

$$d = \frac{K\,\lambda}{FWHM\,\cos\vartheta}$$

This equation includes the form factor (K = 0.9), the X-ray wavelength of the source (λ = 1.54 Å in case of Cu anode), the angular reflection position (θ) and the full width at half maximum of the corresponding reflection feature (FWHM).

2.3.2 *In situ* measurements

In situ XRD measurements were conducted on the same instrument using an *in situ* XRD reactor chamber (XRK 900, Anton Paar). Reactive gases (5 vol% H_2/N_2 and 20 vol% O_2/N_2) were dosed to the chamber during the experiment (100 sccm) using mass flow controllers (MFC, Bronkhorst). Sample temperature was monitored using a K-type thermocouple.

2.4 X-ray absorption spectroscopy

X-ray absorption spectroscopy (XAS) measurements were performed at the SuperXAS beamline of the Swiss light source (SLS, Villigen, Switzerland) using a 2.9 T superbend magnet as the source. The beam current and the energy of the storage ring were 400 mA and 2.4 GeV, respectively. Subsequently the beam was collimated using a Si coated collimating mirror at 2.9 mrad and then monochromatised using a liquid nitrogen cooled Si 111 channel cut monochromator oscillating at a 1 Hz repetition rate [8]. The resulting beam was then focused to a 1 mm x 0.4 mm spot size on sample using a Rh coated torroidal double focussing mirror. Transmission geometry measurements were carried out with 1.5 bar N_2 filled ion chambers and energy calibration by consideration of the maximum of the first derivative of a simultaneously measured Fe or Cu foil. The data were processed using ProQEXAFS [9] for calibration, normalisation and averaging over the 3 minutes data acquisition per sample. Spectra were collected in fluorescence mode using a N_2 filled ion chamber to monitor incoming beam intensity and a five element SD silicon drift detector mounted at 90° to the beam and the sample mounted at 45°. The beam was collimated using a Si coated mirror, which was also used for the reduction of higher harmonic contributions, while the required X-ray energies were scanned around the Cu or Fe K- edge using a Si (111) channel-cut

monochromator. The beam was focused to a spot size of 2 mm × 0.2 mm (H×V). *Ex situ* measurements were conducted on pelletized samples at room temperature.

2.5 High energy X-ray diffraction

Operando time-resolved X-ray diffraction patterns were acquired at beamline ID15A of the ESRF (Grenoble, France, beam size 100 x 100 μm) using a Pilatus X detector (1679 x 1475 pixels, Dectris) at a time resolution of 0.5 s and at an incident energy of 79.5 keV. The samples (sieve fraction, 100–150 μm) were firmly mounted between two quartz wool plugs in a quartz capillary reactor (OD = 2 mm, wall thickness 50 μm) which allowed the insertion of a 0.5 mm thermocouple. The sample was positioned 800 mm from the detector. The reactor was connected to a gas manifold allowing for fast switching of the feed to simulate reductive and oxidative operation and was interfaced by heated stainless steel capillary to a mass spectrometer (MS, Pfeiffer Omnistar GSD 320) for on-line gas analysis. The following m/z values were recorded: 2 (H_2), 4 (He), 18 (water), 28 (CO), 32 (O_2) and 44 (CO_2). Feed conditions were controlled by two solenoid on/off valves placed in front of the quartz reactor and slaved to the beamline control software to synchronize data acquisition and gas switches. Heating was provided using a hot air blower.

An experiment consisted in heating the sample to the desired temperature (300, 400 and 500 °C) in 5 vol% O_2/He followed by repeated and alternate pulses of 5 vol% CO/He, 1 vol% Ar and 5 vol% O_2/He (30 s each).

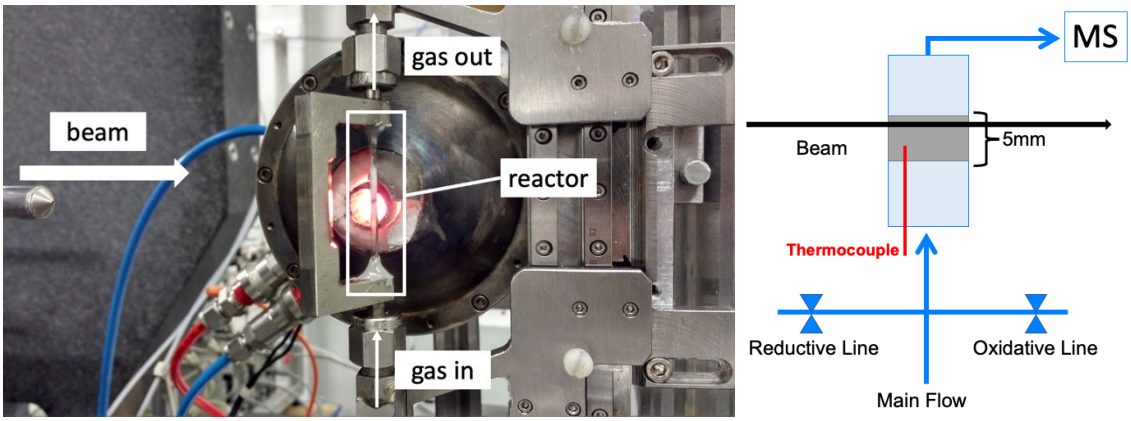

Figure 18 Left: image of the setup used at the beamline ID15A.

Right: scheme of the system used during operando measurements.

Above 300°C, the measurements at selected temperatures were interspersed by heating to 600°C in 5 vol% O_2/He in order to ensure restauration of the original structure, which was confirmed by XRD.

2.6 Temperature programmed reduction

Temperature programmed reduction (TPR) experiments were carried out on a bench top AutoChem 2920 instrument equipped with a thermal conductivity detector to measure H_2 consumption. The samples (~50 mg) were loaded into the quartz reactor tube. Measurements were recorded in 5 vol% H_2/Ar (30 sccm) and with a heating rate of 10 °Cmin^{-1}. TPR samples were previously outgassed with He (50 sccm) at room temperature. Single TPRs were usually conducted up to 800°C.

2.7 Scanning microscopy

Scanning electron microscopy (SEM) was used to observe morphological changes of powder samples and the structural evolution of Cu particles over the course of reducing process. The instrument used to obtain all SEM images was a field emission SEM (Zeiss ULTRA 55). Powder samples were deposited on sticky carbon pads on aluminum stubs before analysis. The samples were analyzed using a 20 keV electron beam and the in-lens secondary electron detector at a working distance of 7 mm. Magnifications in the range of 50,000 - 100,000 allowed the analysis of Cu particles.

2.8 Catalytic tests

2.8.1 Reverse water gas shift reaction

Catalytic activity tests towards the reverse water gas shift reaction (RWGS) were conducted at atmospheric pressure using the setup showed in Figure 19. Reactants and products were analyzed using an FTIR spectrometer (ThermoFisher Antaris) equipped with a heated 2-m gas cell. In each experiment, the sieved sample (50 - 100 mg) was mixed with 50 - 100 mg of cordierite and loaded in a tubular quartz reactor (d_i=6 mm). Prior to the reaction, all the samples were heated with 10% O_2 in N_2 (100 sccm) to 400 °C at 10 °C/min. MFCs (BROOKS) were used to dose the reactant gases and a K-type thermocouple placed in the middle of the catalyst bed was used to monitor temperature.

The tests were conducted two times with all the samples, replacing every time the catalyst used with a fresh one:

a. with pre-reduction (5% H_2 in N_2) up to 300 ºC.

b. no pre-treatment.

The reactant gas mixture (5 % H_2 / 1 % CO_2 / rest N_2) was fed at a total flow rate of 100 sccm with a ramp of 10 ºC from room temperature up to 600 ºC.

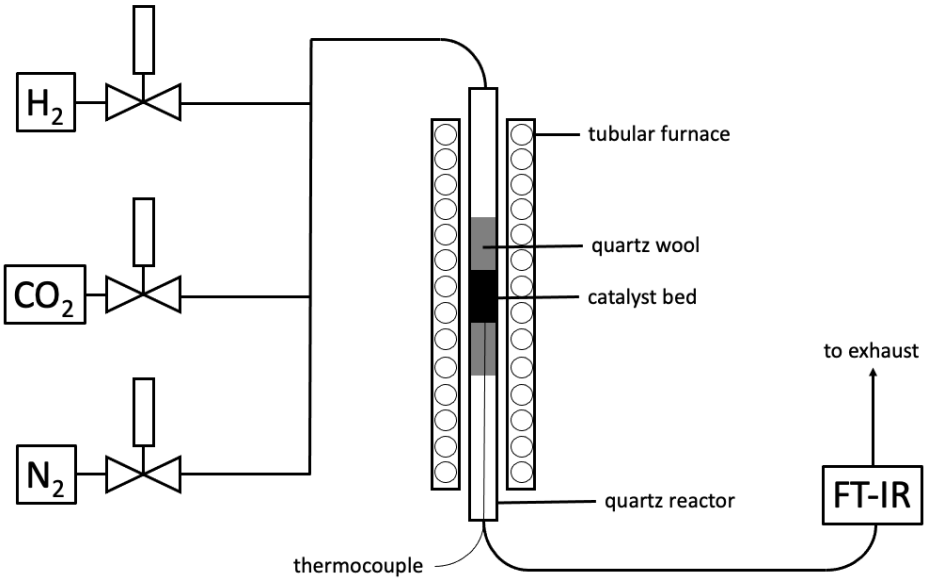

Figure 19 Catalytic test setup: MFCs mixing unit, heated stainless steel tubing, tubular furnace (Tmax = 700°C) and a spectrophotometer FT-IR for gas composition analysis.

2.8.2 Three-way catalyst reaction

The activity of the powder catalysts toward TWC reaction was evaluated with a system considerably comparable with the one showed in the previous paragraph (Figure 19). The gas flow after reaction was analyzed with a InProcess Instruments GAM 400 mass spectrometer and with a FT-IR Brucker Alpha II equipped with a 7 cm gas cell with a ZnSe window. The gas cell is heated to 150 ºC during measurement.

Spectra were recorded from 3000 to 300 cm^{-1} at a resolution of 4 cm^{-1} and scanner velocity of 0.33 Hz. The sample and background spectra resulted from averaging 30 and 20 scans,

respectively. Fragments with m/z ratios of 2 (H_2), 4 (He), 18 (H_2O), 28 (N_2/CO), 30 (NO), 32 (O_2), and 44 (CO_2, N_2O) were followed. The exothermic effect of the reaction was minimized by diluting the catalyst (50 mg, 150–200 μm sieve fraction) with cordierite 150 mg, 100–150 μm). Feed conditions were controlled by two solenoid on/off valves (Series 9, Parker; opening time <5 ms) placed in front of the reactor. The conditions followed the idea proposed in a previous publication [10]. Under rich conditions the feed composition was 0.7 vol% CO, 0.15 vol% NO, 0.16 vol% C_3H_8 balanced with He. When 0.7 vol% O_2 was added, the feed composition was only slightly lean. Experiments under constant feed were performed with 0.7 vol% CO, 0.15 vol% NO, 0.16 vol% C_3H_8, 1 vol% O_2, balanced with He. Rich or lean feed conditions were maintained for 20 s each. The long pulse time and the predominantly rich reaction conditions relative to realistic operation are suitable from an experimental viewpoint to study the catalytic and reducing response. The large difference in oxygen concentration, much larger than expected for operation in real, was selected to enhance the chemical response. Samples temperatures were monitored continuously using a K-type thermocouple inserted parallelly in the inlet of the catalyst bed and controlled by a house made software. Before performing catalytic experiments, the samples were treated in 5 vol% O_2/He (50 sccm) at 400 ºC for 30 min.

2.9 Electro-catalytic tests

2.9.1 Cells manufacturing

In the current thesis the button cell design was chosen due to its simplicity. Between the possible configurations, electrolyte-supported was realized to increment the reproducibility of the test. The main purpose of this work is, in fact, studying the property of the synthesized

catalyst as fuel electrode in a solid oxide cell. To obtain the green pellet 2.5g of $La_{0.8}Sr_{0.20}Ga_{0.8}Mg_{0.2}O_3$ (LSGM) or yttria stabilized zirconia (8-YSZ) [11] powder was compressed utilizing a pressure of 4.5 tons for 5 minutes; eventually the pellet was treated thermically at 1500°C for 6 hours with a ramp of 5°C/min until 1100° followed by a ramp of 3°C/min up to the final temperature. The manufactured electrolytes possessed dimensions of 20 mm diameter and 1 mm thickness. To prepare the ink, catalyst powder and 3% wt carbon soot was mixed in a mortar, followed by the addition of two α-terpineol based polymers. The ink was deposited via tape casting utilizing a 12 mm diameter mask. This method allowed to obtain electrode thicknesses of 30 μm [12]. Once the electrodes were deposited, a further heat treatment was carried out to optimize the adhesion: 1100°C for 2h in air with a 3°C/min ramp. A gold paste made of a commercial compound of gold and an organic binder has then been deposited by tape casting on the electrodes as current collector.

2.9.2 Electrochemical Impedance spectroscopy (EIS)

The best way to study a material as electrode in a solid oxide cell is the symmetrical configuration [13] [14]: both the electrodes are equal and are composed by the same materials. For symmetrical test, the cell was supported by an α-alumina DEGUSSIT AL23 tube able to canalize the gases parallel to the electrodes' surface, as showed in Figure 20. Platinum wires present on the ceramic tube were connected to the golden wires on the cell in order to establish a consistent electron pathway.

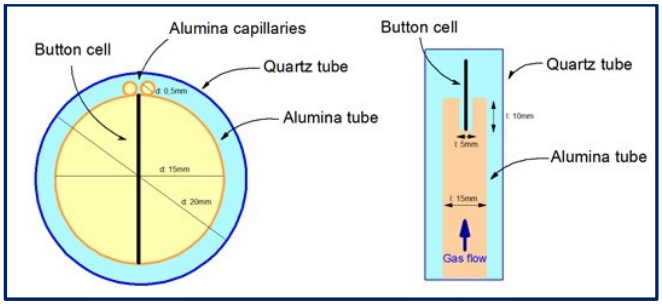

Figure 20 Representation of the symmetrical setup used for electrochemical measurements.

Electrochemical results were obtained through PGSTAT 302 Autolab Frequency Response Analyzer: The tests were carried out in steady state conditions, i.e., with no DC current in the frequency range of 10^{-2}-10^{6} Hz with a signal amplitude of 20 mV. All EIS data were fitted and analyzed through the ZView 4 software and different circuits were utilized to fit different EIS data. The number of R-CPE is the number of the processes seen in the Nyquist and Bode plots. It this thesis was decided to use the CPE (i.e., Constant Phase Element) instead of a normal capacitor since capacitors in EIS experiments often do not fit correctly the curve due to their inability to modulate a real process [15].

2.10 Bibliography

[1] K. Faungnawakij, N. Shimoda, T. Fukunaga, R. Kikuchi, and K. Eguchi, "Crystal structure and surface species of $CuFe_2O_4$ spinel catalysts in steam reforming of dimethyl ether," *Appl. Catal. B Environ.*, vol. 92, no. 3–4, pp. 341–350, 2009.

[2] J. E. Tasca, C. E. Quincoces, A. Lavat, A. M. Alvarez, and M. G. González, "Preparation and characterization of $CuFe_2O_4$ bulk catalysts," *Ceram. Int.*, vol. 37, no. 3, pp. 803–812, 2011.

[3] H. S. Lim *et al.*, "Ni-exsolved $La_{1-x}Ca_xNiO_3$ perovskites for improving CO_2 methanation," *Chem. Eng. J.*, vol. 412, no. October, 2021.

[4] D. D. Athayde *et al.*, "Review of perovskite ceramic synthesis and membrane preparation methods," *Ceram. Int.*, vol. 42, no. 6, pp. 6555–6571, 2016.

[5] A. Gurbani, J. L. Ayastuy, M. P. González-Marcos, J. E. Herrero, J. M. Guil, and M. A. Gutiérrez-Ortiz, "Comparative study of CuO-CeO_2 catalysts prepared by wet impregnation and deposition-precipitation," *Int. J. Hydrogen Energy*, vol. 34, no. 1, pp. 547–553, 2009.

[6] S. Brunauer, P. H. Emmett, and E. Teller, "Adsorption of Gases in Multimolecular Layers," *J. Am.Chem.Soc.*, vol. 60, no. 2, pp. 309–319, 1938.

[7] "Bestimmung der Grösse und der inneren Struktur von Kolloidteilchen mittels Röntgenstrahlen. Nachrichten von der Gesellschaft der Wissenschaften zu Göttingen," pp. 98–100, 1918.

[8] O. Müller, M. Nachtegaal, J. Just, D. Lützenkirchen-Hecht, and R. Frahm, "Quick-EXAFS setup at the SuperXAS beamline for in situ X-ray absorption spectroscopy with 10ms time resolution," *J. Synchrotron Radiat.*, vol. 23, pp. 260–266, 2016.

[9] A. H. Clark, J. Imbao, R. Frahm, and M. Nachtegaal, "ProQEXAFS: A highly optimized parallelized rapid processing software for QEXAFS data," *J. Synchrotron Radiat.*, vol. 27, pp. 551–557, 2020.

[10] I. Alxneit, A. Garbujo, G. Carollo, D. Ferri, and A. Glisenti, "CuO/Lao.5Sro.5CoO3: Precursor of efficient NO reduction catalyst studied by: Operando high energy X-ray diffraction under three-way catalytic conditions," *Phys. Chem. Chem. Phys.*, vol. 22, no. 34, pp. 18798–18805, 2020.

[11] J. B. Goodenough, "Oxide-ion conductors by design," *Nature*, vol. 404, no. 6780, pp. 821–823, 2000.

[12] G. Carollo, A. Garbujo, A. Bedon, D. Ferri, M. M. Natile, and A. Glisenti, "Cu/CGO cermet based electrodes for Symmetric and Reversible Solid Oxide Fuel Cells," *Int. J. Hydrogen Energy*, vol. 45, no. 25, pp. 13652–13658, 2020.

[13] S. P. S. Shaikh, A. Muchtar, and M. R. Somalu, "A review on the selection of anode materials for solid-oxide fuel cells," *Renew. Sustain. Energy Rev.*, vol. 51, pp. 1–8, 2015.

[14] N. Mahato, A. Banerjee, A. Gupta, S. Omar, and K. Balani, "Progress in material selection for solid oxide fuel cell technology: A review," *Prog. Mater. Sci.*, vol. 72, pp. 141–337, 2015.

[15] Q. A. Huang, R. Hui, B. Wang, and J. Zhang, "A review of AC impedance modeling and validation in SOFC diagnosis," *Electrochim. Acta*, vol. 52, no. 28, pp. 8144–8164, 2007.

Chapter 3

"I wear a mask. And that mask, it's not to hide who I am, but to create what I am."

Batman

3.1 Introduction

Spinel oxides have been used in various catalytic applications, including the decomposition of CO_2 [1] and gaseous pollutants like the various nitric oxides [2]. In this thesis chapter, the main reaction studied is the reversible and exothermic water gas shift reaction (WGSR):

$$CO + H_2O \rightleftharpoons CO_2 + H_2$$

Investigation has been mostly driven by spinel-based systems made up by iron and copper. Spinel crystallographic structures are a tremendously simple system way elaborated by the nature to arrange some metal ions (sub-chapter 1.4.3 and 1.3.5) in a perfect architecture with overwhelming catalytic properties. It is possible to bestow to spinel the specific behavior that a specific application needed, adjusting with craftiness the composition [3]. At this purpose, different dopings with aluminum were provided to understand the correlation between structural integrity and reactivity. The fundamental idea behind this work is trying to elaborate a starting material that can completely change its catalytic behavior and transforming itself in a new *in situ* catalyst.

3.2 Experimental

3.2.1 Synthesis

Spinel-type mixed oxides of composition $CuFe_2O_4$, $CuFeAlO_4$ and $CuAl_2O_4$ were synthesized via the citrate-gel method [4] described in chapter 2.1. Final calcination was conducted at 800°C for 6 h to obtain the desired crystal phase. As reference, α-Al_2O_3 were loaded with Cu

by wet impregnation (chapter 2.1) with an aqueous solution of $Cu(NO_3)_2 \cdot 6H_2O$ to produce 10 wt% Cu/Al_2O_3. The composite material was dried overnight and calcined at 450 ºC for 2 h. Prior to experiments all the samples were ground to a fine powder in an agate mortar and eventually sieved with fraction of 100-150 μm.

3.2.2 Characterization

Phase purity of the powder catalysts was verified by powder X-ray diffraction (XRD) using the instrumentation and settings described in Chapter 2.3.2. XRD patterns were also collected *in situ* during reduction (5% H_2 in N_2) and oxidation (20% O_2 in N_2) of spinel samples ($CuFe_2O_4$, $CuFeAlO_4$, $CuAl_2O_4$) on the same instrument using a XRK 900 reactor chamber from Anton Paar. In these experiments the angular range was scanned using a step size of 0.05° in the range 20° - 70°.

Cu K-edge (8.9789 keV) and Fe K-edge (7.1120 keV) X-ray absorption spectra were acquired on pelletized samples in fluorescence mode at the X10DA (SuperXAS) beamline of the Swiss Synchrotron Light Source (SLS, Villigen, Switzerland) as described in Chapter 2.4. XAS spectra of the samples were fitted using as reference the samples listed in Table 1.

Table 1 References used for XAS measurements and calculations.

Cu	Fe
metallic Cu	metallic Fe
CuO	Fe_3O_4

Cu_2O	FeO
-	y-FeOOH

Temperature programmed reduction experiments were performed using the procedure explained in Chapter 2.6. The samples (~50 mg) were loaded into the quartz reactor tube and measurements were recorded in 5 vol% H_2/Ar (30 sccm) and with a heating rate of 10 °C min^{-1}. To evaluate a possible reversibility of the structure, for the sample $CuFe_2O_4$ a reoxidation step between two TPR was performed with 20 % O_2/N_2 up to 400 ºC with a heating rate of 10 °C min^{-1}.

The specific surface area (SSA) of the calcined powder was determined by N_2 physisorption isotherms as described in Chapter 2.2.

Changes in the microstructure of the samples as a result of reduction condition were studied using scanning electron microscopy (SEM) by the instrumentation described in Chapter 2.7. Images were collected on calcined and reduced samples (5 vol% H_2/Ar, 300°C, 1 h) as well as on fresh samples.

Catalytic activity tests towards water gas shift reaction were carried out on the homemade test setup described in Chapter 2.8.1. Catalytic tests were conducted on pre-reduced samples (5 vol% H_2/N_2, 300°C, 1 h) and fresh samples.

3.3 Results and discussion

3.3.1 X-ray diffraction

Phase purity and crystal symmetry of all powder samples were assessed using powder X-ray diffraction (XRD). The obtained patterns were compared with JCPDS (Joint Committee on Powder Diffraction Standards) database and found to correspond well with the respective entries. Figure 1 shows diffraction patterns gathered for the samples $CuFe_2O_4$ (JCPDS 006-0545), $CuFeAlO_4$ (JCPDS reference under revision) and $CuAl_2O_4$ (JCPDS 01-078-556) [6]. All samples exhibit the characteristic diffraction peaks around 30.5°, 35.6°, and 62.6° 2θ positions, which correspond to the hkl (220), (311) and (440) Miller indices of a spinel ferrite with the Fd3m space group [5].

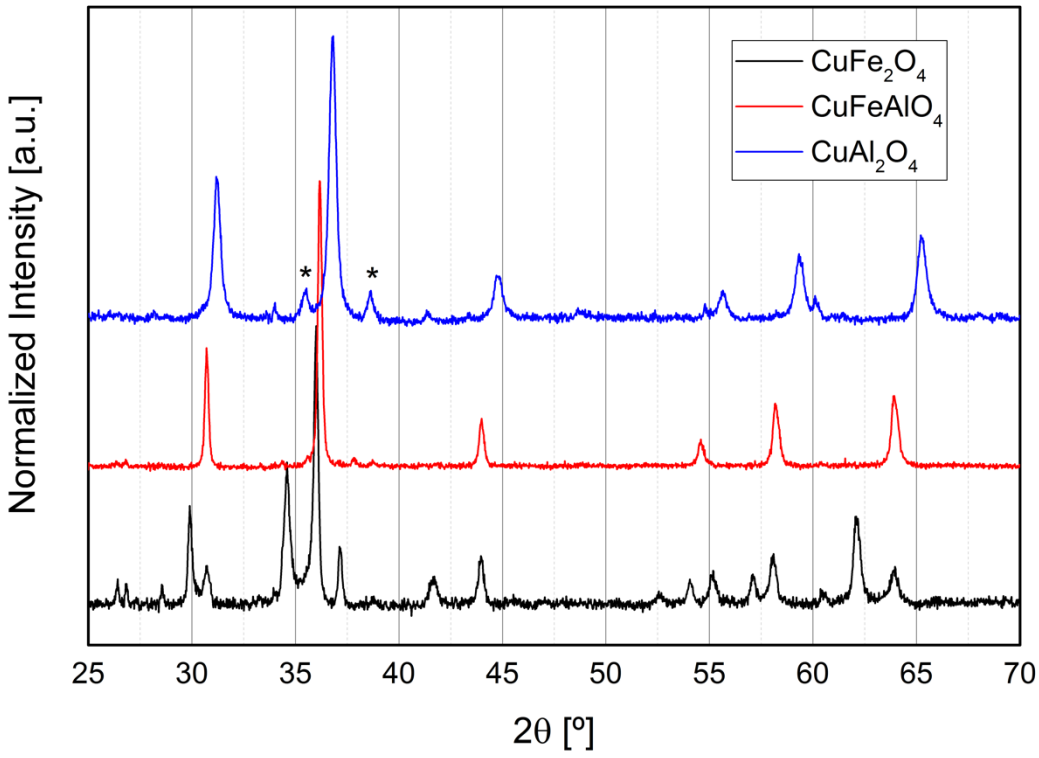

Figure 21 Normalized powder XRD patterns of $CuFe_2O_4$, $CuFeAlO_4$ and $CuAl_2O_4$. The presence of CuO impurities is marked with (*).

Is possible to see from Figure 21 that the angle of the peak at ~36º increase with the aluminum content. Iron and aluminum cations tend to preferentially occupy the octahedral A and B sites than the tetrahedral positions. Instead, Cu cations prefer the tetrahedral positions [6].

The relatively high calcination temperature (800 ºC) causes the narrow shape of the peaks. The average size of crystallite was calculated, on all powder samples, using the Scherrer equation [7] considering the full width at half maximum (FWHM) of the main reflection of the samples. In Table 2 are listed the values for the synthesized spinels.

Table 2 Average dimension of crystals calculated from Scherrer equation.

$CuFe_2O_4$	32.3 nm
$CuFeAlO_4$	30.7 nm
$CuAl_2O_4$	27.6 nm

The ratios of metal cations (Al/Fe) into the solid system influences the crystallographic structure. In the sample $CuFe_2O_4$ the cations and anions arrangement are tetragonal while the insertion of Al inside the lattice, lead to the more symmetric arrangement, cubic ($CuFeAlO_4$ – $CuAl_2O_4$). The presence of aluminum guarantees the stabilization of the cubic symmetry also at room temperature (see Chapter 3.3.2). Secondary phase was found only for $CuAl_2O_4$ and is attributed to CuO, with Bragg peaks located at 2θ=36.0° and 38.0° (marked by * in Figure 21).

3.3.2 *In situ* X-ray diffraction

In situ XRD measurements were conducted in isothermal condition at different temperature and different environments. Temperatures were chosen following the TPR profiles for each sample (Chapter 3.3.3).

$CuFe_2O_4$ – O_2

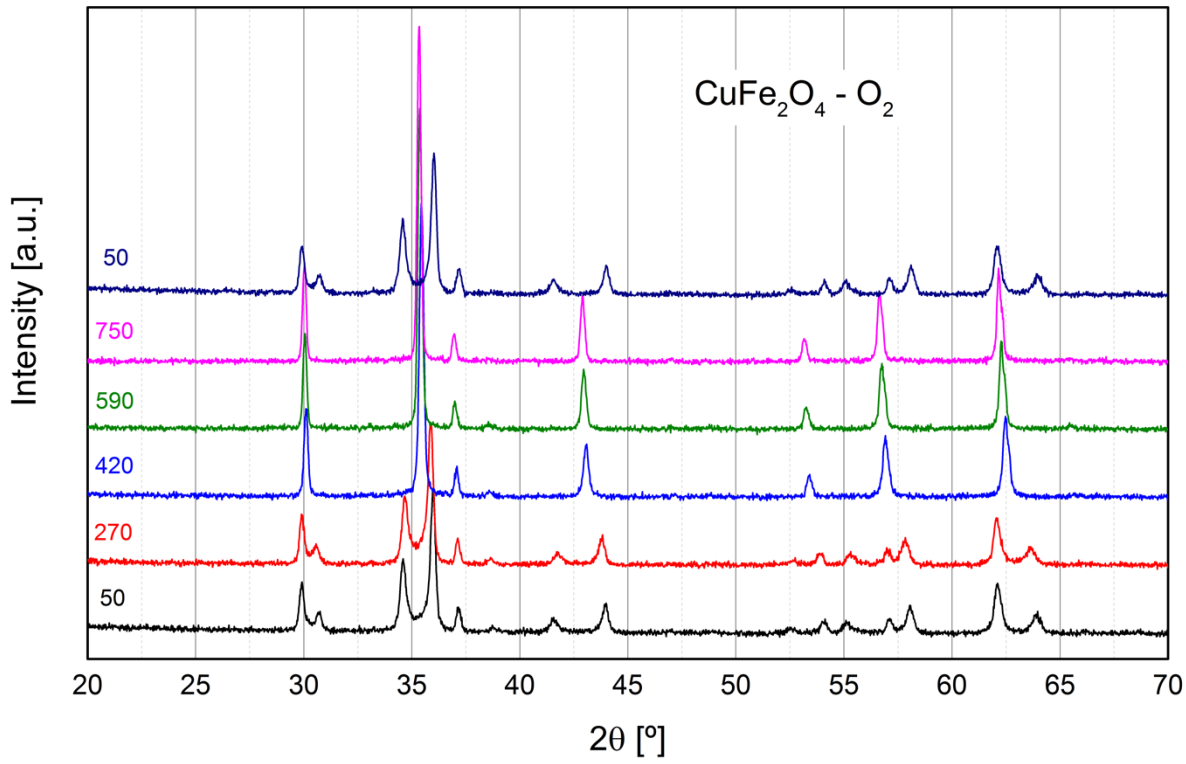

Figure 22 In situ XRD patterns of $CuFe_2O_4$ under 20% O_2/N_2. XRD taken in isothermal conditions at different temperatures: 50 - 270 - 420 - 590 - 750 ºC. First pattern (from the top) was taken at room temperature after all the treatments.

In situ XRD under oxidative condition of $CuFe_2O_4$ allowed to observe a particular behavior of this system. At room temperature, the system arranges itself In a tetragonal disposition, where the cation Cu^{2+} is comfortable in octahedral sites. Fe^{2+} and Fe^{3+}, instead, can settle in octahedral and tetrahedral sites. In general, the crystal structure of spinels can be cubic or tetragonal. As for $CuFe_2O_4$, the cubic-to-tetragonal phase transformation of $CuFe_2O_4$, is irreversible at room temperature [8], since the tetragonal distortion of $CuFe_2O_4$ is more thermodynamically stable than the cubic one. From Figure 22, under 20% O_2 in N_2, the structural changes start to appear above 420 ºC and the phase changes from tetragonal to cubic. A low number of peaks appeared from 420 ºC to 750 ºC and no other phases are formed. As mentioned before, synthesis plays a crucial role: when the starting materials

exhibit tetragonal phase, the structural changes are completely reversible and without losing crystallinity.

$CuFe_2O_4$ – H_2

If the spinel system studied is placed under reducing environment, irreversible structural changes may occur. *In situ* XRD measurements were performed using 5% H_2 in N_2, in isothermal condition using the same temperatures chosen for oxidative tests.

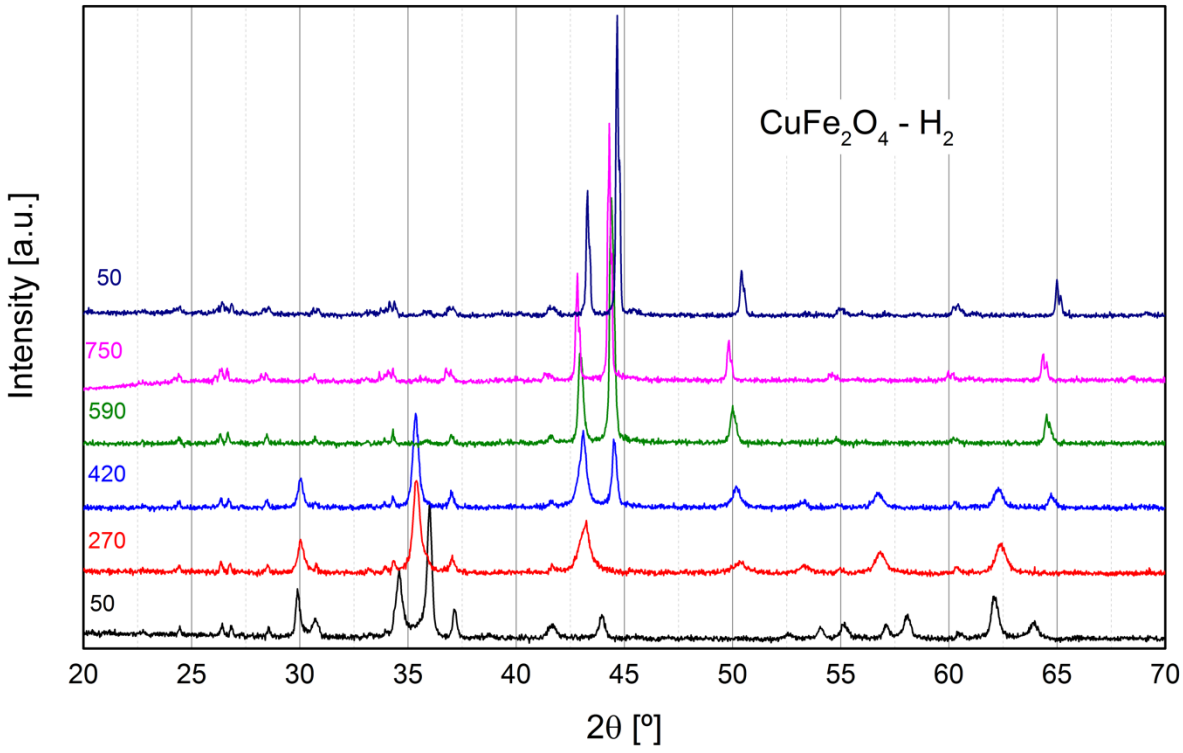

Figure 23 In situ XRD pattern of $CuFe_2O_4$ under 5% H_2/N_2. XRD taken in isothermal conditions at different temperature: 50 - 270 - 420 - 590 - 750 ºC. First pattern (from the top) was taken at room temperature after all the treatment.

Unlike the spinel in oxidative condition, under hydrogen atmosphere, structural changes appear at lower temperature, according to TPR profile (Chapter 3.3.3). At 270 ºC copper starts migrating from the lattice toward the surface to form bulk aggregates, as suggested by the presence of Cu^0 peaks at 42º and 50º 2θ. At higher temperature also iron cations start

to reduce leaving the spinel structure and forming Fe^0 (peak at 44 º 2θ). From 270 ºC to 420 ºC, the crystallographic structure of $CuFe_2O_4$ change from tetragonal to cubic due to temperature increment and cation (Cu^{2+} - Fe^{2+} - Fe^{3+}) migration [9]. Above 420 ºC the spinel starts to decompose completely to metallic copper and metallic iron without possibility of reversible transition.

$CuFeAlO_4$

In order to balance and maintain the spinel structure under reducing atmosphere, a doping in B-site could be a suitable solution. For Investigating the system $CuFeAlO_4$ *in situ* XRD was performed at different temperatures between room temperature and 750°C.

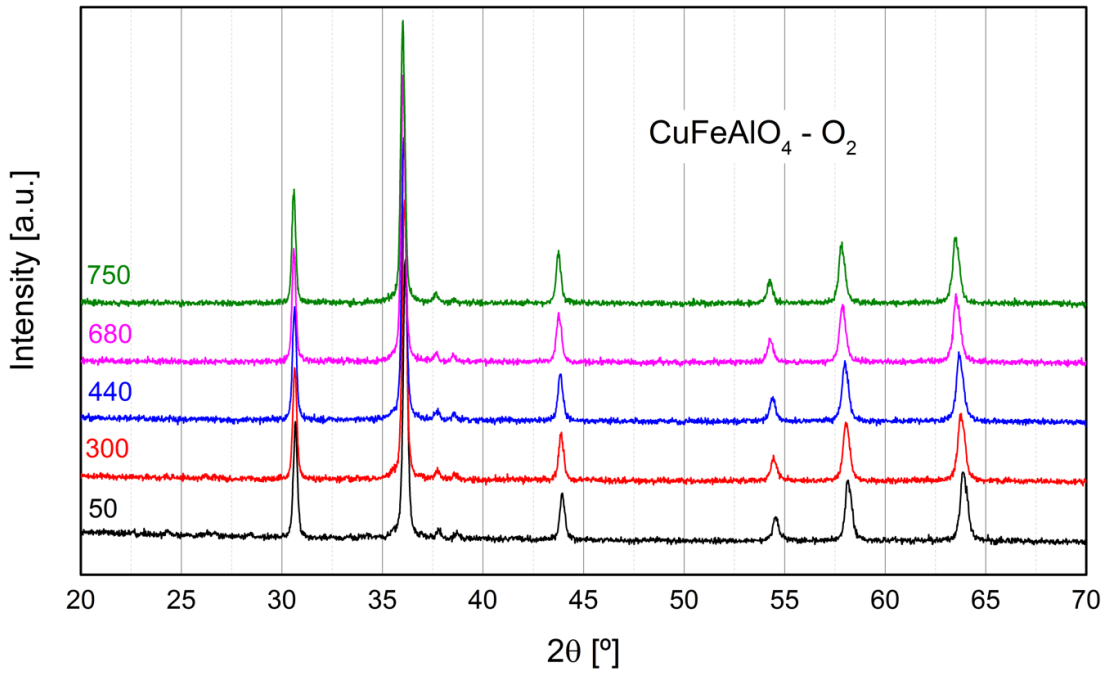

Figure 24 In situ XRD pattern of $CuFeAlO_4$ under 20% O_2/N_2. XRD taken in isothermal conditions at different temperature: 50 – 300 - 440 - 680 - 750 ºC.

The aluminum insertion in $CuFe_2O_4$ allows to stabilize the cubic phase also at room temperature and for this reason, no structural changes were noted under oxidative environment (Figure 24).

Unlike iron (for which two different oxidation numbers are possible), aluminum can be only Al^{3+} and can, therefore, occupy only octahedral sites in spinel system. The insertion of aluminum atoms revealed to be a strategic help to fulfil this goal because it contributes to create a more stable spinel structure but, at the same time, allows to reduce the remaining cations and to enhance the preparation of heterogeneous catalyst.

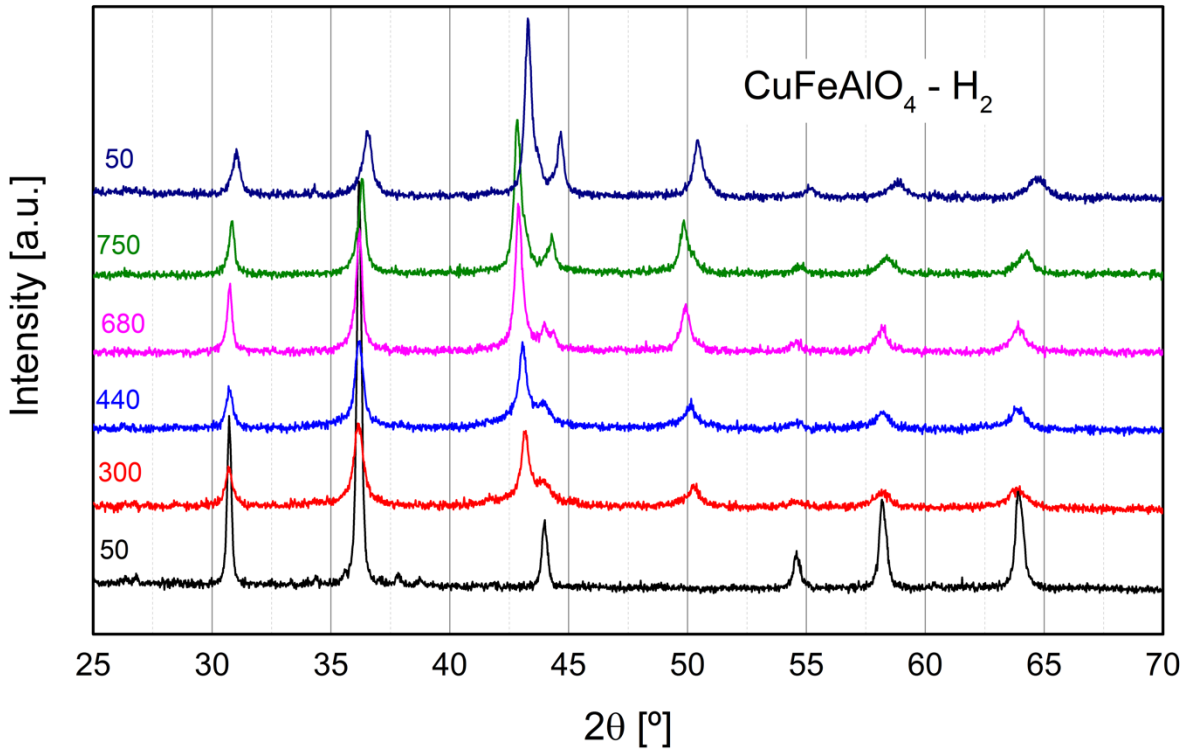

Figure 25 In situ XRD pattern of $CuFeAlO_4$ under 5% H_2/N_2. XRD taken in isothermal conditions at different temperature: 50 – 300 - 440 - 680 - 750 ºC. First pattern (from the top) was taken at room temperature after all the treatment.

The hypothesis was confirmed from *in situ* XRD under hydrogen. At 300 ºC copper cations copper start to migrate from the spinel structure to form Cu nanoparticles that decorate the

surface (Chapter 3.3.2) of the residual spinel. Raising the temperature only provides an increment of the amount of copper extracted from the structure.

As largely described previously in this thesis, that copper cannot be reinserted inside the lattice of the spinel oxide, hence the process is irreversible [10]. At the higher temperatures investigated, 750 ºC, the new system is composed as Cu nanoparticles over the new spinel $FeAl_2O_4$ [11]. From XRD measurements is not possible to evaluate with sufficient accuracy if the nanoparticles are composed only by copper or by an alloy formed by Cu and Fe. *In situ* XRD measurements allowed to confirm the presence of metallic copper over a spinel substrate, necessary condition for Reverse Water Gas Shift reaction, Three Way Catalyst and for electric conductivity in electrodes for Solid Oxide Cells.

$CuAl_2O_4$

In the previous section, aluminum demonstrates the ability to preserve the integrity of the spinel under reducing condition when the exsolution of Cu takes place. But what happens to the oxide when the structure is unable to reduce itself enough? Here, in order to answer this question, cupro-spinel without iron in B-site will be investigated. As much as in the case of $CuFeAlO_4$, the presence of aluminum stabilizes the cubic structure also at room temperature, as shown in Figure 26.

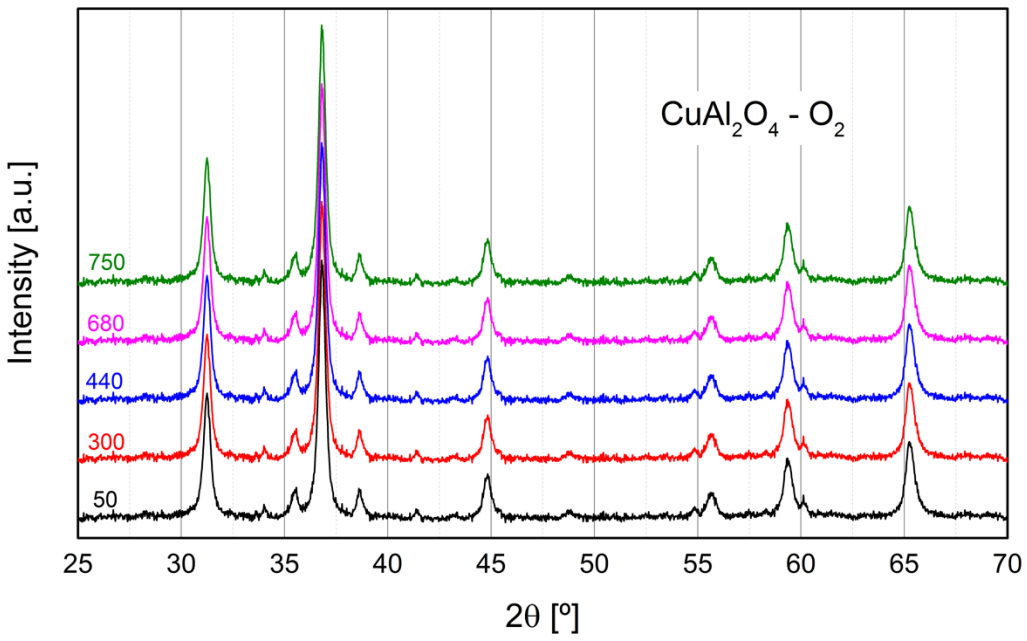

Figure 26 In situ XRD pattern of $CuAl_2O_4$ under 20% O_2/N_2. XRD taken in isothermal conditions at different temperature: 50 – 300 - 440 - 680 - 750 ºC.

Without Fe inside the structure, the only cation that can migrate from the lattice is Cu^{2+}. At 300 ºC, Figure 27, copper starts to accumulate as a new metallic phase. From 440 ºC up to 750 ºC the copper transition from Cu^{2+} to Cu^0 continues until a new phase is formed. The system, after the reduction treatment, is composed by copper particles supported by the $CuAl_2O_4$ left over.

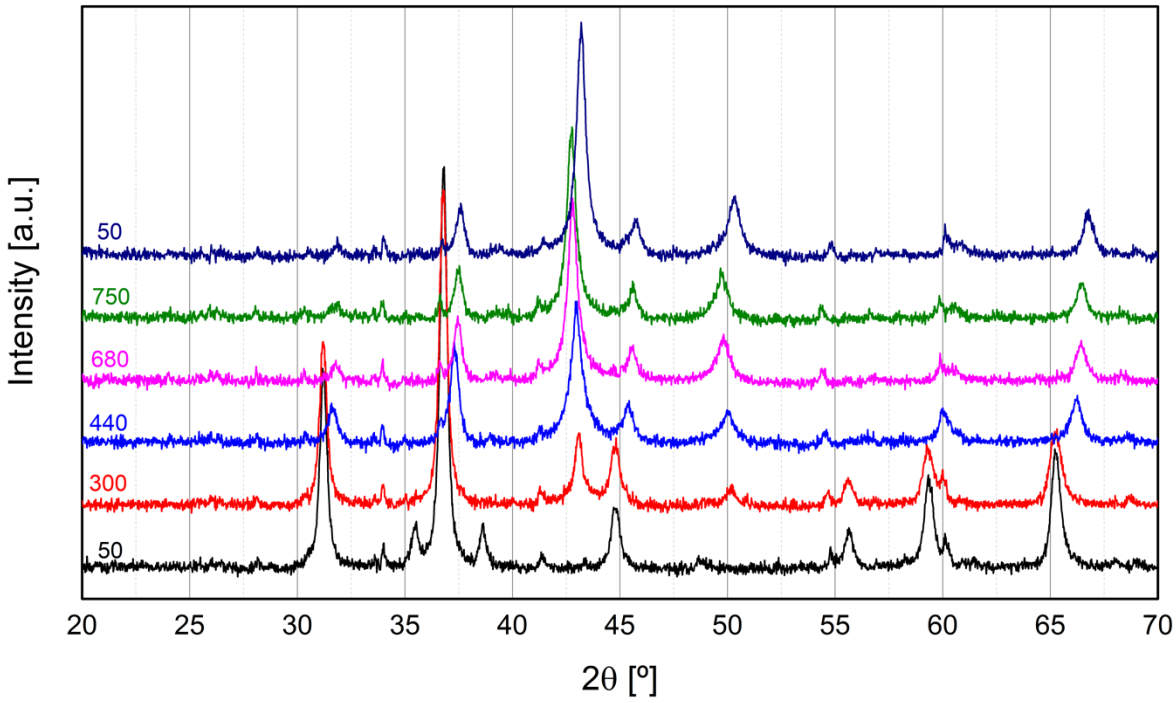

Figure 27 In situ XRD patterns of $CuAl_2O_4$ under 5% H_2/N_2. XRD taken in isothermal conditions at different temperature: 50 – 300 - 440 - 680 - 750 ºC. First pattern (from the top) was taken at room temperature after all the treatments.

3.3.3 Temperature Programmed Reduction analysis

Temperature programmed reduction (TPR) experiments were conducted on calcined powders according to the general procedure described in Chapter 2.5. The reducibility of $CuFe_2O_4$, $CuFeAlO_4$ and $CuAl_2O_4$ samples were examined by H_2-temperature programmed reduction measurements (Figure 28)

Two peaks are observed on the curves of $CuFe_2O_4$ and $CuFeAlO_4$, it meant that the reduction process proceeds at least in two steps. In agreement with the previous *in situ* XRD analysis, $CuAl_2O_4$ presents an impurity peak at ~200 ºC due to the reduction of CuO to Cu^0 [12]. First of all, the temperatures where the reductions begin, were evaluated. From the *in situ* XRD analysis, the hypothesis that increasing the amount of Al^{3+} in the lattice leads to a more stable spinel, is confirmed also by TPR measurements. $CuFe_2O_4$ (red) presents the lowest temperature of reduction (~320 ºC) and the higher H_2 consumption, indicative of a sample that is very unstable at high temperature and under reducing environment. The shape of the first peak, responsible of the process $Cu^{2+} > Cu^0$ [13] hide two possible explanation:

- the presence of Cu^{1+} inside the lattice: very uncommon for spinel structures and in conflict with the H_2 consumption.
- different crystal sizes dimensions have different reduction temperatures.

The iron starts to leave the structure at 450 ºC to be completely reduced to Fe^0 at 750 ºC (Chapter 3.3.2). *Viceversa*, despite the presence of the CuO peak, $CuAl_2O_4$ (green) exhibit the higher reduction temperature, and the total absence of reduction above 500 ºC caused by a

whole iron substitution. The shoulder present at ~420 ºC could be explained by the difficult to extract Cu^{2+} beyond a certain amount due to the tenacity of the system.

Table 3 Comparison between theoretical and experimental H_2 consumption during TPR analysis.

sample	Theoretical H_2 consumption (mol)	Measured H_2 consumption (mol)
$CuFe_2O_4$	0.001570	0.001590
$CuFeAlO_4$	0.001190	0.001200
$CuAl_2O_4$	0.00028	0.00110

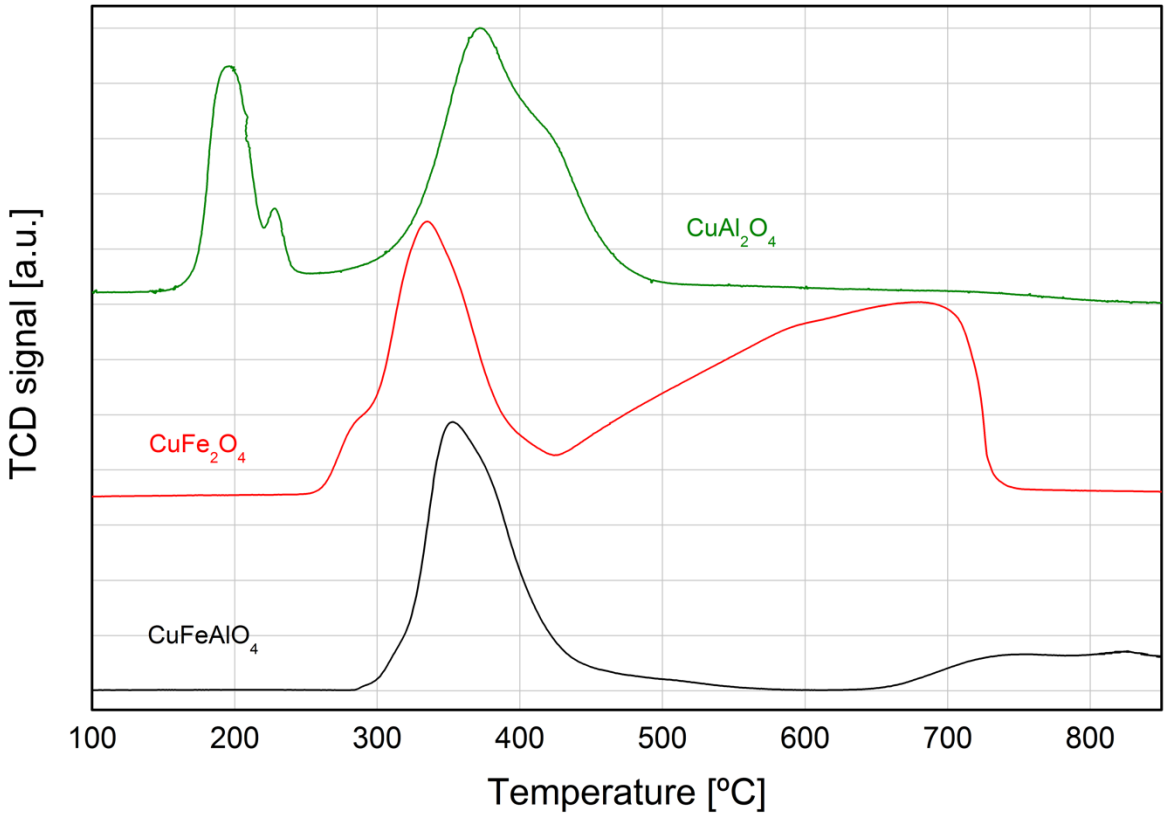

Figure 28 H_2-TPR profiles of the synthesized spinels. Different Al content led to different reduction process and temperature.

Eventually $CuFeAlO_4$ (black) is the synthesized spinel that have good stability at high temperature and a reasonable reduction temperature for RWGS and TWC application. As showed by the *in situ* XRD, Cu^{2+} start to reduce at 300 ºC to form a separate metallic phase. Although the reduction of iron is limited but not equal to zero, demonstrable by the presence of hydrogen consumption at 500 ºC (Fe^{3+} to Fe^{2+}) and above 700 ºC (Fe^{2+} to Fe^{0}) [14] suggesting that take place anyway.

Reversibility of $CuFe_2O_4$

TPR-like measurements were carried out using the *in situ* XRD setup. In Figure 29, a scheme of the thermal program used for this analysis is reported highlighting all the steps. TPR measurement (5% H_2/N_2) followed by a TPO (20% O_2/N_2) and record the phase transition with the XRD.

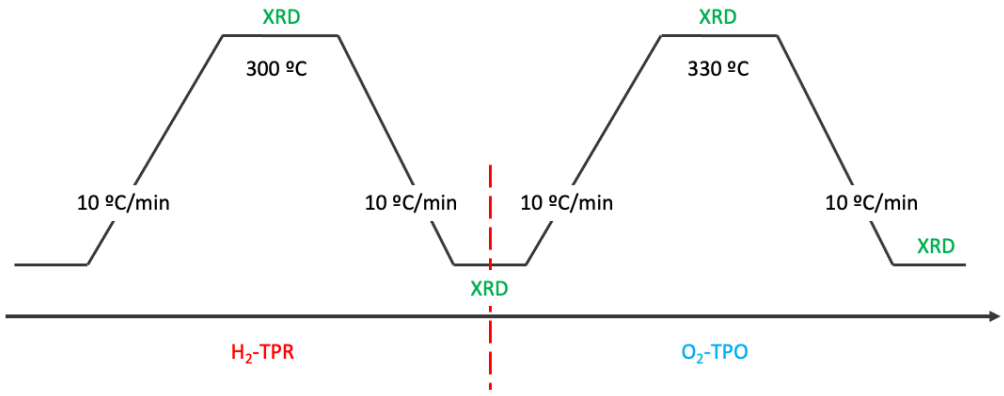

Figure 29 Schematic representation of the program used to verify $CuFe_2O_4$ reversibility.

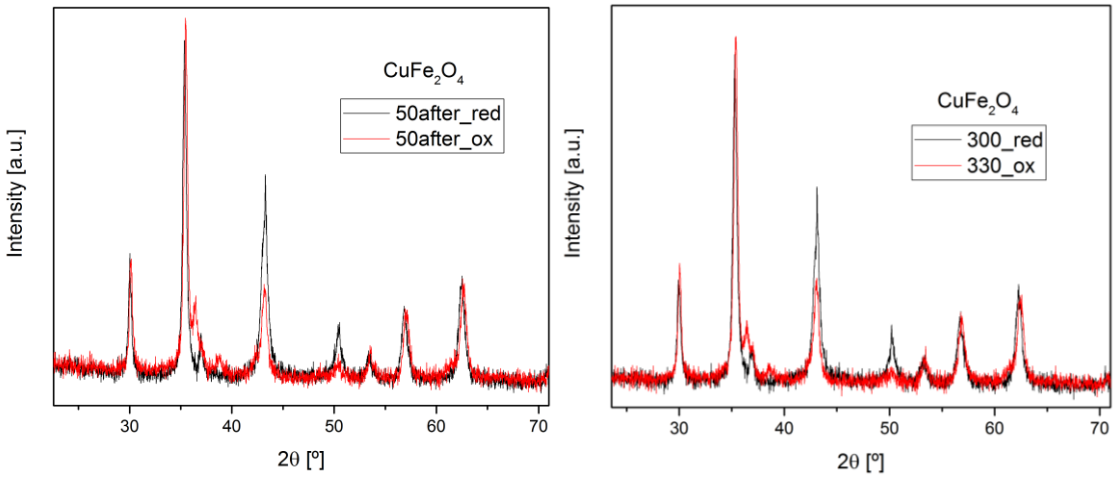

Figure 30 In situ XRD of $CuFe_2O_4$ after a TPR-TPO process to evaluate its reversibility. Reduction step: 300 ºC in 5% H_2/N_2 for 1h. Oxidation step: 330 ºC in 20% O_2/N_2 for 1h.

As expected, the system $CuFe_2O_4$ is not reversible: when copper is extract from the lattice is remarkably difficult to reinsert the cations inside the crystallographic structure [15]. To better understand, Figure 30 shows the results of the consequential TPR-TPO measurements. First of all, in reducing environment the extraction of Cu from $CuFe_2O_4$ causes the rearrangement of the crystallographic structure from tetragonal to cubic. During the reduction process, Cu^{2+} is extract from the spinel system. In addition, in Chapter 3.3.2 was illustrated that more aluminum is inside the lattice, less copper is extract from the structure. After the TPR measurement, (black patterns) the peak at 42 º 2θ grows in intensity due to the presence of metallic copper. While, as a result of the TPO, the oxidation of copper stopped to the intermediate Cu_2O (36 º 2θ) instead oxidize to the more stable CuO.

3.3.4 X-ray Absorption Spectroscopy analysis

Direct information on the oxidation states of Fe and Cu in the various spinels samples was obtained from X-ray absorption spectroscopy (XAS).

In Figure 31 Cu K-edge and Fe K-edge of a set of Cu^{2+} Cu^{1+} Cu^0 and Fe^{3+} Fe^{2+} Fe^0 references compounds which clearly demonstrate the differences in all aspects related to the pre-edge

edge and post-edge features of these selected compounds.

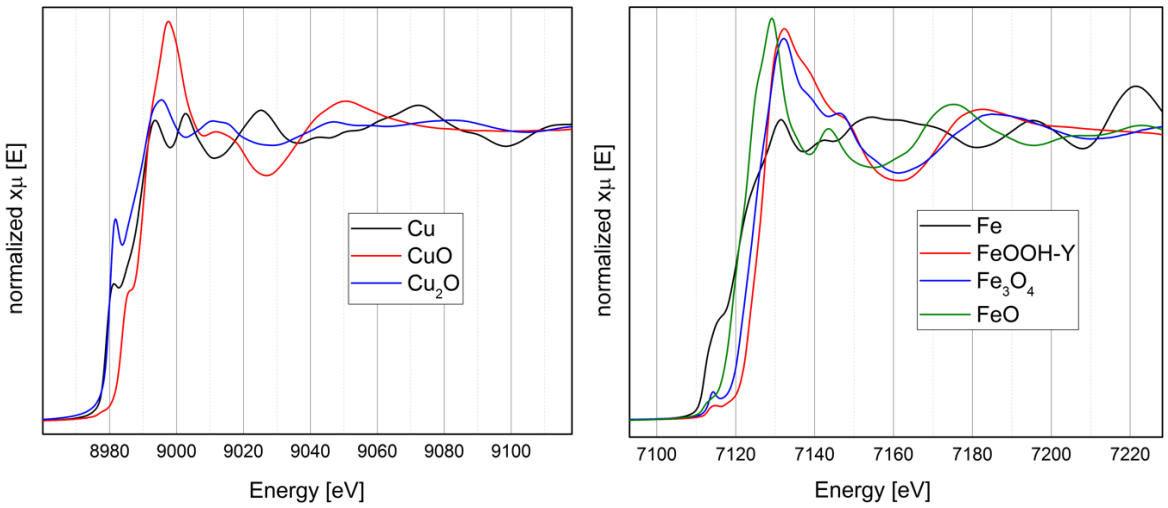

Figure 31 The Cu K-edge and Fe K-edge spectra of selected reference compounds

This also demonstrates that the XAS technique can unravel differences in the spectra which appears to be related to different local geometries. Comparison was performed on the normalized Cu K-edge and Fe K-edge data of all the spinel system (reduced and fresh).

There are three regions of interest in a typical XAS spectrum:

1. the pre-edge which is due to the 1s to 3d transition and has been noted to be sensitive to the local coordination geometry [16].
2. the edge position through the midway of the rising absorption edge which is known to be sensitive to the oxidation state of the metal ions of interest [17]
3. the so-called "white-line" (intensity at the top of the edge) [18] [19] which is known to show differences depending on the nature of the local coordination geometry.

Measurements were carried out on fresh and reduced samples. The reduction procedure was the same for each sample: temperature ramp with 5% H_2/Ar from RT to 350 ºC. As showed

in Chapter 3.3.3, 350 ºC is the temperature of the first reduction peak of copper from Cu^{2+} to Cu^{0}. Furthermore, 350 ºC was the temperature chosen for the catalytic activation before testing spinels for RWGS and TWC reactions.

Cu K-edge

The references used are characterized by different local coordination environment ranging from FCC (Cu^{0}), linear (Cu_2O) and the most common in the synthesized spinel, distorted octahedral (CuO) [20].

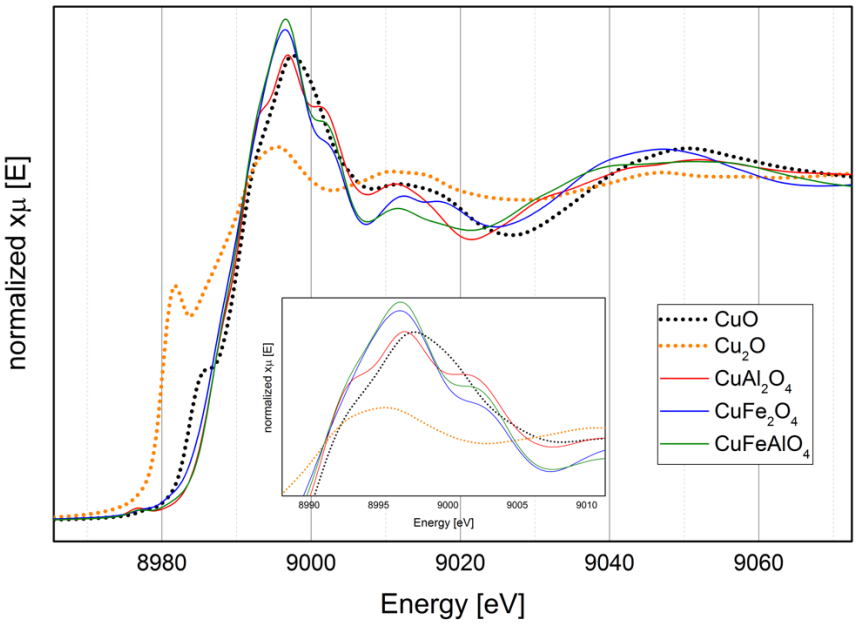

Figure 32 XAS Cu K-edge spectra of $CuFe_2O_4$, $CuFeAlO_4$, $CuAl_2O_4$ without the reduction treatment. CuO and Cu_2O as reference.

Figure 32 shows the Cu K-edge XAS spectra of the three spinel catalysts as-synthesized and without the reduction treatment. The Cu K-edge XANES spectra of all the studied samples are represented by a single intense peak at the absorption edge (1s → 4p transition). Comparison of the position of the Cu K-edge and the shape of the references and the catalysts suggests that that Cu is present in the catalysts mostly in the Cu^{2+} state. In fact, the

shape of the Cu K-edge XAS spectra significantly depends on the chemical state of copper. Copper oxidation leads to a shift of the edge toward higher energies, which indicates the presence of a positive charge on the copper atoms. The value of the shift depends on the charge state of Cu. The absorption edge in the spectrum of Cu_2O, where copper is in the Cu^{1+} state, is shifted toward higher photon energies (~8980 eV); in addition, the spectrum exhibits an intense shoulder at 8981 eV [21]. The appearance of a shoulder at the absorption edge is attributed to the 1s → 4p transition arising from the transfer of outer-shell electrons to an inner-shell vacancy, the so-called "shakedown" electronic transitions [22]. The Cu^{2+} atoms have a partially filled 3d electron shell. The XAS spectra of these compounds are characterized by the presence of a low-intensity peak in the pre-edge region of the spectrum and a shoulder at the absorption edge. The pre-peak corresponds to the 1s → 3d dipole-forbidden quadrupole transitions arising from the hybridization of the p and d orbitals of copper [23].

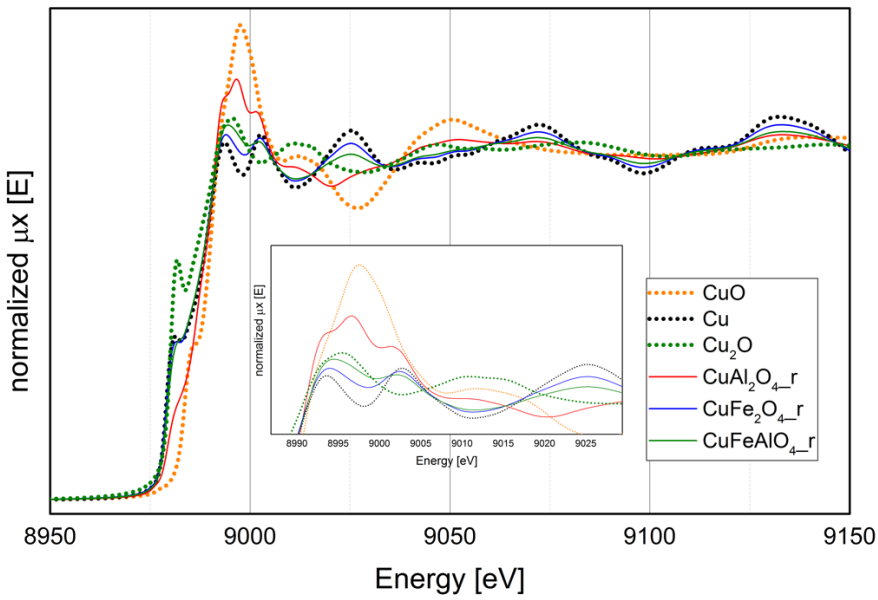

Figure 33 XAS Cu K-edge spectra of $CuFe_2O_4$, $CuFeAlO_4$, $CuAl_2O_4$ without reduction treatment (5% H_2/Ar, 350 ºC, 1h). Metallic Cu, CuO and Cu_2O as reference.

To better understand the evolution of catalysts during reaction, Figure 33 shows the Cu K-edge XAS spectra of catalysts after the reduction treatment (5% H_2/Ar, 350 ºC, 1h). As showed by the *in situ* XRD (Chapter 3.3.2) and TPR measurements (Chapter 3.3.3), copper tends to migrate from structure to the surface forming nanoparticles. In particular, less aluminum is present as iron dopant, more Cu^{2+} tends to leave the spinel structure. From XAS measurements the same results are obtained. From Figure 33 is evident the tendency of $CuFe_2O_4$ and $CuFeAlO_4$ to have the same energy at the edge position. Completely different is the situation for the spinel without the Fe, which behaves like no reduction occurred. Comparing the spinels with the reference, is evident to notice the good matching of $CuFe_2O_4$ and $CuFeAlO_4$ to follow the signal of metallic Cu, confirming the reduction of the system.

To evaluate the entity of the reduction, linear combination fitting (LCF) spectra was performed in the range -20 eV < E_0 < 30 eV around the absorption edge to quantify the fraction of each Cu species present. Reference compounds for each fit usually included Cu foil (Cu^0), CuO (Cu^{2+}), Cu_2O (Cu^{1+}) and the calcined relative spinel.

Table 4 Values from linear combination fit between reduced samples, references and as-synthesized.

%	Cu foil (Cu^0)	CuO (Cu^{2+})	Cu_2O (Cu^{1+})	As-synthesized
$CuFe_2O_4$	0.755	0.034	0.162	0.048
$CuFeAlO_4$	0.573	0.083	0.274	0.070
$CuAl_2O_4$	0.202	0.038	0.242	0.518

Table 4 shows the values deriving from linear combination fit calculated on reduced samples. As-synthesized spinels and references, were used for the fit. Also in this case, more

aluminum is inside the spinel and more the reduction process fatigue to extract copper from the lattice: in $CuFe_2O_4$ almost all the copper is reduced to Cu^0 (0.755), instead in $CuAl_2O_4$ the most present copper after reduction is the Cu inside the spinel structure (0.518). LCF calculations evidenced an important process missed from XRD. The presence of Cu^{1+} in all the samples, from this calculation, is not neglectable and two possible explanations could explain the inconsistency of data from XRD and XAS:

1. XAS measurements was performed *ex situ* thus, during all the preparation steps from the reduction treatments to measurements, part of Cu oxidized to Cu_2O.
2. The Cu_2O is not visible at the XRD due to its amorphous nature.

Starting from my experience and taking into consideration the high concentration of Cu^{1+}, the more plausible explanation is the presence of the copper (I) oxide as amorphous phase. One possible way to totally understand copper path (Cu^{2+} > Cu^{1+} >Cu^0) and its evolution during reaction is *in situ* and *operando* measurements.

Fe K-edge

The Fe K-edge XAS spectrums of the reduced catalyst is similar to the spectrum of Fe_3O_4, where the iron atoms are in the Fe^{3+} state (Figure 34). The spectrum exhibits a broad pre-edge peak at 7114 eV and an intense peak at the absorption edge at 7133 eV, which is characteristic of Fe^{3+} cations in an octahedral oxygen environment [24] [25].

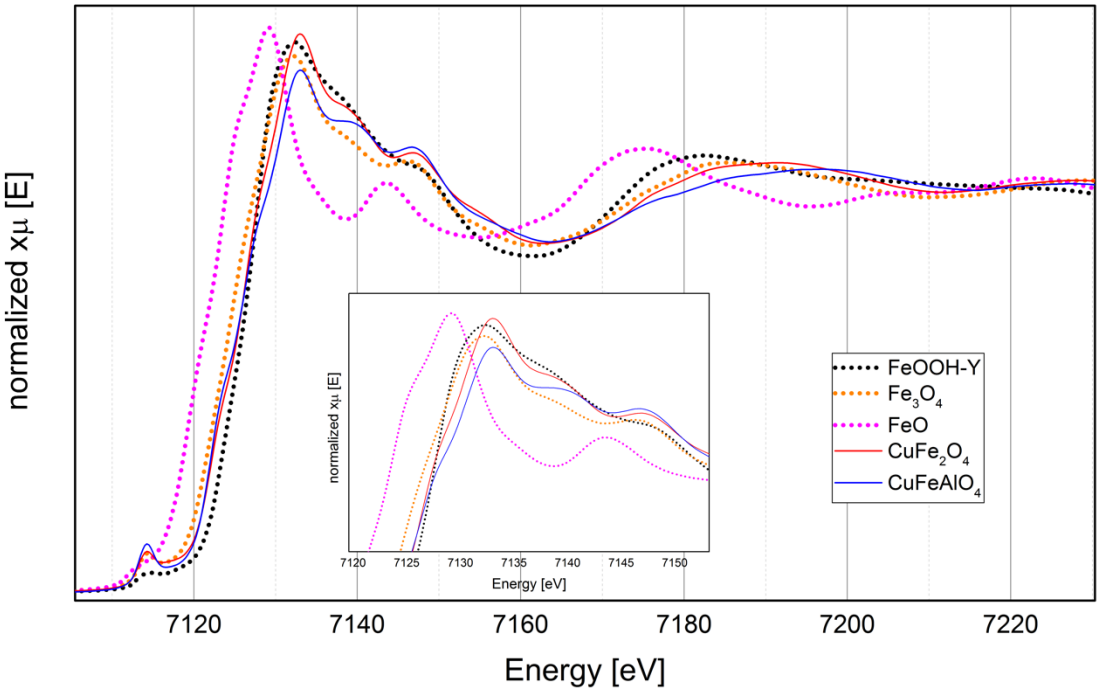

Figure 34 XAS Fe K-edge spectra of $CuFe_2O_4$ and $CuFeAlO_4$, without the reduction treatment. FeO, Fe_3O_4 and FeOOH-Y as references.

The energy shift of the absorption threshold as a result of the different Fe–O bond lengths (the shorter the interatomic distance, the higher the edge energy), which gives a hint on the different oxidation state of the Fe ions (Fe^{2+} and Fe^{3+}) [26].

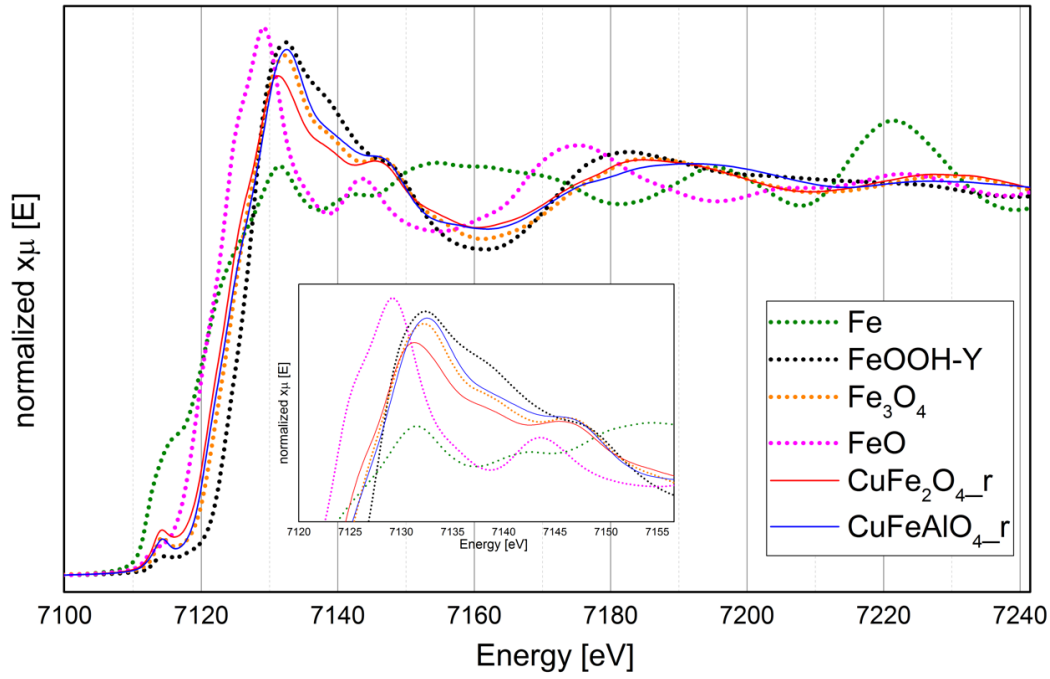

Figure 35 XAS Fe K-edge spectra of $CuFe_2O_4$ and $CuFeAlO_4$, with the reduction treatment (5% H_2/Ar, 350 ºC, 1h). Metallic Fe, FeO, Fe3O4 and FeOOH-Y as references.

XAS measurements of reduced samples were performed also for the Fe K-edge, as summarized in Figure 35. Fe cations are spread out in the spinel structure occupying octahedral and tetrahedral sites (Table 5). When copper leaves the spinel structure, some Fe^{3+} ions in the tetrahedral sites migrate to octahedral positions, changing their oxidation state to +2 and hence the partial reduction of the metal observed by XAS [27].

Table 5 Values from linear combination fit between reduced samples, references and as-synthesized.

%	Fe foil (Fe^0)	FeO (Fe^{2+})	Fe_2O_3 (Fe^{3+})	FeOOH-Y	As-synthesized
$CuFe_2O_4$	0.053	0.422	0.182	0	0.342
$CuFeAlO_4$	0	0.052	0.274	0	0.349

Also in this case, XAS measurements corroborate the previous analysis. From TPR and *in situ* XRD investigation it was possible to determine the stability, under reducing environment, of all spinels below 350 ºC. Unlike Cu, iron cations tends to stay inside the lattice and only at higher temperature all the spinels start to decompose following different ways, depending on the aluminum quantities. Iron can change its position, from tetrahedral to octahedral, during the reducing process. The possibility of iron ions to change oxidation state and occupancy inside the lattice could be extremally important in the two different applications chosen in this thesis: Solid Oxide Cells and Heterogeneous catalyst.

3.3.5 Reverse Water Gas Shift reaction results

The main reaction studied is the reversible and exothermic water gas shift reaction (WGSR):

$$CO + H_2O \rightleftharpoons CO_2 + H_2$$

In the previous chapters, all the techniques used to characterize the spinels were necessary to understand how the system change during reaction. TPR technique allowed to evaluate at which temperature and how much of the spinels are reduced by hydrogen. Starting from that information the critical and fundamental temperature used to activate the catalysts before reaction, was chosen. The catalyst activation, as it will be seen in this chapter, is extremally important to activate the spinel extracting Cu from the lattice and boost the performance towards reverse water gas shift reaction. With *in situ* XRD the precise crystallographic phase that is present during the catalyst activation, was evaluated. Eventually, XAS technique has highlighted the presence of amorphous phase undetectable with XRD. To better understand the behavior of spinels under the activation phase, Scanning Electron Microscopy (SEM) was used to evaluate the morphology of as-synthesized and activated spinels. The activation process was done under 5 % H_2/Ar at 350 ºC for 1h.

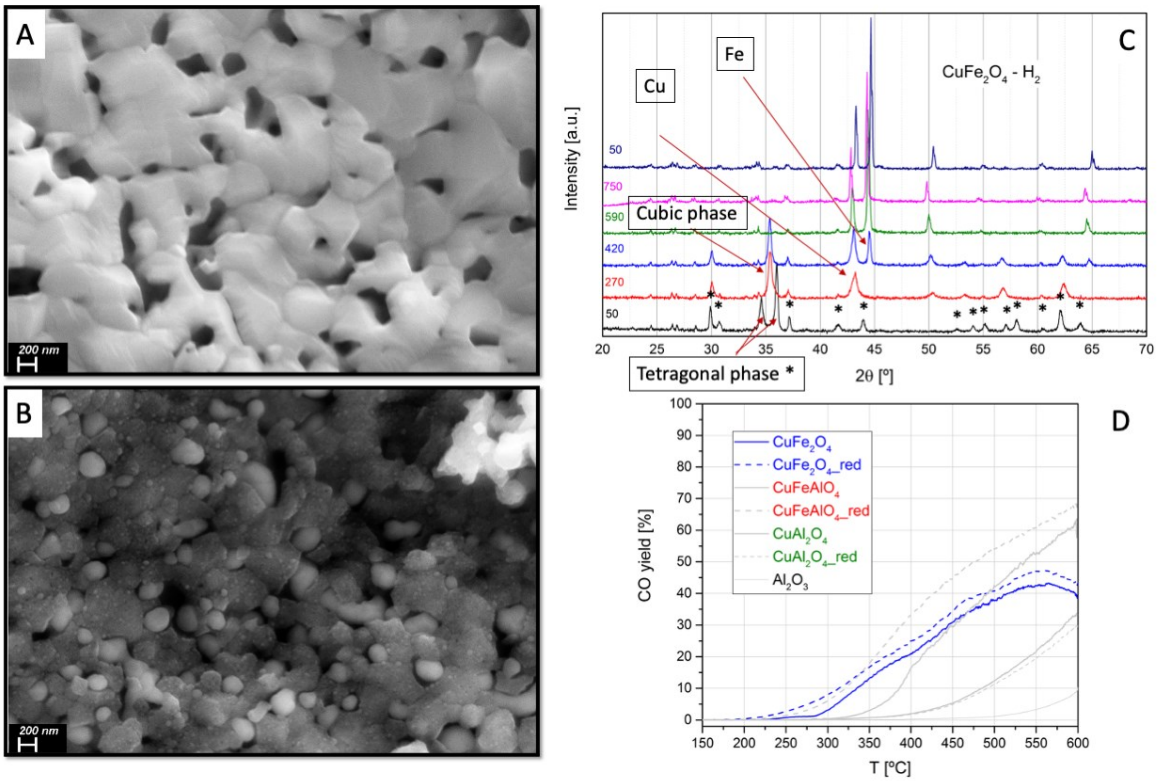

Figure 36 A) SEM image of $CuFe_2O_4$ as-synthesized. B) SEM image of $CuFe_2O_4$ after reduction (5% H_2/Ar, 350 ºC). C) In situ XRD during reduction (5 % H_2/N_2): at 270 ºC copper start to migrate from lattice forming metallic particles. D) CO yield during RWGS: after 500 ºC performance decrease due to decomposition of $CuFe_2O_4$ in metallic Cu and metallic Fe.

Figure 36 summarizes the performance of $CuFe_2O_4$ and its behavior during activation phase and reaction. From SEM images it was possible to evaluate the morphology of the spinel and understand two important processes: the activation of the phase and its deactivation at high temperature. As showed in the previous chapter, $CuFe_2O_4$ starts to reduce under reducing environment between 250-350 ºC due to the segregation of metallic Cu. The morphology changes drastically and corroborate the XRD data, where massive peaks related to metallic Cu and Fe appear above 400 ºC. The increasing temperature and the reaction condition contribute to deactivate the spinel due to its instability caused by the complete Fe reduction. At temperatures higher than 500-550 ºC, spinel structure is completely lost and the ability of catalyzed the RWGS reaction start to decrease, as showed in Figure 36 (D). But if at high

temperature the spinel ability to reduce itself is a drawback, at low temperature is the opposite. Again, the possibility to extract part of the Cu results to be a strategy to form an *in situ* catalyst able to activate the CO_2, increasing the performance at lower temperature. Precisely, if $CuFe_2O_4$ is activated (5% H_2/Ar, 350 ºC, 1h) the overall performance increase and the light off temperature decrease of ~60 ºC. The possible explanation may be found in the metallic copper already outside the spinel structure, thus able to activate CO_2 or in the increment of the surface area during the activation process. Indeed, before $CuFe_2O_4$ activation BET analysis reveal a surface area of 5 m^2/g and after a modest increment up to 9 m^2/g is observed

The $CuFe_2O_4$ suggests the possibility to exploit its particular behavior. To overcome the high temperature problem and try to preserve the activation properties, aluminum doping was performed in $CuFe_2O_4$, as showed in the previous chapter.

The first considerable difference of $CuFeAlO_4$ with respect to $CuF2O4$ concerns the dimension of the Cu particles after the activation phase, showed in Figure 17 (B). The spinel system without Al is unable to sustain severe reducing environment losing its crystallographic structure and forming pure copper and iron in the metallic form. From the SEM images, less particles characterized by very high dimension (~200 nm) are observed to form. Instead, if the spinel is doped with aluminum, in particular if just half of the iron is substitute, the structure is stable and suitable for high temperature application [5]. More stable, from a general point of view, means less able to change after receiving an input (reducing environment).

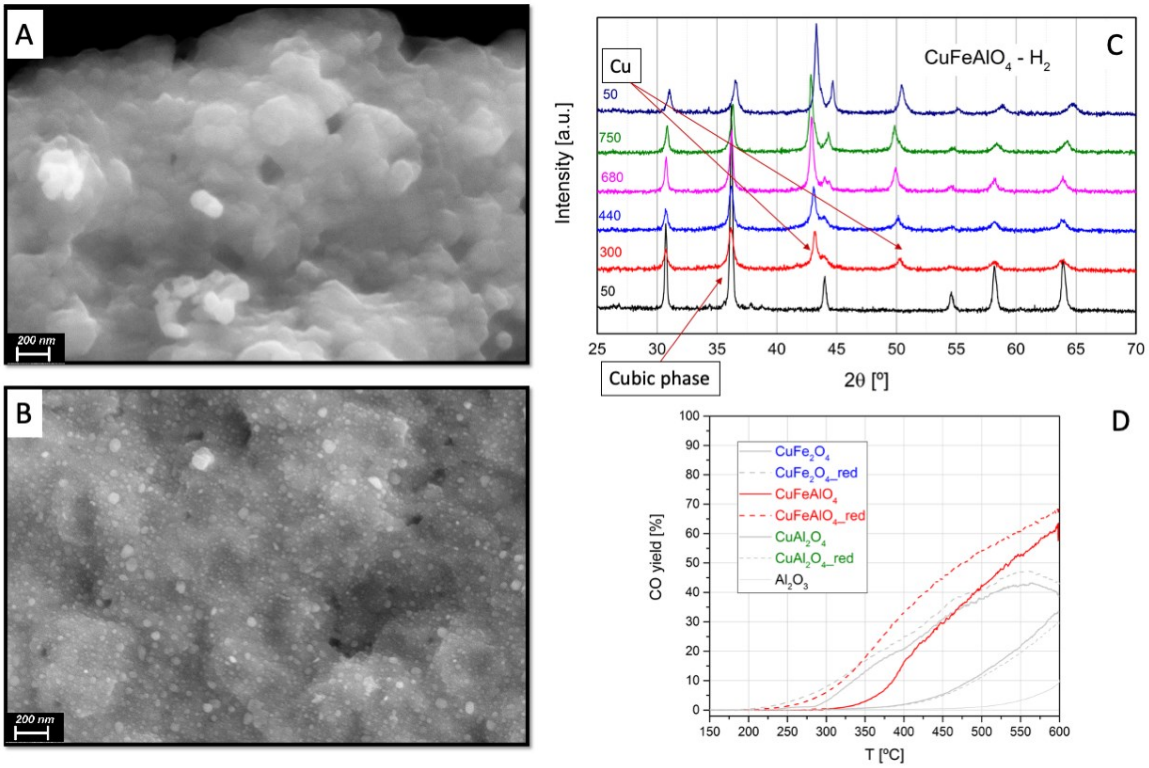

Figure 37 A) SEM image of $CuFeAlO_4$ as-synthesized. B) SEM image of $CuFeAlO_4$ after reduction (5% H_2/Ar, 350 ºC). C) In situ XRD during reduction (5 % H_2/N2): at 300 ºC copper start to migrate from lattice forming metallic particles. D) CO yield during RWGS with (dotted line) and without (normal line) the activation phase.

From the morphological point of view (SEM) $CuFeAlO_4$ is more stable than its counterpart without Al, and the same activation process produces a different result: instead of losing the structure, just a limited part of Cu leaves the lattice forming a field of organized nanoparticles (~5-20 nm) on the surface of the remaining spinel. The possibility of creating a new catalyst *in situ* with an active phase, lead to have different behaviors even if the reaction condition is the same. In Figure 37 (D) is possible to see how the activation process increase dramatically the spinel performance, deceasing of almost 100 ºC the light off temperature and reaching a CO_2 conversion of 70% at 600 ºC. For the $CuFeAlO_4$, the formation of the *in situ* catalyst during the activation step, increase the surface area, calculated with BET, from 6 m^2/g to 22 m^2/g.

By combining the previous characterization and RWGS results, It could be possible to hypothesize that the Cu^{1+} presence, highlighted from XAS measurements, may play an important role during reaction [28]. It is not just the presence of Cu^{1+} that activate the CO_2 during the RWGS but, probably, the continuous alternating process that Cu undergo ($Cu^{2+} \leftrightarrow Cu^{1+} \leftrightarrow Cu^{0}$). Unfortunately, a more confident statement required *in situ* and *operando* technique.

Eventually, the performance during reverse water gas shift of all the studied spinel is summarized in Figure 38. The aluminum content inside the structure is fundamental from the performance point of view. With the total substitution of Fe with Al, the structure is completely inert and stack in the as-synthesized form, unable to respond at the stimulus that the environment may give (green lines). On the contrary, without Al, the system is at the mercy of the outside stimulus and if the environment is unacceptably hard, the spinel vanishes leaving only its metallic part (blue lines). Equilibrium is the key word of this work: not too much, not too little. With the right amount of Al inside the structure, the spinel may reduce itself just in the quantity necessary to resist and respond to the external stimulus, staying sufficiently stable to continue its path in the reaction process (red lines).

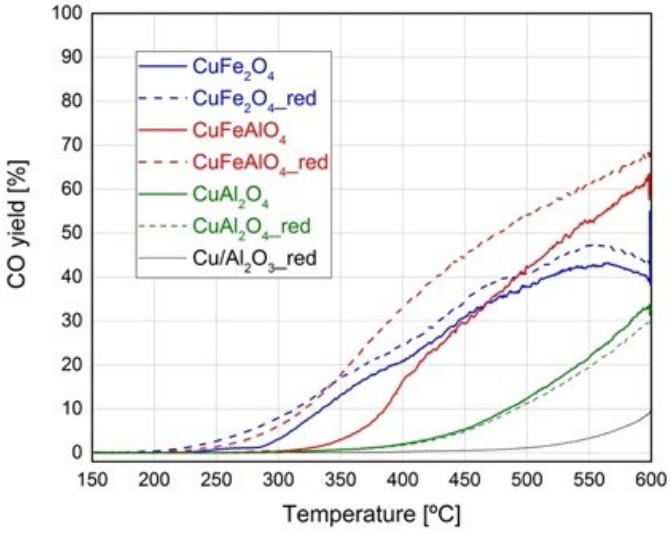

Figure 38 Comparison of CO yield of the studied spinel during RWGS. Cu/Al_2O_3 as benchmark. Dotted line: spinel activated (5% H_2/Ar, 350 ºC, 1h). Normal line: spinel as-synthesized.

3.4 Conclusion

$CuFe_2O_4$, $CuFeAlO_4$ and $CuAl_2O_4$ spinel materials were proposed as active and stable catalysts for the catalytic hydrogenation of CO_2 to CO, also known as the Reverse Water Gas Shift (RWGS) reaction. In this chapter, the activity of spinel oxides as catalysts for this reaction was investigated by comparing the effect of the aluminum content between the three spinels. $CuFeAlO_4$ outperformed all other spinels studied in the range of temperatures (100 ºC–600 ºC). Further investigation of the catalysts with *in situ* XRD showed that $CuFeAlO_4$ spinel is the most balanced under reducing environment: enough to allow the Cu extraction without losing its structural integrity. Furthermore, XAS measurements of as-synthesized and activated spinel showed the presence of Cu^{1+} as amorphous phase, a good candidate as promoter for the CO_2 activation during RWGS. In all the cases, the activation process reveled the increasing of the performance due to the Cu extraction from the lattice. The key factor is the presence ($CuFeAlO_4$ – $CuAl_2O_4$) or not ($CuFe_2O_4$) of aluminum and its quantity. Indeed, the initial synthesis of the catalyst is crucial to provide the desired

properties. In spite of this, it is only the combination of synthesis and reaction process that is possible to achieve what is wanted.

3.5 Bibliography

[1] H. C. Shin, S. C. Choi, K. D. Jung, and S. H. Han, "Mechanism of M ferrites (M = Cu and Ni) in the CO2 decomposition reaction," *Chem. Mater.*, vol. 13, no. 4, pp. 1238–1242, 2001.

[2] D. Fino, N. Russo, G. Saracco, and V. Specchia, "Catalytic removal of NOx and diesel soot over nanostructured spinel-type oxides," *J. Catal.*, vol. 242, no. 1, pp. 38–47, 2006.

[3] B. Lavina, G. Salviulo, and D. Della Giusta, "Cation distribution and structure modelling of spinel solid solutions," *Phys. Chem. Miner.*, vol. 29, no. 1, pp. 10–18, 2002.

[4] J. E. Tasca, C. E. Quincoces, A. Lavat, A. M. Alvarez, and M. G. González, "Preparation and characterization of CuFe2O4 bulk catalysts," *Ceram. Int.*, vol. 37, no. 3, pp. 803–812, 2011.

[5] F. A. Abuilaiwi, M. Awais, U. Y. Qazi, F. Ali, and A. Afzal, "Al3+ doping reduces the electron/hole recombination in photoluminescent copper ferrite (CuFe2-xAlxO4) nanocrystallites," *Bol. la Soc. Esp. Ceram. y Vidr.*, pp. 1–11, 2020.

[6] V. K. Lakhani and K. B. Modi, "Al3+-modified elastic properties of copper ferrite," *Solid State Sci.*, vol. 12, no. 12, pp. 2134–2143, 2010.

[7] "Bestimmung der Grösse und der inneren Struktur von Kolloidteilchen mittels Röntgenstrahlen. Nachrichten von der Gesellschaft der Wissenschaften zu Göttingen," pp. 98–100, 1918.

[8] K. Faungnawakij, N. Shimoda, T. Fukunaga, R. Kikuchi, and K. Eguchi, "Crystal structure and surface species of CuFe2O4 spinel catalysts in steam reforming of dimethyl ether," *Appl. Catal. B Environ.*, vol. 92, no. 3–4, pp. 341–350, 2009.

[9] M. J. Iqbal, N. Yaqub, B. Sepiol, and B. Ismail, "A study of the influence of crystallite size on the electrical and magnetic properties of $CuFe_2O_4$," *Mater. Res. Bull.*, vol. 46, no. 11, pp. 1837–1842, 2011.

[10] I. I. Simentsova, V. I. Zaikovskii, L. S. Dovlitova, N. V. Shtertser, and L. M. Plyasova, "Heat treatment-induced compositional and structural changes in the preparation of $CuCrAlO_4$ and $CuFeAlO_4$," *Inorg. Mater.*, vol. 52, no. 12, pp. 1259–1265, 2016.

[11] J. Riley, R. Siriwardane, H. Tian, W. Benincosa, and J. Poston, "Particle scale modeling of $CuFeAlO_4$ during reduction with CO in chemical looping applications," *Appl. Energy*, vol. 251, no. December 2018, p. 113178, 2019.

[12] G. Carollo, A. Garbujo, A. Bedon, D. Ferri, M. M. Natile, and A. Glisenti, "Cu/CGO cermet based electrodes for Symmetric and Reversible Solid Oxide Fuel Cells," *Int. J. Hydrogen Energy*, vol. 45, no. 25, pp. 13652–13658, 2020.

[13] J. Marrero-Jerez, E. Chinarro, B. Moreno, J. Peña-Martínez, and P. Núñez, "CGO20–CuO composites synthesized by the combustion method and characterized by H_2-TPR," *Ceram. Int.*, vol. 41, no. 9, pp. 10904–10909, 2015.

[14] M. J. Tiernan, P. A. Barnes, and G. M. B. Parkes, "Reduction of iron oxide catalysts: The investigation of kinetic parameters using rate perturbation and linear heating thermoanalytical techniques," *J. Phys. Chem. B*, vol. 105, no. 1, pp. 220–228, 2001.

[15] K. T. Wu and T. Ishihara, "Spinel-based oxide cathode used for high temperature CO_2/H_2O co-electrolysis," *Solid State Ionics*, vol. 329, no. October 2018, pp. 46–51, 2019.

[16] K. I. Shimizu, H. Maeshima, H. Yoshida, A. Satsuma, and T. Hattori, "Ligand field effect on the chemical shift in XANES spectra of Cu(II) compounds," *Phys. Chem. Chem. Phys.*, vol. 3, no. 5, pp. 862–866, 2001.

[17] M. Fernández-García, "XANES analysis of catalytic systems under reaction conditions," *Catal. Rev. - Sci. Eng.*, vol. 44, no. 1, pp. 59–121, 2002.

[18] J. L. DuBois, P. Mukherjee, T. D. P. Stack, B. Hedman, E. I. Solomon, and K. O. Hodgson, "A systematic K-edge X-ray absorption spectroscopic study of Cu(III) sites," *J. Am. Chem. Soc.*, vol. 122, no. 24, pp. 5775–5787, 2000.

[19] N. C. Tomson *et al.*, "Re-evaluating the Cu K pre-edge XAS transition in complexes with covalent metal-ligand interactions," *Chem. Sci.*, vol. 6, no. 4, pp. 2474–2487, 2015.

[20] E. M. C. Alayon, M. Nachtegaal, E. Kleymenov, and J. A. Van Bokhoven, "Determination of the electronic and geometric structure of Cu sites during methane conversion over Cu-MOR with X-ray absorption spectroscopy," *Microporous Mesoporous Mater.*, vol. 166, pp. 131–136, 2013.

[21] W. B. Kim and J. S. Lee, "Quantitative XANES analysis of cuprous dibromide complex formed in the oxidative carbonylation of phenols," *J. Phys. Chem. B*, vol. 107, no. 35, pp. 9195–9202, 2003.

[22] N. Kosugi, T. Yokoyama, K. Asakura, and H. Kuroda, "Polarized Cu K-edge XANES of square planar $CuCl_4^{2-}$ ion. Experimental and theoretical evidence for shake-down phenomena," *Chem. Phys.*, vol. 91, no. 2, pp. 249–256, 1984.

[23] J. E. Hahn, R. A. Scott, K. O. Hodgson, S. Doniach, S. R. Desjardins, and E. I. Solomon, "Observation of an electric quadrupole transition in the X-ray absorption spectrum of a Cu(II) complex," *Chem. Phys. Lett.*, vol. 88, no. 6, pp. 595–598, 1982.

[24] C. Piquer, M. A. Laguna-Marco, A. G. Roca, R. Boada, C. Guglieri, and J. Chaboy, "Fe K-edge X-ray absorption spectroscopy study of nanosized nominal magnetite," *J. Phys. Chem. C*, vol. 118, no. 2, pp. 1332–1346, 2014.

[25] M. Okube *et al.*, "Site occupancy of Fe^{2+}, Fe^{3+} and Ti^{4+} in titanomagnetite

determined by valence-difference contrast in synchrotron X-ray resonant scattering," *J. Synchrotron Radiat.*, vol. 25, no. 6, pp. 1694–1702, 2018.

[26] H. B. Venkata Krishnan, Ramakrishnan Kalai Selvan, Chanassary Ouso Augustin, Aharon Gedanken, "EXAFS and XANES Investigations of CuFe2O4 Nanoparticles and CuFe2O4-MO2 (M) Sn, Ce) Nanocomposites," *J. Phys. Chem.*, vol. 111, no. 1, pp. 16724–16733, 2007.

[27] J. G. Chen, "NEXAFS investigations of transition metal oxides, nitrides, carbides, sulfides and other interstitial compounds," *Surf. Sci. Rep.*, vol. 30, no. 1–3, pp. 1–152, 1997.

[28] M. Estrella *et al.*, "In situ characterization of CuFe2O4 and Cu/Fe 3O4 water-gas shift catalysts," *J. Phys. Chem. C*, vol. 113, no. 32, pp. 14411–14417, 2009.

Chapter 4

"Without struggle, no progress and no result.

Every breaking of habit produces a change in the machine."

G.I. Gurdjieff

4.1 Introduction

Three-way catalysts (TWCs) are exploited to control the emissions of gasoline vehicles [1]. Their engines are operated efficiently at stoichiometry, *i.e.* close to an air-to-fuel ratio equal to 14.6, commonly referred to as λ =1 [2]. The development of new formulations is an important step for automotive industry and development of new TWC technology has been critical in the past few years due to the newer stringent regulations [3]. Indeed, the development of more efficient catalysts depends on a complete understanding of the various parameters related to three-way catalyst design and formulation [4]. Normally, gasoline engine exhaust composition can vary based on the engine and driving conditions, but typical values of the exhaust gases are 0.5 vol% CO, 3500 ppm HCs, 900 ppm NOx, 0.17 vol% H_2, 10 vol% H_2O, 10 vol% CO_2, 0.5 vol% O_2, and the balance N_2 [5].

Satisfactory control of the previous emission can be achieved with a TWC via the simultaneous oxidation of carbon monoxide and hydrocarbons to carbon dioxide and water, and the reduction of nitrogen oxides to nitrogen gas.

$$2\,CO + O_2 \rightarrow 2\,CO_2$$

$$C_xH_y + O_2 \rightarrow CO_2 + H_2O$$

$$2\,NO \rightarrow O_2 + N_2$$

Next generation TWCs must include low amounts of expensive platinum group metals (PGM) while maintaining their high efficiency. Among other transition metals [6] [7] copper is considered a potential candidate to replace PGM in gasoline emission control technologies.

A recent study [8] at the Cu and K-edges demonstrated that Cu supported on CeO_2 possesses remarkable TWC properties with respect to the demanding NO reduction reaction. The NO reduction activity of CuO/CeO_2 increased significantly under oscillating feed condition relative to a static feed composition between 200 and 400 ºC that was attributed to the formation of oxygen vacancies and of reduced Cu species at the $CuO–CeO_2$ interface. Some other authors demonstrated the potential of Cu-decorated perovskite-type oxides [9]. The copper deposition forming $Cu/LaCoO_3$ enhances the low temperature activity if care is taken to obtain high dispersion of the Cu nanoparticles [10] [11]. Previous work [12] [9] showed that $CuO/La_{0.5}Sr_{0.5}CoO_3$ is the most active catalyst of the $La_{1-x}Sr_xCoO_3$ series. Unfortunately, the presence of cobalt decreases the industrial opportunities of this particular perovskite: in particular the high price due to low abundance [13] and safety problem for its environmental and human health dangerousness [14] [15] play a relevant role.

In this chapter, the catalytic performances are analyzed for a series of Iron-containing polycationic oxides. This particular transition metal was chosen as valid substitute of Co due to its abundance and remarkable catalytic performance in TWC application [16] [17]. Both composition and crystalline structure are expected to affect the catalytic activity and selectivity of oxides. The use of polycationic oxides allow to tune the reactivity and thus the chemical behavior whereas structure has effect on the ion mobility. Two main types of polycationic oxides are compared in this chapter: traditional perovskites and spinels. In both cases different compositions are considered to evaluate the role of cations on catalytic activity; moreover, both oxides have been considered as a support for copper decoration to investigate the role of support.

The conditions used to study the Fe-perovskite were chosen following the idea proposed in a previous publication [12] of the two research groups lead by Prof. Glisenti (UNIPD) and Dr.

Ferri (PSI). The fundamental principle, which is concise in the initial quote, is to use alternating redox pulses to "over" stimulate the catalyst and pump its activity toward TWC reactions. Eventually, the pulsing conditions were compared to static operations trying to understand if the alternating redox environment is needed to activate the surface of the catalyst.

4.2 Experimental

4.2.1 Synthesis

Perovskite-type mixed oxide of composition $LaFeO_3$ and spinel-type polycationic oxide $CuFeAlO_4$ were synthesized via the citrate-gel method [18] [19] described in chapter 2.1. Final calcination was conducted, for both systems, at 800°C for 6 h to obtain the desired crystal phase. To add the reducing functionalization, CuO was deposited to the perovskite-type oxide via wet impregnation. 10 wt% of final Cu were loaded forming $CuO/LaFeO_3$ and followed by a calcination at 450 ºC for 2 h. As benchmark, α-Al_2O_3 were loaded with Cu by wet impregnation (chapter 2.1) with an aqueous solution of $Cu(NO_3)_2{\cdot}6H_2O$ to produce 10 wt% Cu/Al_2O_3. The composite material was dried overnight and calcined at 450 ºC for 2 h. Prior to experiments all the samples were ground to a fine powder in an agate mortar and eventually sieved with fraction of 100-150 μm.

4.2.2 Catalytic activity tests

The activity of the powder catalysts toward TWC reaction was evaluated with a system considerably comparable with the one showed in the Chapter 2, Figure 2. The gas flow after reaction was analyzed with a InProcess Instruments GAM 400 mass spectrometer and with a FT-IR Brucker Alpha II equipped with a 7 cm gas cell with a ZnSe window. The gas cell is heated to 150 ºC during measurement. Spectra were recorded from 3000 to 300 cm^{-1} at a resolution of 4 cm^{-1} and scanner velocity of 0.33 Hz. The sample and background spectra resulted from averaging 30 and 20 scans, respectively. Fragments with m/z ratios of 2 (H_2), 4 (He), 18 (H_2O), 28 (N_2/CO), 30 (NO), 32 (O_2), and 44 (CO_2, N_2O) were followed. The exothermic effect of the reaction was minimized by diluting the catalyst (50 mg, 150–200 μm sieve fraction with cordierite 150 mg, 100–150 μm). Feed conditions were controlled by two solenoid on/off valves (Series 9, Parker; opening time <5 ms) placed in front of the reactor. The conditions followed the idea proposed in a previous publication [12]. Under rich conditions the feed composition was 0.7 vol% CO, 0.15 vol% NO, 0.16 vol% C_3H_8 balanced with He. When 0.7 vol% O_2 was added, the feed composition was only slightly lean. Experiments under constant feed were performed with 0.7 vol% CO, 0.15 vol% NO, 0.16 vol% C_3H_8, 1 vol% O_2, balanced with He. Rich or lean feed conditions were maintained for 20 s each. The long pulse time and the predominantly rich reaction conditions relative to realistic operation are suitable from an experimental viewpoint to study the catalytic and reducing response. The large difference in oxygen concentration, much larger than expected for operation in real, was selected to enhance the chemical response. Samples temperatures were monitored continuously using a K-type thermocouple inserted parallelly in the inlet of

the catalyst bed and controlled by a house made software. Before performing catalytic experiments, the samples were treated in 5 vol% O_2/He (50 sccm) at 400 ºC for 30 min.

4.3 Results and discussion

4.3.1 Cu/Al_2O_3

The first sample tested was the composite materials Cu/Al_2O_3. The chosen alumina was the α-Al_2O_3 to have a specific surface area of the same order of magnitude in the reference and In the samples. In fact, spinel and perovskite synthesized and described in this chapter do not exceed the ~15 m^2/g. Alumina is widely used as support for active catalyst [20] [5] thanks to its affordability and cheapness. Nonetheless, this support is manly used due to its intrinsic stability and to be inert in a wide range of temperatures and environments.

The load of copper deposited over alumina was chosen to be 10% in weight, as for the nanocomposite catalysts. This amount can be considered a good compromise in terms of chemical and physical stability of the metal nanoparticles and the overall surface occupancy.

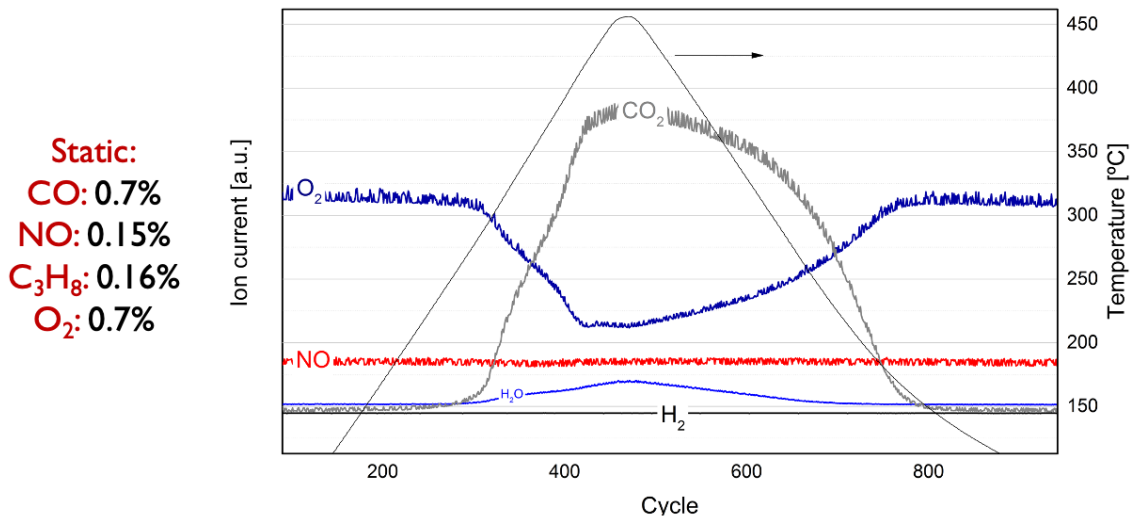

Figure 39 MS signal of 2 (H_2), 18 (H_2O); 30 (NO), 32 (O_2), and 44 (CO_2) gases during TWC static condition over Cu/Al_2O_3.

In Figure 39 the results of the evolution of all TWC gases over Cu/Al_2O_3 from 100 ºC to 450 ºC. The properties of this catalyst permit the abatement of only CO without converting the more challenging NO. The presence of water is an indicator of the reduction of CuO to metallic Cu. The behavior is the same even if the system is propelled with the switching valves (Figure 40). The gases concentration, as described in the Introduction, were chosen to have a λ between 0 and 0.9. NO is not catalyzed by the only presence of metallic Cu, nor by the possible Cu redox path that is created by the pulses ($Cu^{2+} \leftrightarrow Cu^{1+} \leftrightarrow Cu^{0}$). In fact, the idea to use pulses is to push the system to change surface chemistry and create active site for the reaction.

It is noteworthy that he tests over Cu/Al_2O_3 are fundamental to understand the need of an active support for TWC application. The metallic Cu by itself cannot behave as the active phase for the NO reduction: the interaction between copper particles, the capability of this cation to proceed into a redox path [11] and the interaction with the support are expected to play a major role

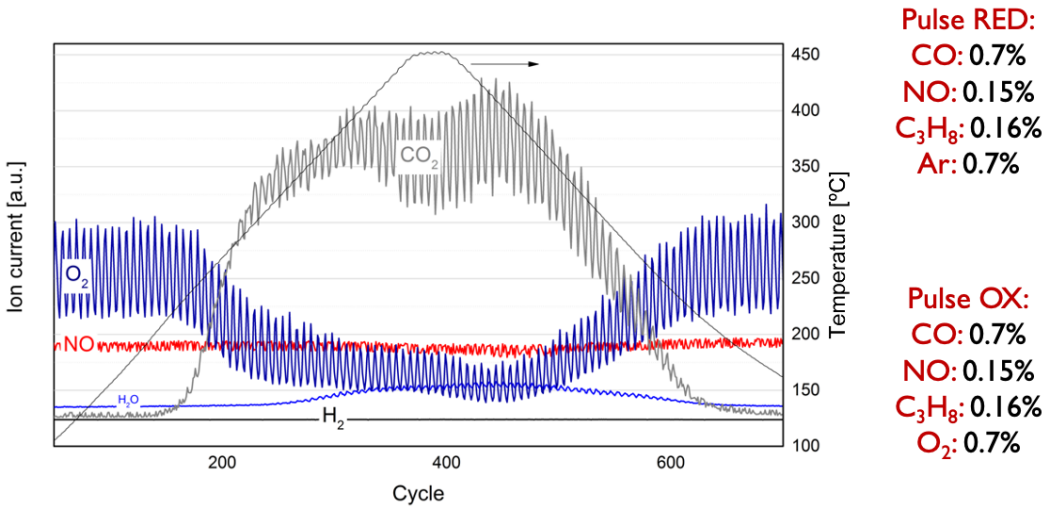

Figure 40 MS signal of 2 (H_2), 18 (H_2O); 30 (NO), 32 (O_2), and 44 (CO_2) gases during TWC pulsing condition over Cu/Al_2O_3.

4.3.2 $CuFeAlO_4$

In Chapter 3 of this thesis, it was Illustrated that the most stable spinel with the highest performance towards WGSR was the system $CuFeAlO_4$. The idea was to create an *in situ* catalyst starting from a simple but versatile system, as the spinel is. The already described results showed that the presence of aluminium inside the structure contribute in strengthens the spinel when is immersed in reactive environment, such as for the WGSR. Because of this reason, only the spinel system $CuFeAlO_4$ was tested as catalyst toward TWC reaction.

The first test conducted, analogous to Cu/Al_2O_3, was under static condition with the following gases concentration: 0.7 vol% CO, 0.15 vol% NO, 0.16 vol% C_3H_8, 1 vol% O_2. As expected, and not reported here, the system did not show any activity concerning NO reduction. As stated in Chapter 3.3.2, the Cu extraction from the lattice must be done in a reducing environment and the used feed in slightly oxidizing.

The second and third test were accomplished using the pulses trying to answer at the question that is at the foundations of this chapter: are pulses conditions useful to activate the catalyst in TWC application? The answer is, in this case: "*almost"*.

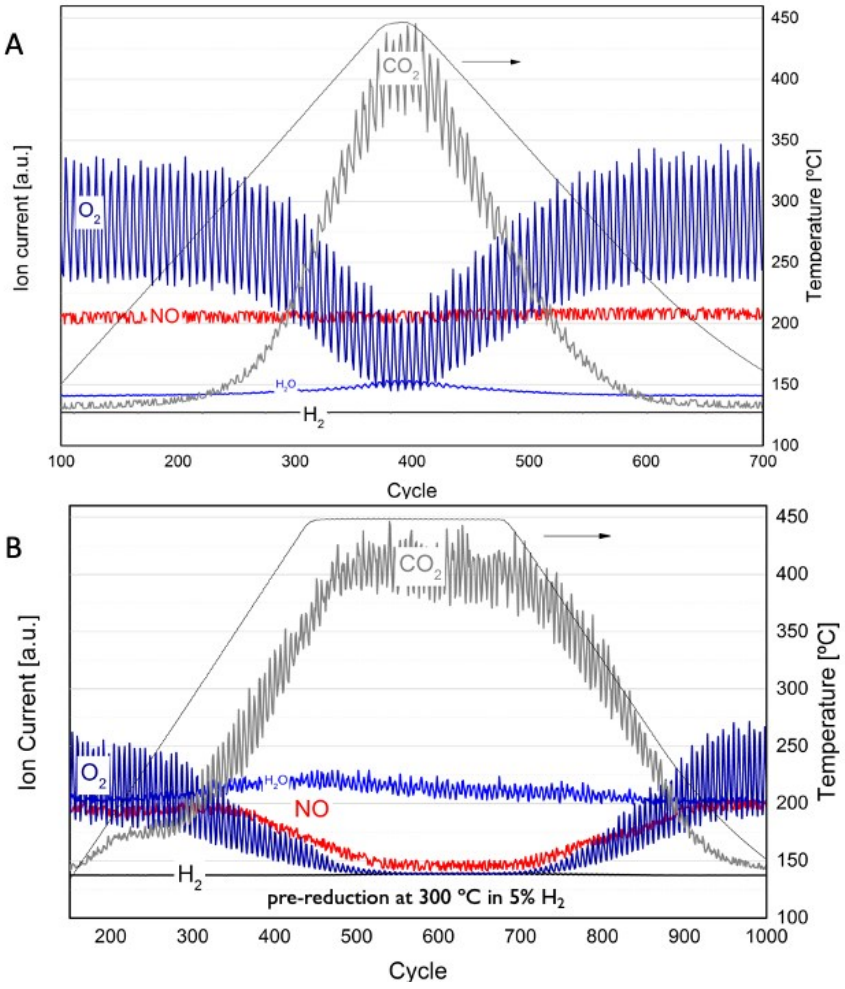

Figure 41 MS signal of 2 (H_2), 18 (H_2O); 30 (NO), 32 (O_2), and 44 (CO_2) gases during TWC pulsing condition over $CuFeAlO_4$. A) Test conducted without pre-reduction. B) Test conducted with pre-reduction at 300 ºC, 1h, 5% H_2.

In the previous Chapter it was demonstrated that if the spinel system is activated before reaction, it performs significantly better than without the activation as a consequence of the presence of Cu nanoparticles decorating the spinel surface. Figure 41 show the comparison between the performance of the system $CuFeAlO_4$ in the two different conditions, no-activated (A) and activated (B):

A. Reducing pulse:0.7 vol% CO, 0.15 vol% NO, 0.16 vol% C_3H_8.

   Oxidizing pulse: 0.7 vol% CO, 0.15 vol% NO, 0.16 vol% C_3H_8, 0.7 vol% O_2

In this test, the spinel was not pre-reduced. From water signal, (dark blue, A), is possible to understand that a slight reduction of the system is occurred but not enough to start the NO reduction. Oxygen is consumed to oxidize CO to CO_2 reaching the 80% of yield.

B. Reducing pulse:0.7 vol% CO, 0.15 vol% NO, 0.16 vol% C_3H_8.

   Oxidizing pulse: 0.7 vol% CO, 0.15 vol% NO, 0.16 vol% C_3H_8, 0.7 vol% O_2

   Thanks to the activation, that consisted in 5% H_2 up to 300 ºC dwell 1h, the simple and cheap $CuFeAlO_4$ can perform the abatement of NO. At 450 ºC the NO conversion reached the 35%, sign that a lot of work needs to be done but huge and immense perspectives are around the corner for this system!

4.3.3 Cu/$LaFeO_3$

Last studied system for TWC application is the composite materials Cu/$LaFeO_3$. Perovskite system are considered among the most promising materials for the substitution of noble metals as catalyst during TWC reaction and can be considered as an Interesting benchmark for fully understanding also the spinel based ones [21] [22]. The ability of perovkites to easily oxidize CO to CO_2 is known but it is not joined to a good performance in NO reduction. For fill this lacking competence, metal nanoparticles are deposited on the surface and as mentioned before, the synergy between metals and support may increase the conversion capability. To verify this hypothesis, both system $LaFeO_3$ and Cu/$LaFeO_3$ were tested during TWC activity. In any case, as first test the system Cu/$LaFeO_3$ was tested during static condition and the results is showed in Figure 42.

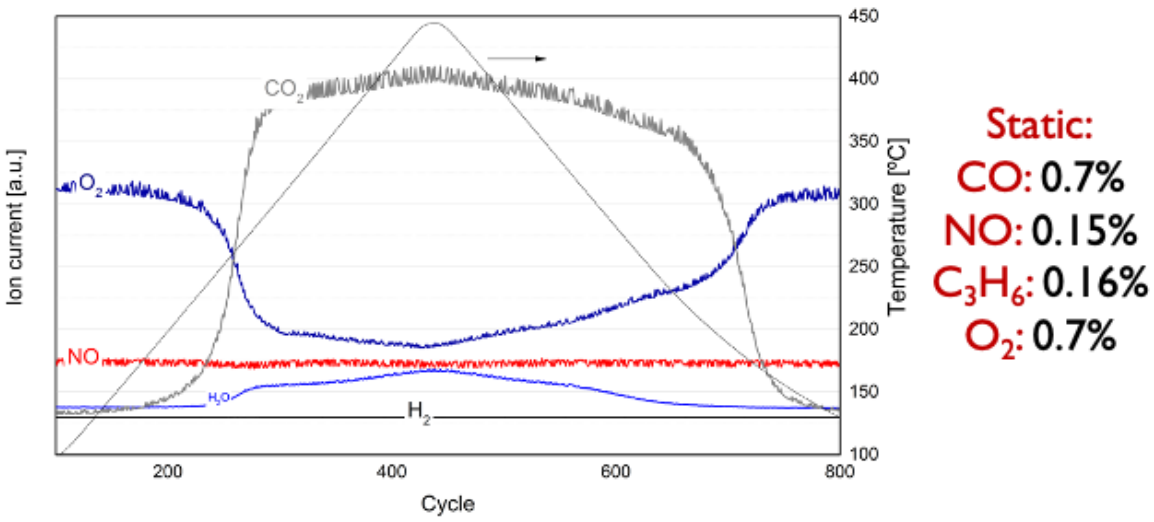

Figure 42 MS signal of 2 (H_2), 18 (H_2O); 30 (NO), 32 (O_2), and 44 (CO_2) gases during TWC static condition over Cu/$LaFeO_3$.

In the same way as all the other systems tested in this Chapter, Cu/$LaFeO_3$ during static condition did not show any attractiveness to the NO abatement. On the contrary and as expected, the oxidizing ability of the perovskite support is confirmed by the highly presence of CO_2 in the analyzed gases by the mass spectrometer. The presence of water, instead, could be assign to the reduction of the copper oxide to metallic copper and, probably, to the water gas shift reaction that may occurred in this kind of application.

Eventually, the system Cu/$LaFeO_3$ was tested in pulsing condition confirming the hypothesis that opened this chapter: are pulses conditions useful to activate the catalyst in TWC application? The answer is yes and with the performance increase of almost the 100%! In Figure 43 is possible to evaluate the ability of all the active systems toward NO abatement, studied in this thesis.

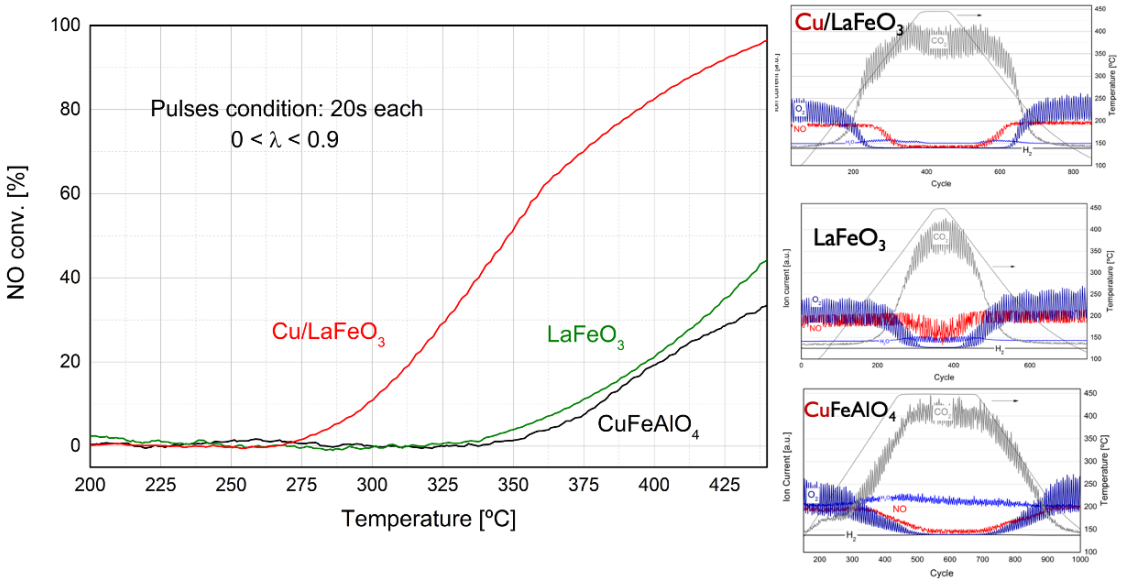

Figure 43 Left) NO conversion during pulsing reaction of $Cu/LaFeO_3$ - $LaFeO_3$ - $CuFeAlO_4$. The presence of Cu nanoparticles are fundamental to reach a reasonable TWC activity. Right) MS signal of 2 (H_2), 18 (H_2O); 30 (NO), 32 (O_2), and 44 (CO_2) gases during TWC pulsing condition.

The best performance was achieved by the composite materials $Cu/LaFeO_3$ reaching almost the 100% of NO conversion at 450 ºC. The 50% of NO conversion was reached at 350 ºC, decreasing of almost 100 ºC and having the same performance of the perovskite without copper. This result is the proof of two important statements:

1. First of all, pulses conditions are mandatory to activate the catalyst. Continuous and repeated environmental changing cause a modification of the catalyst surface that led to activate the perovskite and the copper nanoparticles.
2. Secondly, the interaction between Cu and perovskite during pulses is the key and their synergy may help the activation of the tough NO. A possible explanation, supported by *in situ* XRD and *operando* data from a previous communication [12], is the copper ability to change easily through its oxidation state $Cu^{2+} \leftrightarrow Cu^{1+} \leftrightarrow Cu^{0}$. Is

still not clear if is just the ability of fluctuation or, maybe, the presence of the unstable Cu^{1+}.

At the end, the NO was totally converted to N_2? Not totally, unfortunately. For answering this question, the pulsed reaction on $Cu/LaFeO_3$ was followed with a FT-IR, more sensible than MS to detect nitrogen compound as N_2O and NH_3.

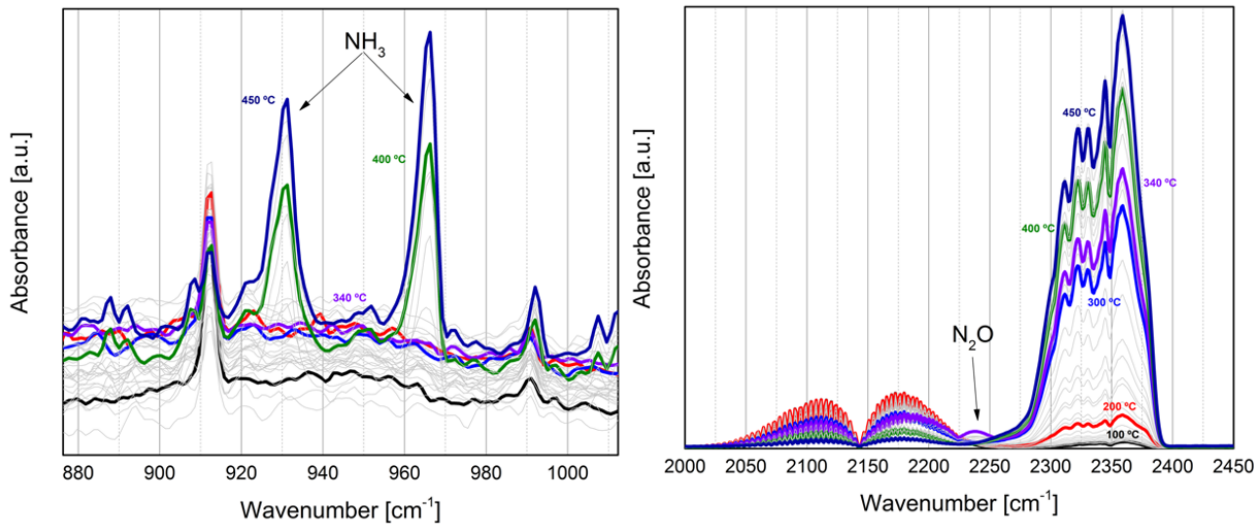

Figure 44 FT-IR signal of the exhaust gases during pulsed reaction on $Cu/LaFeO_3$. At high temperature, due to the relatively reducing environment, ammonia is formed from the NO abatement.

In Figure 44 are shown the most significant wavenumber regions (for FT-IR signal), capable of detecting the presence of N_2O and NH_3. The relevant result from this data is the formation of ammonia only at high temperature, while in the range of 300- 350 ºC the presence of N_2O is observed. A possible explanation for the NH_3 formation is the highly reducing environment that the system $Cu/LaFeO_3$ is immersed in. The oxygen pumped during the pulses was not enough for the NO reduction path [23] and, probably, instantly consumed by the perovskite for the CO oxidation or to restore its structure.

4.4 Conclusion

Different crystallographic structures containing Fe and Cu, inside or supported on the surface, were proposed as active catalyst towards Three Way Catalyst reaction. The foundation and the question that drove this research was the following: "*are pulses conditions useful to activate the catalyst in TWC application?*" The answer is yes, but some precaution must be taken in account. Spinel system $CuFeAlO_4$, for its nature and composition, showed a remarkable ability towards the NO abatements only during pulses condition. During static condition, only CO was oxidized to CO_2. Different behavior was point out from the perovskitic system $LaFeO_3$: in the scenario where only, the perovskite was used as catalyst, poor TWC performances were achieved, especially versus the NO. If the system is enriched with copper nanoparticles, thanks to its ability to change easily through $Cu^{2+} \leftrightarrow Cu^{1+} \leftrightarrow Cu^{0}$, TWC performance is boosted reaching almost the 100 % of NO conversion at 450 ºC. Unfortunately, FT-IR measurements showed the presence of ammonia in the exhaust gases, probably caused by the slightly reducing condition used ($0 < \lambda < 0.9$).

4.5 Bibliography

[1] H. S. Gandhi, G. W. Graham, and R. W. McCabe, "Automotive exhaust catalysis," *J. Catal.*, vol. 216, no. 1–2, pp. 433–442, 2003.

[2] U. G. Alkemade and B. Schumann, "Engines and exhaust after treatment systems for future automotive applications," *Solid State Ionics*, vol. 177, no. 26-32 SPEC. ISS., pp. 2291–2296, 2006.

[3] R. García-Contreras *et al.*, "Impact of regulated pollutant emissions of Euro 6d-Temp light-duty diesel vehicles under real driving conditions," *J. Clean. Prod.*, vol. 286, 2021.

[4] M. Giuliano *et al.*, "Characterization of the evolution of noble metal particles in a commercial three-way catalyst: Correlation between real and simulated ageing," *Catalysts*, vol. 11, no. 2, pp. 1–15, 2021.

[5] S. Rood, S. Eslava, A. Manigrasso, and C. Bannister, "Recent advances in gasoline three-way catalyst formulation: A review," *Proc. Inst. Mech. Eng. Part D J. Automob. Eng.*, vol. 234, no. 4, pp. 936–949, 2020.

[6] H. Hirata, "Recent Research Progress in Automotive Exhaust Gas Purification Catalyst," *Catal. Surv. from Asia*, vol. 18, no. 4, pp. 128–133, 2014.

[7] A. Beniya, Y. Ikuta, N. Isomura, H. Hirata, and Y. Watanabe, "Synergistic Promotion of NO-CO Reaction Cycle by Gold and Nickel Elucidated using a Well-Defined Model Bimetallic Catalyst Surface," *ACS Catal.*, vol. 7, no. 2, pp. 1369–1377, 2017.

[8] Y. Nagai, K. Dohmae, Y. F. Nishimura, H. Kato, H. Hirata, and N. Takahashi, "Operando XAFS study of catalytic NO reduction over Cu/CeO2: The effect of copper-ceria interaction under periodic operation," *Phys. Chem. Chem. Phys.*, vol. 15, no. 22, pp. 8461–8465, 2013.

[9] G. Carollo *et al.*, "CuO/Lao.5Sro.5CoO3 nanocomposites in TWC," *Appl. Catal. B Environ.*, vol. 255, no. January, 2019.

[10] M. Pacella *et al.*, "PGM-free CuO/LaCoO3 nanocomposites: New opportunities for TWC application," *Appl. Catal. B Environ.*, vol. 227, no. November 2017, pp. 446–458, 2018.

[11] G. Carollo, A. Garbujo, A. Bedon, D. Ferri, M. M. Natile, and A. Glisenti, "Cu/CGO cermet based electrodes for Symmetric and Reversible Solid Oxide Fuel Cells," *Int. J. Hydrogen Energy*, vol. 45, no. 25, pp. 13652–13658, 2020.

[12] I. Alxneit, A. Garbujo, G. Carollo, D. Ferri, and A. Glisenti, "CuO/Lao.5Sro.5CoO3: Precursor of efficient NO reduction catalyst studied by: Operando high energy X-ray diffraction under three-way catalytic conditions," *Phys. Chem. Chem. Phys.*, vol. 22, no. 34, pp. 18798–18805, 2020.

[13] N. Lin, Y. Gong, R. Wang, Y. Wang, and X. Zhang, "Critical review of perovskite-based materials in advanced oxidation system for wastewater treatment: Design, applications and mechanisms," *J. Hazard. Mater.*, vol. 424, no. PC, p. 127637, 2022.

[14] Q. Zhu *et al.*, "Cobalt exposure in relation to cardiovascular disease in the United States general population," *Environ. Sci. Pollut. Res.*, vol. 28, no. 31, pp. 41834–41842, 2021.

[15] L. Leyssens, B. Vinck, C. Van Der Straeten, F. Wuyts, and L. Maes, "Cobalt toxicity in humans—A review of the potential sources and systemic health effects," *Toxicology*, vol. 387, no. May, pp. 43–56, 2017.

[16] Y. Lu *et al.*, "Methane abatement under stoichiometric conditions on perovskite-supported palladium catalysts prepared by flame spray synthesis," *Appl. Catal. B Environ.*, vol. 144, pp. 631–643, 2014.

[17] A. Schön, J. P. Dacquin, P. Granger, and C. Dujardin, "Non stoichiometric La1-yFeO3 perovskite-based catalysts as alternative to commercial three-way-catalysts? – Impact of Cu and Rh doping," *Appl. Catal. B Environ.*, vol. 223, pp. 167–176, 2018.

[18] J. E. Tasca, C. E. Quincoces, A. Lavat, A. M. Alvarez, and M. G. González, "Preparation and characterization of CuFe2O4 bulk catalysts," *Ceram. Int.*, vol. 37, no. 3, pp. 803–812, 2011.

[19] C. Marcilly, P. Courty, and B. Delmon, "Preparation of highly dispersed mixed oxides and oxide solid solutions," *J. Am. Ceram. Soc.*, vol. 53, no. 1, p. 56, 1970.

[20] N. Guilhaume and M. Primet, "Catalytic combustion of methane: Copper oxide supported on high-specific-area spinels synthesized by a sol-gel process," *J. Chem. Soc. Faraday Trans.*, vol. 90, no. 11, pp. 1541–1545, 1994.

[21] S. Keav, S. K. Matam, D. Ferri, and A. Weidenkaff, "Structured perovskite-based catalysts and their application as Three-Way Catalytic converters-a review," *Catalysts*, vol. 4, no. 3, pp. 226–255, 2014.

[22] G. Perin *et al.*, "Cu@LaNiO3 based nanocomposites in TWC applications," *Appl. Catal. B Environ.*, vol. 209, pp. 214–227, 2017.

[23] L. Forni, C. Oliva, T. Barzetti, E. Selli, A. M. Ezerets, and A. V. Vishniakov, "FT-IR and EPR spectroscopic analysis of La(1-x)Ce(x)CoO3 perovskite-like catalysts for NO reduction by CO," *Appl. Catal. B Environ.*, vol. 13, no. 1, pp. 35–43, 1997.

Chapter 5

"If the first button of one's coat is wrongly buttoned, all the rest will be crooked."

Giordano Bruno

5.1 Introduction

To characterize the electrochemical performances of a Solid Oxide Cell (SOC), one of the most utilized techniques is the Electrochemical Impedance Spectroscopy (EIS). Through this method it is possible to obtain lot of useful information over the behavior of the electrodic material of the cell [1] [2]. However, the technique is influenced by the manufacturing process of the cell. The EIS is also sensitive towards the configuration of the device under analysis [3]. Therefore, it is crucial to pay particular attention to the building process of the experimental cell, minimizing possible systematic errors that could arise in the data originating from a defective sample.

Before analyzing the electrochemical behavior of the samples, it is necessary to understand how EIS works starting from some basic concepts.

The electrochemical resistance is the ability of a circuit to resist the flow of electrical current. It is defined by the Ohm's law as the ratio between a voltage E and a current I:

$$R \equiv \frac{E}{I}$$

The previous equation is limited to ideal resistors, defined by several simplifying properties that deviate from the real counterpart:

I. It follows Ohm's law regardless current and voltage levels.
II. It does not depend on the frequency.
III. Voltage and AC current signals are in phase with each other through a resistor.

Where these restraints are not verified it is possible to consider a more general circuit parameter. Here the impedance plays a crucial role because it can be defined the same way as the electrical resistance but no more limited by the restraints that limits the ideal resistors. The Electrochemical Impedance can be measured by applying an AC potential to a cell and then measuring the current passing through it. Generally, it is assumed that the potential excitation is sinusoidal, therefore the response is an AC current signal. The excitation signal is normally small; hence it is possible to consider the response of the cell as pseudo-linear, that allows to consider the current as a sinusoid at the same frequency of the sinusoidal potential but shifted in phase (following figure).

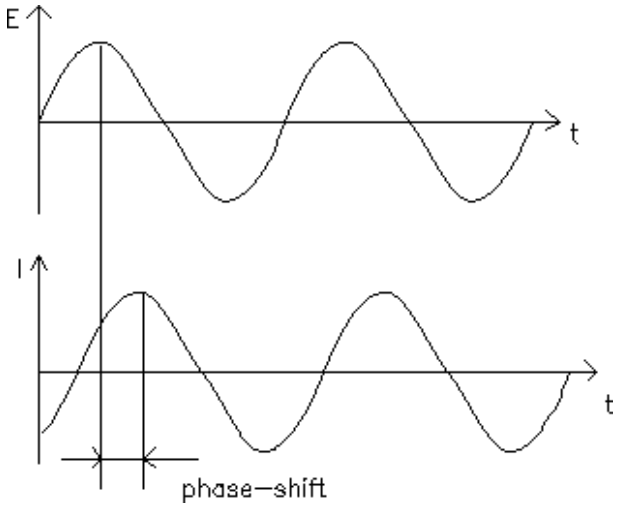

It is possible to express the excitation signal as a function of time:

$$E_t = E_0 \sin(\omega t)$$

E_t is the potential at the time t, E_0 the amplitude of the signal and the radial frequency ω [radians/s], which depends on the frequency [Hz]:

$$\omega = 2\pi f$$

In a linear system the response signal I_t can be expressed as:

$$I_t = I_0 \sin(\omega t + \phi)$$

Being I_0 it's amplitude and ϕ the shift in phase. The ratio of the excitation signal and the response signal, in analogy to the Ohm's law, allow to obtain the impedance Z of a system:

$$Z = \frac{E_t}{I_t} = \frac{E_0 \sin(\omega t)}{I_0 \sin(\omega t + \phi)} = Z_0 \frac{\sin(\omega t)}{\sin(\omega t + \phi)}$$

where Z_0 represents the magnitude and ϕ the phase shift.

Plotting the sinusoidal applied signal against the sinusoidal response signal it is possible to obtain what is commonly known as the 'Lissajous Figure' shown in the following figure which is an oval and its analysis on the oscilloscope screen has been the accepted method to calculate the impedance prior to modern EIS instrumentation.

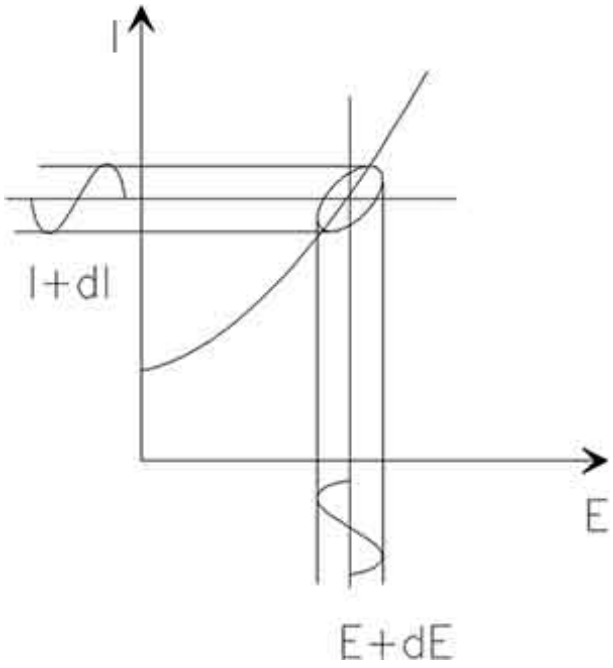

Taking into consideration the Euler's relationship:

$$\exp(j\phi) = \cos\phi + \sin\phi$$

It is possible to express the impedance as a complex function, whom potential and current response can be described as:

$$E_t = E_0 \exp(j\omega t)$$

$$I_t = I_0 \exp(j\omega t\text{-}\phi)$$

The impedance is then a complex number, given by:

$$Z(\omega) = Z_0 \exp(j\phi) = Z_0(\cos\phi + j\sin\phi)$$

Looking at the equation it is possible to see how the impedance is composed of a real and an imaginary part. Plotting the real part against the imaginary part it is possible to obtain what is known as a Nyquist Plot: each point of the plot represents the impedance at one specific frequency; in particular, data obtained at lower frequency are on the right while data obtained at high frequencies are on the left. The following figure shows the typical shape of a Nyquist plot.

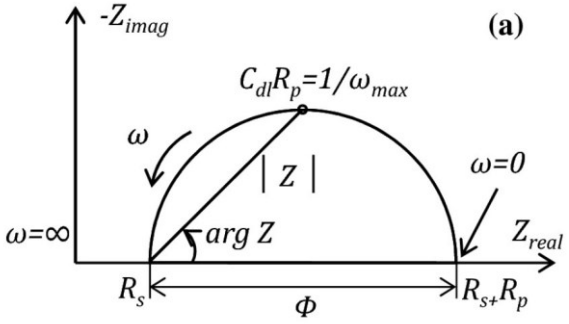

However, from this single plot the frequencies are not obvious and small impedances can be swamped by larger ones. Therefore, another plot, namely the Bode plot is commonly used as a data presentation method. Here the impedance is plotted with log frequency on the X-axis and both the absolute value of the impedance $|Z|= Z_0$ and the phase-shift on the Y-axis. This method allows to resolve the individual charge transfer processes with explicit frequencies; moreover, small impedances can be easily identified even in presence of large impedances (following image).

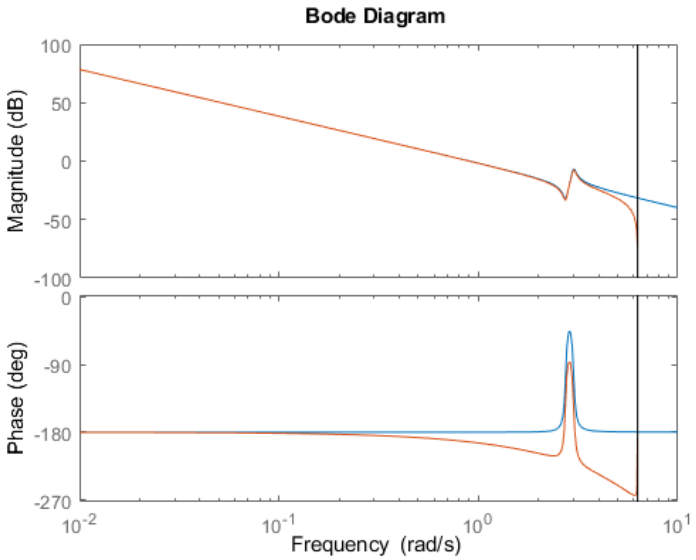

5.2 Experimental

EIS results have been obtained through PGSTAT 302 Autolab Frequency Response Analyzer: the tests have been carried out in steady state conditions, i.e., with no DC current in the frequency range of 10^{-2}-10^{6} Hz with a signal amplitude of 20 mV.

EIS has been used to investigate the electrochemical behavior of the fuel electrode in different operating conditions; in particular parameters such as temperature and fuel will be changed. The fuels that have been used are CO and H_2, which is necessary for the comparison with literature.

5.2.1 Modelling and calculations

All EIS data have been fitted and analyzed through the *ZView 4* software [4]. Data fitting allows to identify the different mechanisms and to quantify its resistances through the help of equivalent circuits. Different circuits have been utilized to fit different EIS data. The first step it has been to identify the number of processes looking both at the Nyquist and Bode

plots. Once identified the circuit has been made using a resistor (that simulates the ohmic resistance of the cell) connected in series with R-CPE subcircuits.

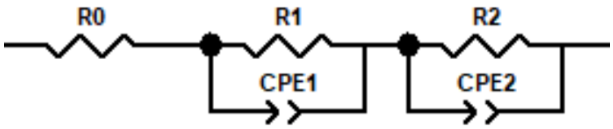

The number of R-CPE is the number of the processes seen in the plots. It has been decided to use the CPE (i.e., Constant Phase Element) instead of a normal capacitor since capacitors in EIS experiments often do not behave ideally.

By using the equivalent circuit, it is possible to fit each data set to obtain resistance values for each electrochemical process that occur during the EIS analysis. Hence, it is possible to calculate the total resistance of the processes. These values need to be refined as area specific resistance (ASR) to be compared with the data available in the literature [5] [6]:

$$\mathrm{ASR} = \mathrm{R}^{*}\frac{\mathrm{A}_{\mathrm{electrode}}}{2}$$

Where $\mathrm{A}_{\mathrm{electrode}}$ represents the area of the circular electrode calculated though the radius of the electrode (0.6 mm); the factor ½ depends by the fact that utilizing symmetrical cell the contribute to the resistances comes from both of electrodes, therefore dividing by two the ASR value refers to just one electrode (Chapter 2)..

Moreover, the fitting also allowed to calculate the capacitance for each process. Using R_{i} to indicate the resistance relative to the i-th process and using $\mathrm{CPET}_{\mathrm{i}}$ and $\mathrm{CPEP}_{\mathrm{i}}$ when referring to the Constant Phase Element (these are two fitting parameters), it is possible to calculate the capacitance for each process through:

$$C_i = (R_i + CPET_i)^{CPEP_i}$$

By knowing the capacitance value, it is possible to correlate the process to the phenomenon responsible for it, using data available in literature. A qualitative interpretation can be obtained by using Table 6.

Table 6 Capacitance values correlated to physical phenomena during SOC application.

Capacitance (F)	**Phenomenon Responsible**
10^{-12}	Bulk
10^{-11}	Minor, Second phase
10^{-11}-10^{-8}	Grain-boundary
10^{-10}-10^{-9}	Bulk ferroelectric
10^{-9}-10^{-7}	Surface layer
10^{-7}-10^{-5}	Sample-electrode interface
10^{-4}	Electrochemical reaction

One more data can be derived using the EIS: the activation energy associated with the overall fuel-electrode processes.

Starting from the conductivity (σ) equation as a function of the temperature, knowing that $ASR = 1/\sigma$, it is possible to obtain a linear equation:

$$\ln(ASR) = \frac{E_a}{k_B T} - \ln(k_0)$$

Using T as the temperature expressed in Kelvin, E_a as the activation energy and k_B as the Boltzmann constant. By plotting $\ln(ASR)$ as a function of 1000/T it is possible to obtain an Arrhenius Plot that gives the activation energy of the involved processes by using the slope of the fitting line as follows:

$$E_a = m*R*0.010341$$

Where R is the product of the Avogadro Number and the Boltzmann constant and the numeric factor is used to convert the obtained value in eV, which is the notation utilized in the literature.

5.2.2 Cell manufacturing

In the current thesis the button cell design was chosen due to its simplicity. Between the possible configurations, electrolyte-supported was realized to increment the reproducibility of the test. The main purpose of this work is, in fact, studying the property of the synthesized catalyst as fuel electrode in a solid oxide cell. To obtain the green pellet 2.5g of yttria stabilized zirconia (8-YSZ) [7] powder was compressed utilizing a pressure of 4.5 tons for 5 minutes; eventually the pellet was treated thermically at 1500°C for 6 hours with a ramp of 5°C/min until 1100° followed by a ramp of 3°C/min up to the final temperature. The manufactured electrolytes possessed dimensions of 20 mm diameter and 1 mm thickness. To prepare the ink, catalyst powder and 3% wt carbon soot was mixed in a mortar, followed by the addition of two α-terpineol based polymers. The ink was deposited via tape casting utilizing a 12 mm diameter mask. This method allowed to obtain electrode thicknesses of 30 µm [8]. Once the electrodes were deposited, a further heat treatment was carried out to

optimize the adhesion: 1100°C for 2h in air with a 3°C/min ramp. A gold paste made of a commercial compound of gold and an organic binder has then been deposited by tape casting on the electrodes as current collector.

5.3 Results and discussion

5.3.1 $CuFe_2O_4$/YSZ – H_2

In this and the following sections the behavior of $CuFe_2O_4$ and $CuFeAlO_4$ spinels system will be inspected and discussed when implied as fuel electrode in SOC application. In this paragraph, will be discussed the results obtained using a symmetrical cell with $CuFe_2O_4$ as the electrode material and YSZ adopted as the electrolyte material. Hydrogen has been used as the fuel, at a concentration of 10% wet in Ar with a flux of 100 sccm. Different temperatures have been taken into analysis: 600, 650, 700, 750 and 800 °C.

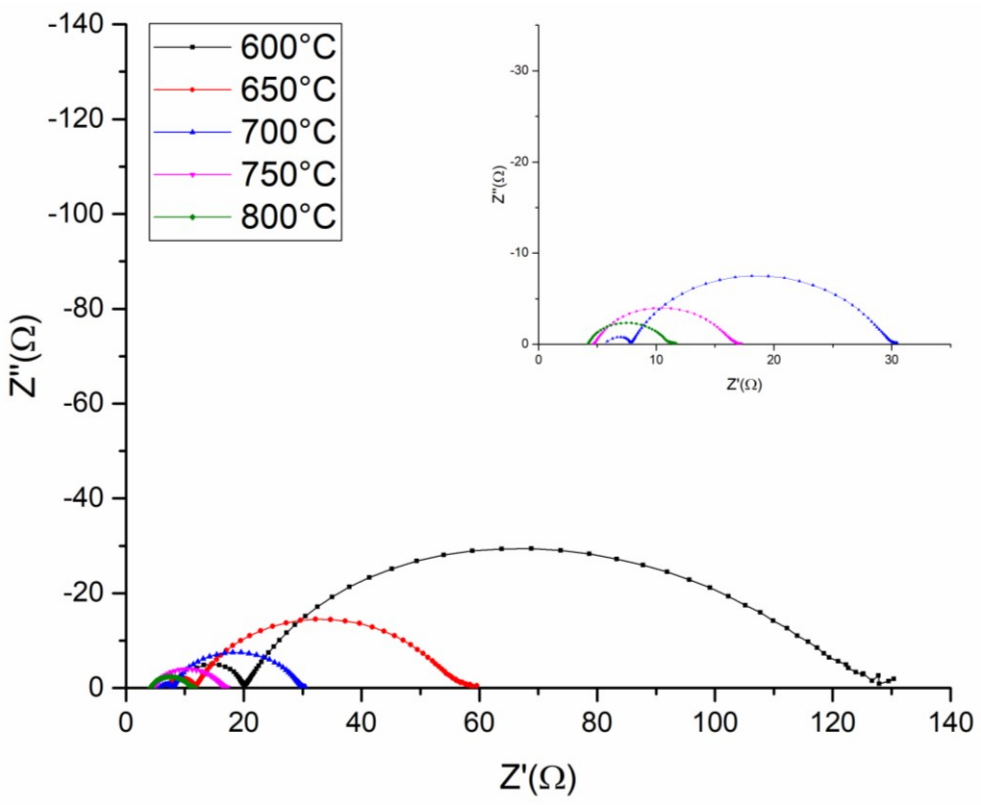

Figure 45: Nyquist plot obtained with $CuFe_2O_4$/YSZ/$CuFe_2O_4$, using as fuel 10%H2/Ar wet 100 sccm.

In Figure 45 are presented the impedance spectra obtained for $CuFe_2O_4$/YSZ/$CuFe_2O_4$. To analyze these spectra, made of two processes that are mostly distinguishable at lower temperatures, the model circuit that has been implied, consisted of a resistance in series with two R-CPE elements, as briefly discussed in the previous section. The intercept of the curve at high frequency with the X-axis gives the value of the Ohmic resistance, i.e., the resistance of the electrolyte. The intercept of the curve at low-frequency with the X-axis gives instead the total resistance, which includes the cell's Ohmic resistance, the concentration polarization resistance (due to mass-transfer or gas-diffusion) and the effective interfacial polarization resistance between the electrode and the electrolyte.

The total Area Specific Resistance (ASR) has been calculated for each temperature giving the following results. The ASR drastically reduces with the increment of temperature, suggesting the presence of one, or more, temperature dependent processes.

Temperature (°C)	600	650	700	750	800
ASR (Ωcm^2) 10% wet H_2/Ar	64.44	29.85	16.13	6.85	3.93

To confront the processes, a Bode plot was utilized as displayed in Figure 46. It is possible to observe that while the higher-frequency process is located at the same order of magnitude for all the temperatures analyzed, the one located at lower frequencies significantly change its value. This indicate that this process could be associated to a reaction influenced by kinetically activated parameters, hence temperature dependent, supporting the previous assumptions [9] [10].

It is then possible to associate the first process (lower frequencies) to a gas diffusion reaction, while the second process could be linked to an electrochemical reaction, more specifically a charge-transfer reaction or a resistance at the interface anode-electrolyte.

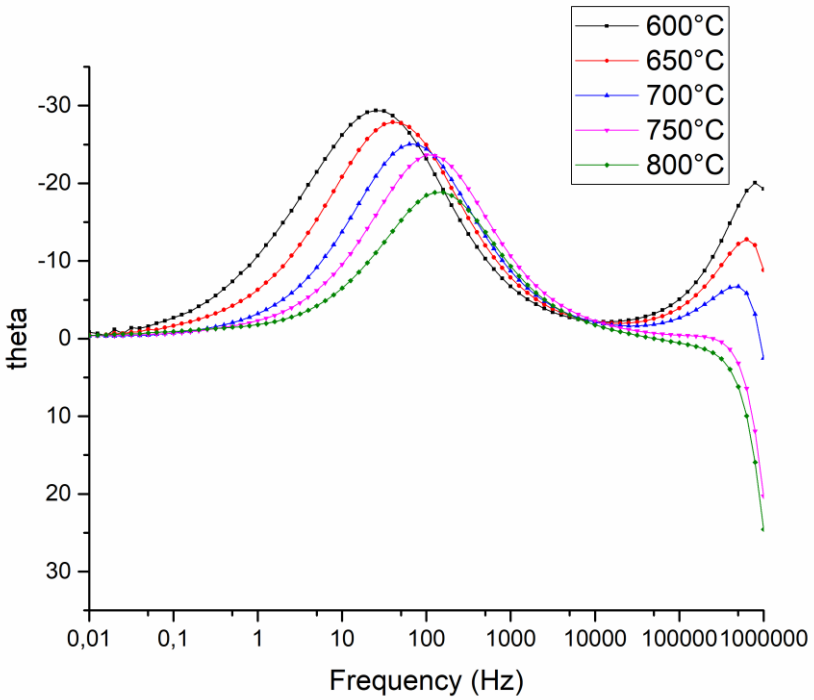

Figure 46: Bode plot obtained for $CuFe_2O_4$/YSZ/$CuFe_2O_4$, using as fuel 10% H_2/Ar wet 100 sccm.

An Arrhenius plot has been performed (Figure 47) and the activation energy for all the processes was of 1.14 eV. The obtained activation energy values are consistent with how reported in literature for solid oxide cells [11].

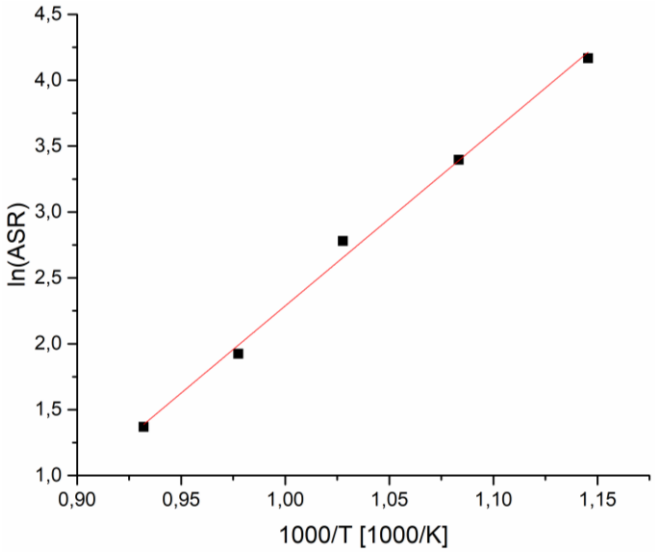

Figure 47: Arrhenius plot obtained for $CuFe_2O_4$/YSZ/$CuFe_2O_4$, using as fuel 10% H_2/Ar wet 100 sccm.

5.3.2 $CuFe_2O_4$/YSZ - H_2 + CO

In this paragraph, will be discussed the results obtained using a symmetrical cell with $CuFe_2O_4$ as the electrode material and YSZ as the electrolyte material.

Here, Hydrogen and carbon monoxide (CO) have been used as fuels, both at a concentration of 10% in Ar in a wet flux of 100 sccm.

The same temperatures of the previous paragraph have been considered: 600, 650, 700, 750 and 800 °C.

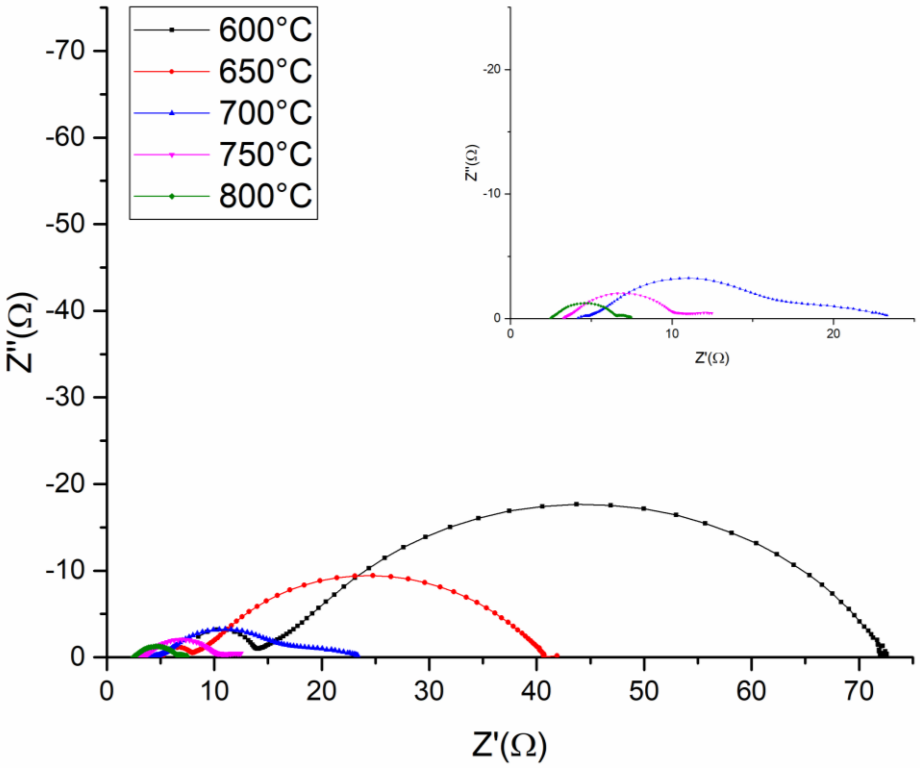

Figure 48: Nyquist plot obtained with $CuFe_2O_4$/YSZ/$CuFe_2O_4$, using as fuel a flow of 10% H2 10% CO/Ar wet 100 sccm.

In Figure 45Figure 48 are presented the impedance spectra obtained for $CuFe_2O_4$/YSZ/$CuFe_2O_4$. Following the procedure used in the previous paragraph, a model circuit made of a resistance in series with two R-CPE element was used, to fit and analyze the

impedance spectra. As a result, the total Area Specific Resistance (ASR) has been calculated for each temperature giving the following results.

Temperature (°C)	600	650	700	750	800
ASR (Ωcm^2) 10% H_2 10% CO wet/Ar	38.34	20.27	9.97	4.35	2.74

As previously seen for the system $CuFe_2O_4$ analyzed with the only hydrogen, also here the temperature plays a crucial role in the resistance of the material towards the electrochemical reactions that take place in the cell. Even in this case, in fact, the total ASR value strongly depends on the temperature, giving the best results at the highest temperature analyzed. The reason for this behavior could once again be given by the presence of thermally activated processes.

A Bode plot has been performed to fully characterize the sample and its processes (Figure 49). The results are similar to the ones already discussed for $CuFe_2O_4$ with only H_2:

- At higher frequencies there is the presence of an electrochemical reaction linked with a charge-transfer process [12]. It is also possible to observe that this reaction is temperature dependent due to its shift towards lower frequencies with rising temperatures [13],
- At lower frequencies there is the presence of a possibly gas diffusion reaction, strongly influenced by temperature. Looking at the Nyquist plot it is possible to observe that its ASR is almost negligible at temperatures higher that 700°C (as displayed in the zoomed part of the image).

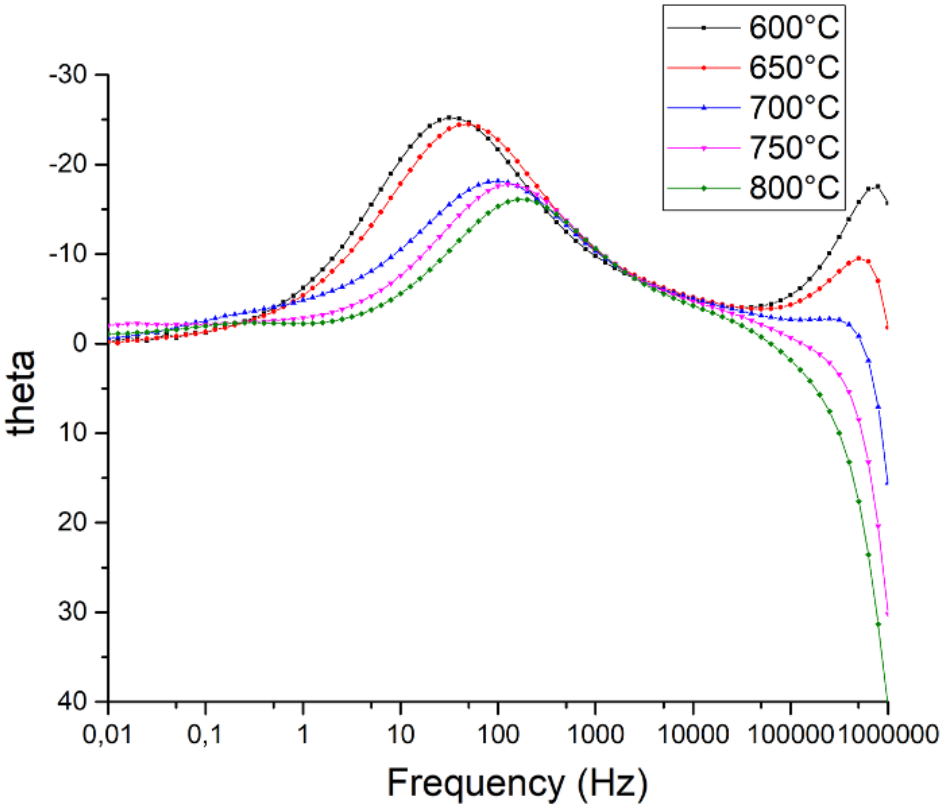

Figure 49: Bode plot obtained for $CuFe_2O_4$/YSZ/$CuFe_2O_4$, using as fuel a flow of 10% H_2 10% CO/Ar wet 100 sccm.

Lastly, the Arrhenius plot has been used to calculate the activation energy for all the processes giving a value of 1.10 eV.

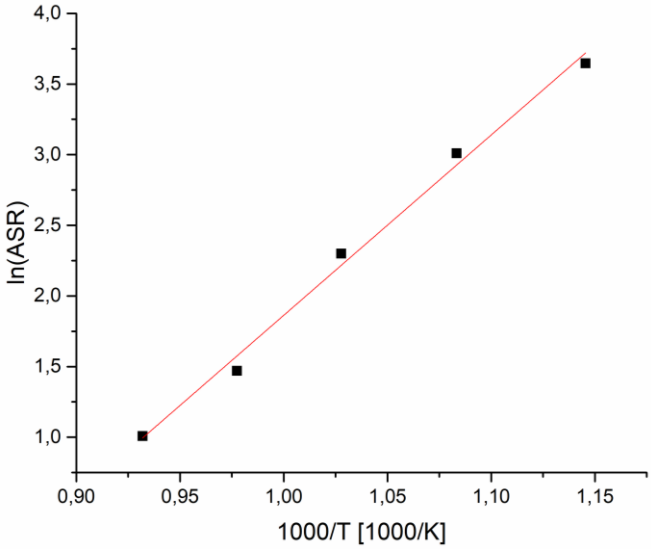

Figure 50: Arrhenius plot obtained for $CuFe_2O_4$/YSZ/$CuFe_2O_4$, using as fuel a flow of 10% H_2 10% CO/Ar wet 100 sccm.

5.3.3 $CuFeAlO_4$/YSZ – H_2

In this paragraph, will be discussed the results obtained using a symmetrical cell with $CuFeAlO_4$ as the electrode material and YSZ as the electrolyte material.

Hydrogen has been used as fuel at a concentration of 10% in Ar in a wet flux of 100 sccm.

The same temperatures of the previous paragraphs have been taken into analysis: 600, 650, 700, 750 and 800 °C.

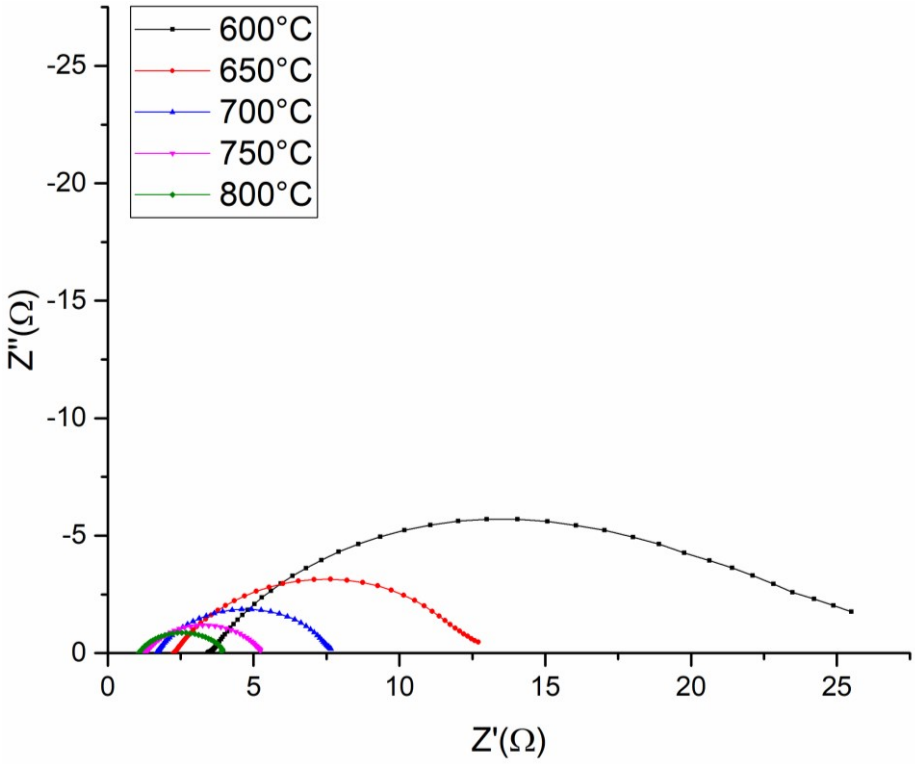

Figure 51: Nyquist plot of $CuFeAlO_4$/YSZ/$CuFeAlO_4$, using 10% H_2/Ar 100 sccm as fuel in a wet flow.

In Figure 51 are presented the Nyquist plots obtained at the different temperatures of analysis. Here the image can be a little misleading: even if at higher temperature seems like there is only one process, the plot at lower temperature shows that there actually are two processes, with a very small one located at high frequencies (for a better understanding of

the presence of this process it is possible to look at the Bode plot, Figure 52). Therefore, the model circuit was made of a resistance in series with two R-CPE elements, as seen before.
The total Area Specific Resistance (ASR) has been calculated for each temperature giving the following results.

Temperature (°C)	600	650	700	750	800
ASR (Ωcm^2) 10% H_2 wet/Ar	11.34	5.92	3.41	2.25	1.69

Even in this case there is the presence of thermally activated processes, giving the best overall performances at the highest temperature of 800°C.
Using a Bode plot it is possible to better identify the processes that take place in the cell.
The same considerations done in the previous two paragraphs can be applied here; there are, in fact, two processes:

- The first one, located at lower frequencies is noticeable at lower temperatures but almost negligible at 700°C and more (if the Nyquist plot is taken into account). It is therefore thermally activated, and it is possible to link it with a gas diffusion reaction.
- The second one, located at high frequencies, is possibly related to a charge-transfer process. Judging from the Nyquist plot, it is the more significant for the electrochemical performances of the material and it is temperature dependent.

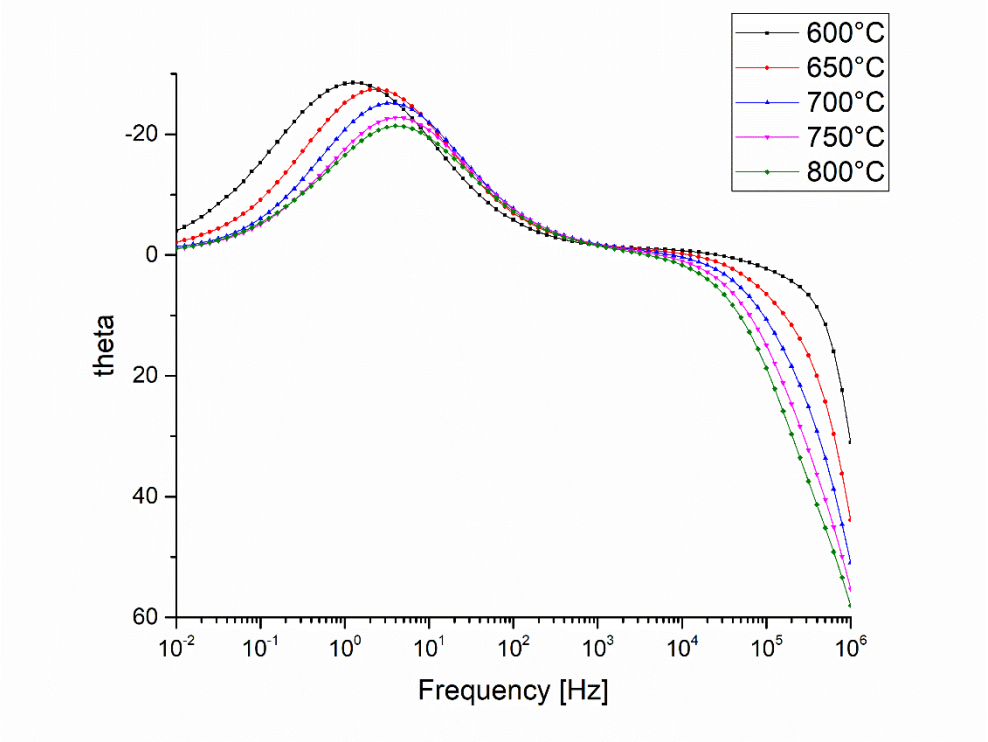

Figure 52: Bode plot of $CuFeAlO_4$/YSZ/$CuFeAlO_4$, using 10% H_2/Ar 100 sccm as fuel in a wet flow.

From the data obtained from the Nyquist and the Bode plots it is possible to suppose that, under 650°C, the limiting factor is linked with the diffusion of the reactant gases into the active sites of the electrode material, while, over that temperature, the bottle neck of the performances is given by the charge transfer reaction that takes place in the electrode.

To find the activation energy for all the processes we used the Arrhenius plot. The obtained value was of 0.77 eV.

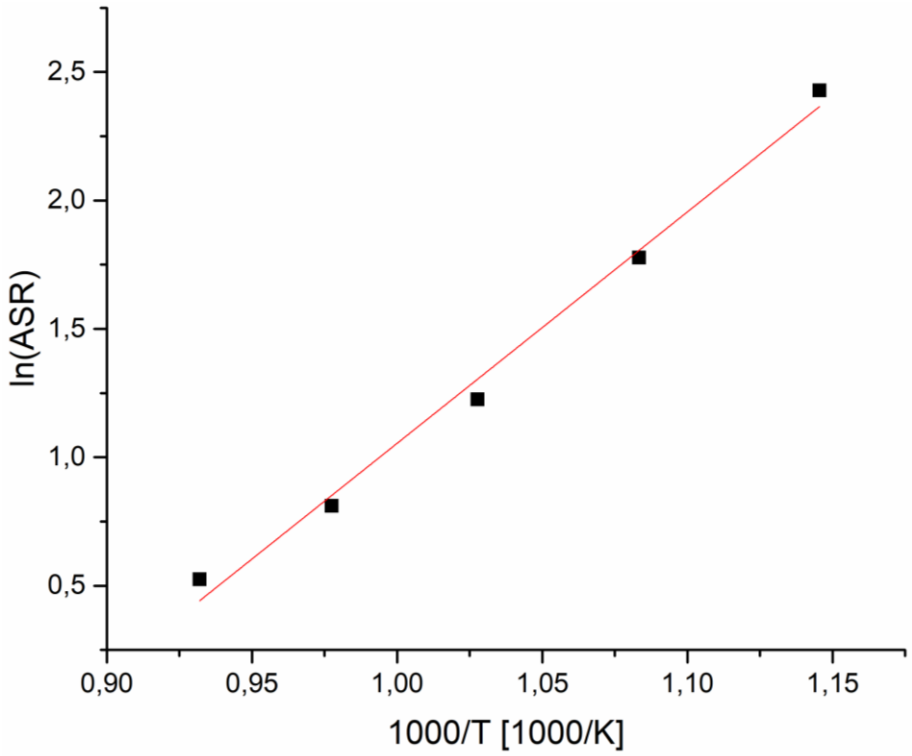

Figure 53: Arrhenius plot of $CuFeAlO_4$/YSZ/$CuFeAlO_4$, using 10% H_2/Ar 100 sccm as fuel in a wet flow.

5.3.4 $CuFeAlO_4$/YSZ – H_2 + CO

The results obtained using a symmetrical cell with $CuFeAlO_4$ as the electrode material and YSZ as the electrolyte material with Hydrogen and carbon monoxide (CO) as fuels (both at a concentration of 10% in Ar in a wet flux of 100 sccm) will be discussed in this paragraph. Different temperatures have been taken into account to compare the following results with the previous ones: 600, 650, 700, 750 and 800 °C.

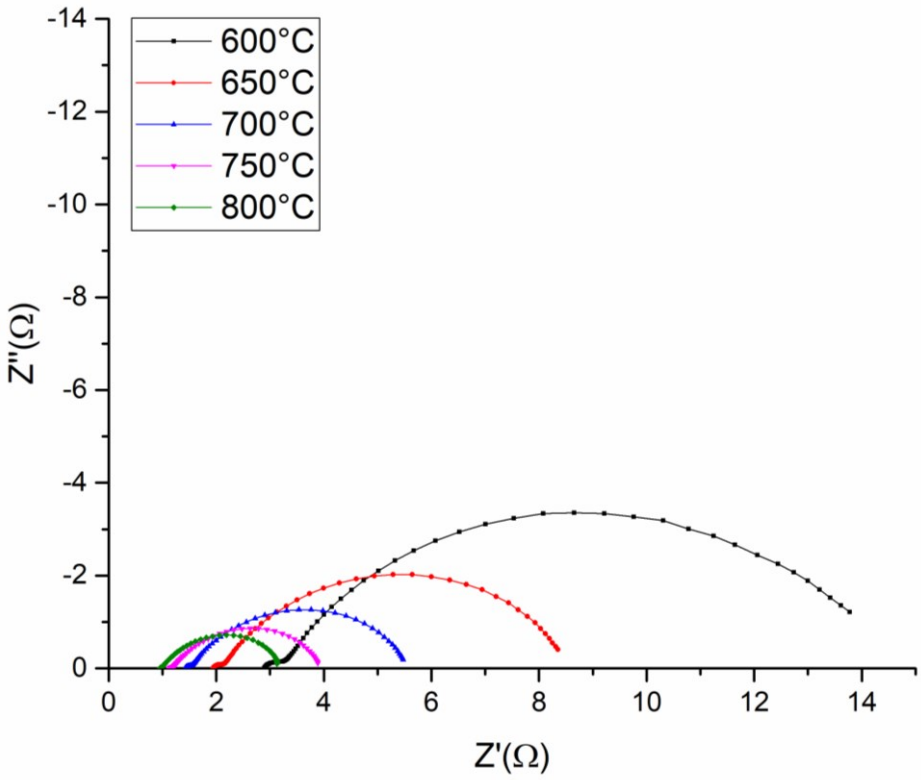

Figure 54: Nyquist plot of $CuFeAlO_4$/YSZ/$CuFeAlO_4$, using as fuel a flow of 10% H_2 10% CO/Ar wet 100 sccm.

As done for the other materials a symmetrical cell was built using $CuFeAlO_4$ at both the electrodes giving the following cell structure: $CuFeAlO_4$/YSZ/$CuFeAlO_4$. Then EIS analysis were performed leading to the Nyquist plots presented in Figure 54. To analyze them, a model circuit made of a resistance in series was made, with two R-CPE elements, as in all the previous cases. Nevertheless, in this instance, however, the two different processes are easily distinguishable: at lower frequencies (right side of the Nyquist plot) there is a big process that decreases its area with increasing temperatures while at higher frequencies there is a presence of a small process, possibly linked with charge-transfer reactions.

The total Area Specific Resistance (ASR) has been calculated for each temperature giving the following results.

Temperature (°C)	600	650	700	750	800
ASR (Ωcm^2) 10% H_2 10% CO wet/Ar	6.59	3.83	2.37	1.70	1.31

As seen previously there is the presence of thermally activated processes, giving better performances as the temperature rise. Looking at the Bode plot it is possible to identify those processes:

- At low frequency there is a process that grows in phase magnitude as the temperature rise, keeping constant its center. It can be linked with a gas diffusion reaction and, judging from the Nyquist plot, can be limiting factor to the performances of the cell,
- At higher frequencies there is the presence of a process possibly linked with a charge-transfer process or a resistance at the interface anode-electrolyte. Increasing the temperature its ASR value almost gets negligible. Therefore, despite being temperature dependent, in the range under analysis (600-800 °C) it is safe to assume that it does not hinder the performances of the cell, even at low temperatures.

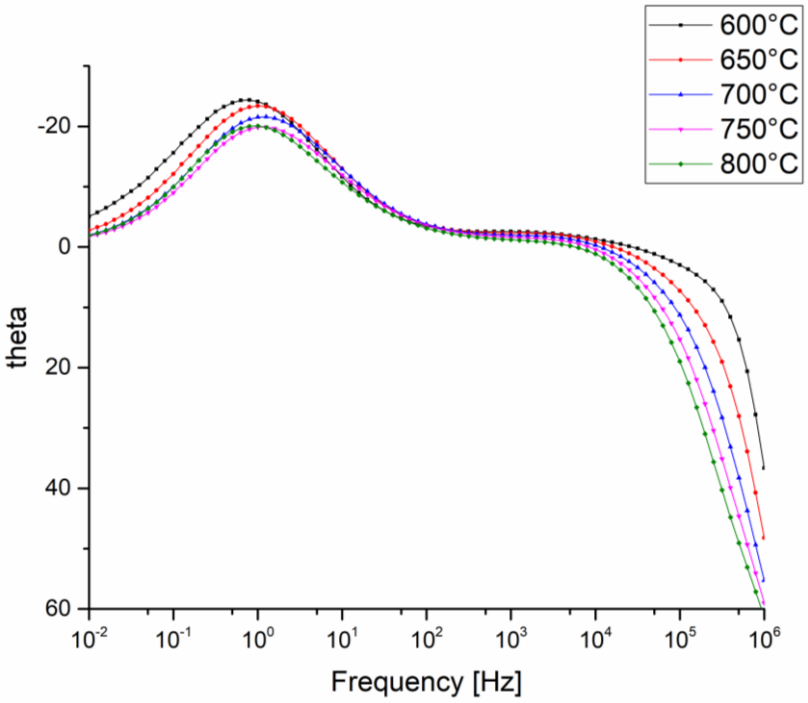

Figure 55: Bode plot of $CuFeAlO_4$/LSGM/$CuFeAlO_4$, using as fuel a flow of 10% H2 10% CO/Ar wet 100 sccm.

Lastly, the obtained value of the activation energy for all the processes, calculated through the Arrhenius plot was of 0.66 eV.

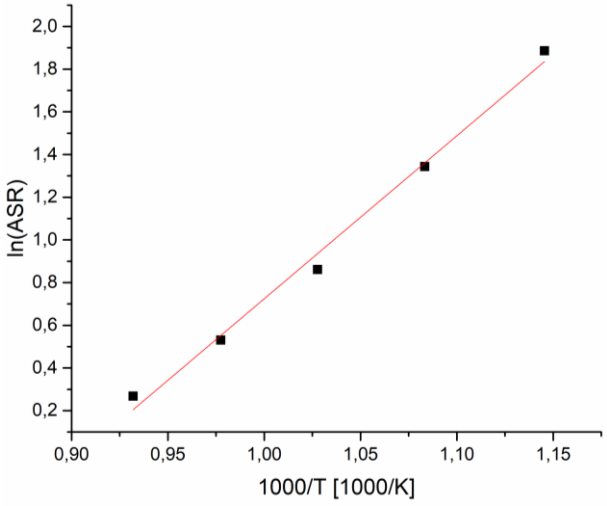

Figure 56: Arrhenius plot of $CuFeAlO_4$/YSZ/$CuFeAlO_4$, using as fuel a flow of 10% H_2 10% CO/Ar wet 100 sccm.

5.4 Conclusions

In this chapter, the electrochemical characterization of the two spinels system $CuFe_2O_4$ and $CuFeAlO_4$ were conduct. The system with only aluminum inside the lattice, $CuAl_2O_4$, was discard due to its very low reducibility, thus performance in the water gas shift reaction. The two spinels were studied by means of the Electrochemical Impedance Spectroscopy probing throughout temperature variation and different gases such hydrogen and carbon monoxide. In the previous Chapters 3 and 4, was evaluated the ability of the two system to reduce under hydrogen and the amount depends on the aluminum content. Further investigation of the catalysts with *in situ* XRD showed that $CuFeAlO_4$ spinel is the most balanced under reducing environment: enough to allow the Cu extraction without losing its structural integrity. Furthermore, XAS measurements of as-synthesized and activated spinel showed the presence of Cu^{1+} as amorphous phase, a good candidate as promoter for the CO_2 and CO activation during RWGS and other reactions as TWC. In all the presented cases, the activation process reveled the increasing of the performance due to the Cu extraction from the lattice. The key factor is the presence ($CuFeAlO_4$) or not ($CuFe_2O_4$) of aluminum and its quantity.

Table 7 Summary of the ASR values of $CuFe_2O_4$ and $CuFeAlO_4$ with H_2.

Temperature (°C)	600	650	700	750	800
$CuFe_2O_4$/YSZ/$CuFe_2O_4$ ASR (Ωcm^2) 10% wet H_2/Ar	64.44	29.85	16.13	6.85	3.93
$CuFeAlO_4$/YSZ/$CuFeAlO_4$ ASR (Ωcm^2)	11.34	5.92	3.41	2.25	1.69

10% H_2 wet/Ar	

The same results were obtained in the electrochemical investigation, where the $CuFeAlO_4$ spinel overcome the $CuFe_2O_4$ performance, in all temperature and with all the gases studied, Table 7 and Table 8.

Table 8 Summary of the ASR values of $CuFe_2O_4$ and $CuFeAlO_4$ with H_2 + CO.

Temperature (°C)	600	650	700	750	800
$CuFe_2O_4$/YSZ/$CuFe_2O_4$ ASR (Ωcm^2) 10% H_2 10% CO wet/Ar	38.34	20.27	9.97	4.35	2.74
$CuFeAlO_4$/YSZ/$CuFeAlO_4$ ASR (Ωcm^2) 10% H_2 10% CO wet/Ar	6.59	3.83	2.37	1.70	1.31

The ability of $CuFeAlO_4$ to maintain its structure beside the Cu extraction is the reason of its good activity, also toward the CO oxidation. In the previous section was showed how the Bode plot change with CO presence, confirmed by the appearing of a new process. In the spinel without aluminum ($CuFe_2O_4$) was not present this peculiarity because the system was not able to maintain the crystallographic structure intact at high temperature, thus its inability to activate and catalyze the CO oxidation. Another fact supporting this hypothesis is the activation energy of the cells studied in this thesis. In the cells containing the spinel with aluminum, the activation energies are lower compared to the spinel $CuFe_2O_4$. Moreover, the $CuFe_2O_4$ system present almost the same activation energy (Table 9) with and without the presence of CO, as another confirmation that the system did not have sufficient

stability to maintain the active site towards CO oxidation. On the contrary, the spinel with aluminum showed different activation energy and different ASR with H_2 and CO. In this case, the structural integrity allowed by the presence of Al inside the structure, permit the system to maintain the active site for the CO oxidation and, furthermore, increment the performance.

Table 9 Activation energies of the tested cells with different gases and electrodes composition.

Sample (fuel)	Activation energy (eV)
$CuFe_2O_4$/YSZ (H_2)	1.14
CuFe2O4/YSZ (H_2 + CO)	1.10
$CuFeAlO_4$/YSZ (H_2)	0.77
$CuFeAlO_4$/YSZ (H_2 + CO)	0.66

5.5 Bibliography

[1] Q. A. Huang, R. Hui, B. Wang, and J. Zhang, "A review of AC impedance modeling and validation in SOFC diagnosis," *Electrochim. Acta*, vol. 52, no. 28, pp. 8144–8164, 2007.

[2] M. J. Jørgensen, S. Primdahl, and M. Mogensen, "Characterization of composite SOFC cathodes using electrochemical impedance spectroscopy," *Electrochim. Acta*, vol. 44, no. 24, pp. 4195–4201, 1999.

[3] P. Jasinski, T. Suzuki, F. Dogan, and H. U. Anderson, "Impedance spectroscopy of single chamber SOFC," *Solid State Ionics*, vol. 175, no. 1–4, pp. 35–38, 2004.

[4] D. Vladikova, "THE TECHNIQUE OF THE DIFFERENTIAL IMPEDANCE ANALYSIS Part I: BASICS OF THE IMPEDANCE SPECTROSCOPY," *Proc. Int. Work. "Advanced Tech. Energy Sources Investig. Testing,"* no. January 2004, pp. 1–28, 2004.

[5] A. V. Virkar, J. Chen, C. W. Tanner, and J. W. Kim, "Role of electrode microstructure on activation and concentration polarizations in solid oxide fuel cells," *Solid State Ionics*, vol. 131, no. 1, pp. 189–198, 2000.

[6] V. Dusastre and J. A. Kilner, "Optimisation of composite cathodes for intermediate temperature SOFC applications," *Solid State Ionics*, vol. 126, no. 1, pp. 163–174, 1999.

[7] J. B. Goodenough, "Oxide-ion conductors by design," *Nature*, vol. 404, no. 6780, pp. 821–823, 2000.

[8] G. Carollo, A. Garbujo, A. Bedon, D. Ferri, M. M. Natile, and A. Glisenti, "Cu/CGO cermet based electrodes for Symmetric and Reversible Solid Oxide Fuel Cells," *Int. J. Hydrogen Energy*, vol. 45, no. 25, pp. 13652–13658, 2020.

[9] Y. Liu *et al.*, "Natural CuFe2O4 mineral for solid oxide fuel cells," *Int. J. Hydrogen Energy*, vol. 42, no. 27, pp. 17514–17521, 2017.

[10] K. T. Wu and T. Ishihara, "Spinel-based oxide cathode used for high temperature CO2/H2O co-electrolysis," *Solid State Ionics*, vol. 329, no. October 2018, pp. 46–51, 2019.

[11] S. Paydar, N. Akbar, Q. Shi, and Y. Wu, "Developing cuprospinel CuFe2O4–ZnO semiconductor heterostructure as a proton conducting electrolyte for advanced fuel cells," *Int. J. Hydrogen Energy*, vol. 46, no. 15, pp. 9927–9937, 2021.

[12] Y. Pan, S. Geng, G. Chen, and F. Wang, "CuFe2O4/CuO coating for solid oxide fuel cell steel interconnects," *Int. J. Hydrogen Energy*, vol. 46, no. 44, pp. 22942–22955, 2021.

[13] B. A. Boukamp, M. Verbraeken, D. H. A. Blank, and P. Holtappels, "SOFC-anodes, proof for a finite-length type Gerischer impedance?," *Solid State Ionics*, vol. 177, no. 26-32 SPEC. ISS., pp. 2539–2541, 2006.

Chapter 6

"Come, come, whoever you are.
Wanderer, worshipper, lover of leaving — it doesn't matter,
Ours is not a caravan of despair.
Come, even if you have broken your vow a hundred times,
Come, come again, come."
Rumi

6.1 Introduction

Co-based perovskite-type oxides are used in various fields as catalysts, electrodes in solid oxide fuel cells and in gas separation (ceramic membranes). The aim of this experiment is to perform in situ, time-resolved high energy X-ray diffraction analysis on the reversible structural changes of Co-based perovskite-type oxides under oxidative (O_2) and reductive (H_2 and/or CO) environments as a function of doping with different elements.

Detailed information collected using XRD under pulsing conditions at selected temperatures will allow correlating the nature of the structural changes (reversible on these materials) with catalytic activity, ion mobility and electro-catalytic activity. The systems proposed for these experiments are $LaCoO_3$-based oxides obtained by doping with increasing amounts of Sr (A-site) and Fe (B-site).

Perovskite-type oxides are relevant to a number of important industrial processes and the large interest on these compounds is related to the tunability of their proprieties [1]. The combination of element composition and proper doping allow the development of and the control over the desired functionality. Several elements can be inserted in the perovskite-type structure with the aim to develop specific behaviors. La- Sr-Co-Fe-O oxides are used in intermediate temperature solid oxide fuel cells as electrodes replacing the conventional $(LaSr)MnO_3$ used at higher temperature. Moreover, La-Co-O perovskite-type systems are used in gas separation and as oxygen pump [2]. All these applications are allowed by the developed mixed ion-electron conductivity and induced formation of surface-active sites. The incorporation of aliovalent cations in the perovskite lattice is an effective way to generate vacancies and thus to increase ion mobility and catalytic activity. Vacancies are responsible for the coordination and activation of reactants, e.g. NO.

Previous operando X-ray diffraction measurements performed on $LaCo_{0.5}Cu_{0.5}O_3$ (vs un-doped $LaCoO_3$) [3] [4] analogous to modulation experiments (H_2/O_2, CO/O_2) [5] have shown that Cu doping enhances the extent of phase change in addition to bestowing catalytic activity towards three-way catalysis (TWC) type reactions. It was observed that the activity is strictly linked to the phase change and to the reducibility of the material. To this end, Cu was observed to decrease the reduction temperature of the material. Prompted by preliminary H_2/O_2 and CO/O_2 pulse measurements on un-doped and doped $LaCoO_3$ using HE-XRD (Figure 57), $CuO@La_{0.5}Sr_{0.5}CoO_3$ nano-composites was designed and tested under TWC pulsed conditions with the purpose of studying (by means of XRD) the extent of structural changes and consistently, the catalytic activity determined simultaneously with mass spectrometry [6].

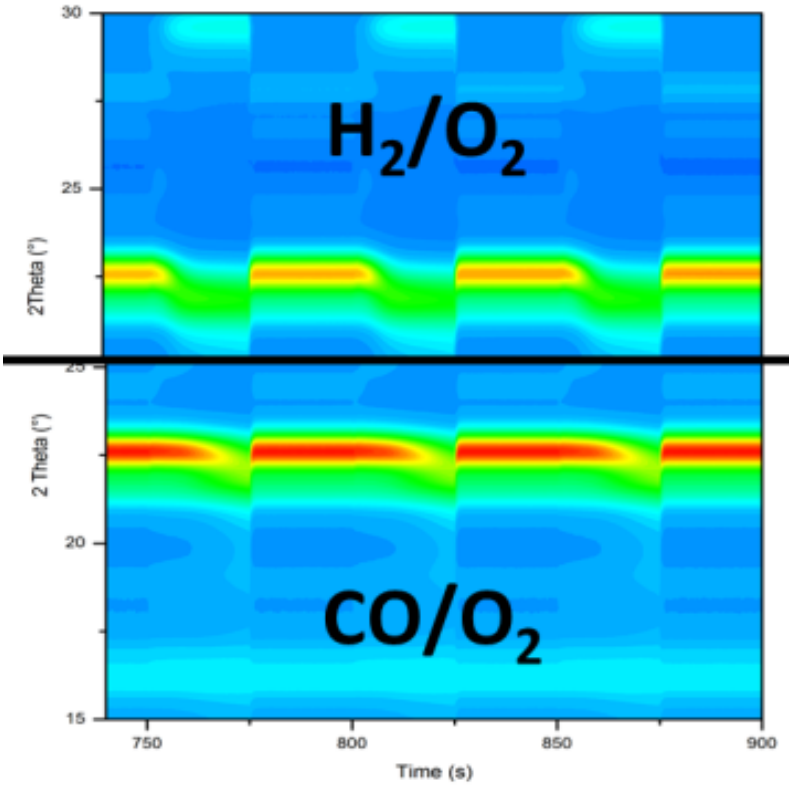

Figure 57 Time-resolved HE-XRD data (0.5s/pattern) during H_2/O_2 and CO/O_2 pulses on $LaCo_{0.5}Cu_{0.5}O_3$ at 450°C. Structural changes from perovskite to brownmillerite are visible.

The collected data show intriguing results probably induced by the presence of Cu surface sites catalytically active towards NO, and of enhanced vacancies and ion mobility of supporting $La_{0.5}Sr_{0.5}CoO_3$ [7]. In order to study the fast dynamics of the process, the patterns were acquired with high acquisition rate and thus high time-resolution with the aim of following the process at subsecond time scale. A careful study of the material response to different environments (different pulse sequences) is essential in order to understand the behavior of the material and to design a new generation of materials in which functionality can be tailored.

6.2 Experimental

6.2.1 Synthesis

Perovskite-type mixed oxide of composition $LaCoO_3$ – $La_{0.8}Sr_{0.2}CoO_3$ – $La_{0.5}Sr_{0.5}CoO_3$ – $LaFe_{0.5}Co_{0.5}O_3$ were synthesized via the citrate-gel method [8] [9] described in chapter 2.1. Final calcination was conducted, for all systems, at 800°C for 6 h to obtain the desired crystal phase.

6.2.2 High energy X-ray diffraction tests

Operando time-resolved X-ray diffraction patterns were acquired at beamline ID15A of the ESRF (Grenoble, France, beam size 100 x 100 μm) using a Pilatus X detector (1679 x 1475 pixels, Dectris) at a time resolution of 0.5 s and at an incident energy of 79.5 keV. The samples (sieve fraction, 100–150 μm) were firmly mounted between two quartz wool plugs in a quartz

capillary reactor (OD = 2 mm, wall thickness 50 µm) which allowed the insertion of a 0.5 mm thermocouple. The sample was positioned 800 mm from the detector. The reactor was connected to a gas manifold allowing for fast switching of the feed to simulate reductive and oxidative operation and was interfaced by heated stainless steel capillary to a mass spectrometer (MS, Pfeiffer Omnistar GSD 320) for on-line gas analysis. The following m/z values were recorded: 2 (H_2), 4 (He), 18 (water), 28 (CO), 32 (O_2) and 44 (CO_2). Feed conditions were controlled by two solenoid on/off valves placed in front of the quartz reactor and slaved to the beamline control software to synchronize data acquisition and gas switches. Heating was provided using a hot air blower.

An experiment consisted in heating the sample to the desired temperature (300, 400 and 500 °C) in 5 vol% O_2/He followed by repeated and alternate pulses of 5 vol% CO/He, 1 vol% Ar and 5 vol% O_2/He (30 s each).

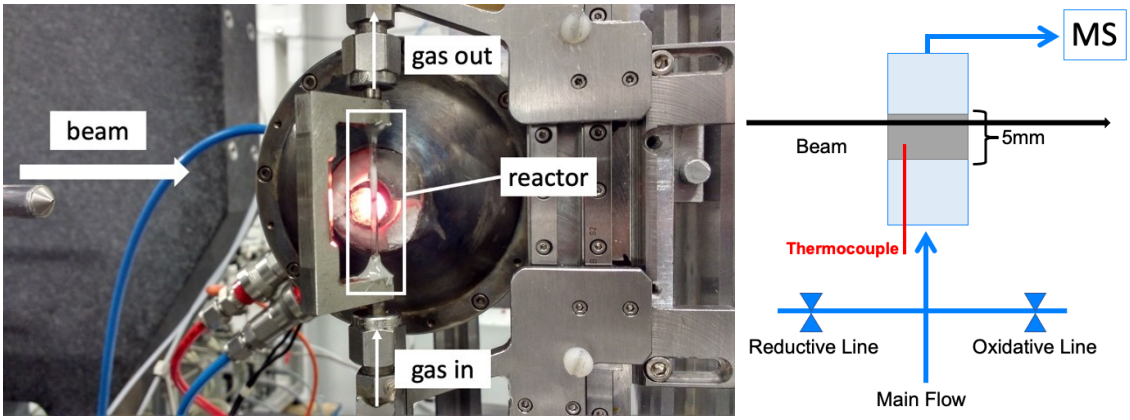

Figure 58 Left: image of the setup used at the beamline ID15A.

Right: scheme of the system used during operando measurements.

Above 300°C, the measurements at selected temperatures were interspersed by heating to 600°C in 5 vol% O_2/He in order to ensure restauration of the original structure, which was confirmed by XRD.

6.3 Results and discussion

As mentioned in the Experimental part, a typical experiment consisted in repeated and alternated pulses of 5 vol% CO/He and 5 vol% O_2/He for 30 s each. The catalytic system was followed, from the crystallographic point of view, collecting a XRD pattern every 0.5s.

In Figure 59 the graphic representation of the experiments can be appreciated. The Y axis indicates the total number of XRD patterns taken during the experiment, while the X axis define the Wave Vector (Q) from the reciprocal lattice. The color code represents the intensity of the perovskitics peaks where blue is almost zero counts and red the highest number counted from the detector. In other words, the image consists in hundreds of ordinary XRD patterns looked from the top view. A line in this 2D colorful graph is the peak in the *more friendly* XRD pattern.

In the following paragraphs all the synthesized perovskites will be evaluated during the changing of a pulse, from reducing to oxidizing environments. CO_2 production during the reducing pulses will be used to calculate the Oxygen Storage Capacity (OSC) from the systems doped with strontium, as the more reactive in the CO oxidation.

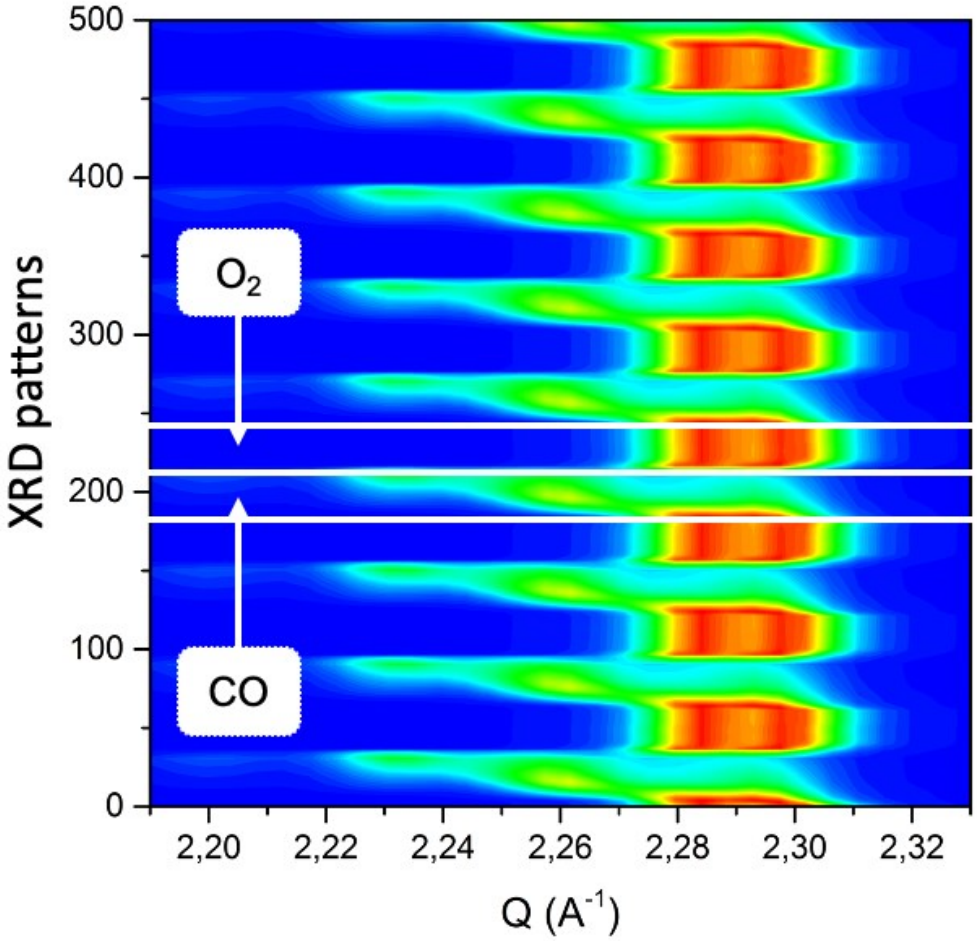

Figure 59 *$LaCoO_3$ un-doped, pulses of CO (5%) and O_2 (5%), pulses 30s each, T = 500 ºC.*

6.3.1 B-doped $LaCoO_3$

The first sample that will be analyzed is the perovskite doped in the B-site: $LaCo_{0.5}Fe_{0.5}O_3$. The B-doping in the perovskite structure allows to confer a peculiar characteristic during the design of the catalyst. Iron is widely used as dopant for cobalt perovskite [10] [1] [2] or, as stated in Chapter 4, as the main perovskitic cation. The most used perovskite used for O_2-

elctrode in Solid Oxide Cell is the $La_{1-x}Sr_xCo_{1-y}Fe_yO_3$ where the iron content may vary from 0.5 to 0.8 [11] [12].

In complete opposition from the results discussed in Chapter 4 and compared to the un-doped B-site perovskites, the ability of $LaCo_{0.5}Fe_{0.5}O_3$ to oxidized CO is very low.

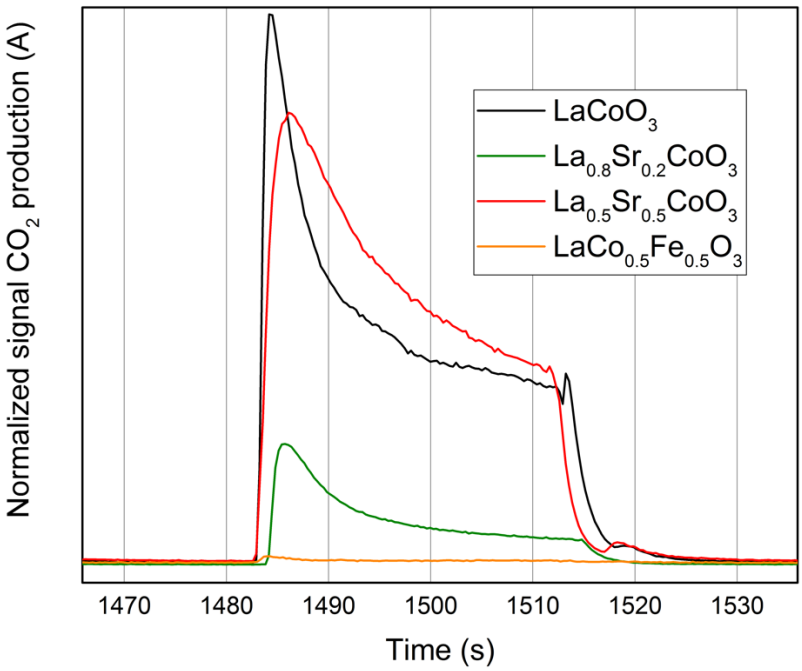

Figure 60 CO_2 production during the last reducing pulse at 300 ºC. The perovskite containing Fe has the lowest ability to convert CO compared to the B-un-doped perovskites.

The CO_2 production during CO oxidation can be evaluated in Figure 60. The graph is related to the last reducing pulse to be completely sure that the system reached a dynamic equilibrium. This behavior may be explained from two different point of view.

The first explanation, independently on the temperature, is the inability of Fe-doped perovskite to create surface vacancies as a consequence of the highly affinity of iron to strongly bon oxygen [13] [14]. So, in this case, a long pulse of only CO may not be sufficient to activate the surface, as demonstrated in Chapter 4.

The second possible explanation derive from the XRD data showed in Figure 61. This sequence from 300 ºC to 500 ºC show the main perovskitic peak of the B-doped $LaCoO_3$ with iron. The difference from Figure 59 is the representation of only two pulses: from bottom, the reducing one and from the perfect half, the oxidizing pulse. Probably it is difficult to understand where the oxidizing pulse starts and the reason is the following: the system $LaCo_{0.5}Fe_{0.5}O_3$ did not change from the structural point of view. In particular, the doublet peak proved the presence of a rhombohedral structure [15]. From the *in situ* XRD data is clear that, during the CO oxidation reaction, no visible structural changes occurred. No other structural recombination was seen as possible precursor towards the CO evolution in CO_2, as hypothesized in the Introduction section.

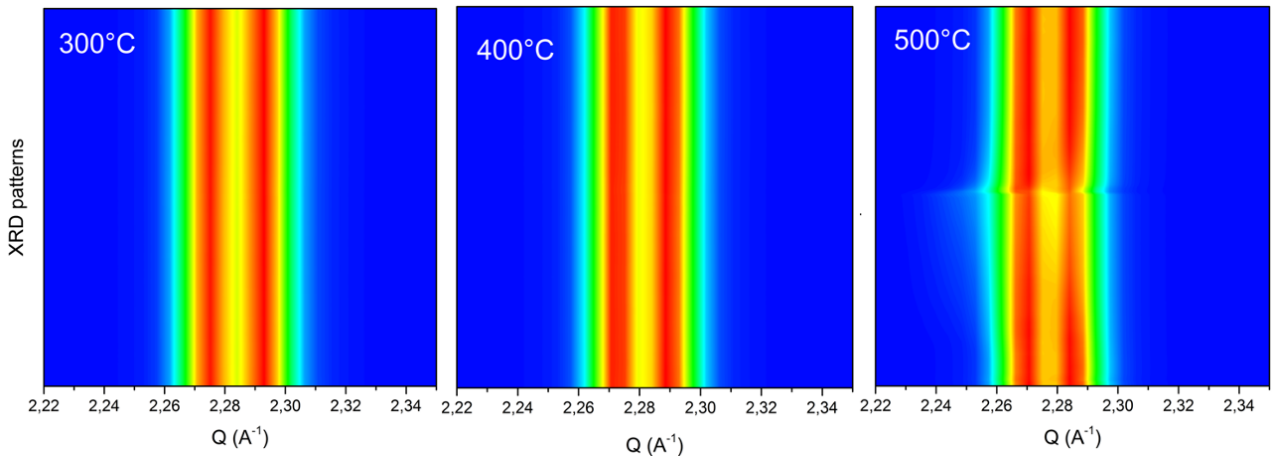

Figure 61 Main perovskitic peak of $LaCo_{0.5}Fe_{0.5}O_3$ during reducing (bottom half) and oxidizing (upper half) pulses. No visible structural changes occurred in this system.

6.3.2 A-doped $LaCoO_3$

Different doping was chosen for the A-site with strontium: plain $LaCoO_3$, $La_{0.8}Sr_{0.2}CoO_3$ and the half substitution, $La_{0.5}Sr_{0.5}CoO_3$. The incorporation of aliovalent cations in the perovskite lattice is an effective way to generate oxygen anion vacancies and thus to increase ion mobility and the catalytic activity. Vacancies are also responsible for the coordination and activation of reactants. As showed in Figure 60, different A-doping leads to a different CO_2 production, thus to different ability in incorporating oxygen into the lattice and surface. As stated before, the lanthanum substitution with strontium inside the lattice may produce the Increment of superficial vacancies, thus the overall Oxygen Storage Capacity.

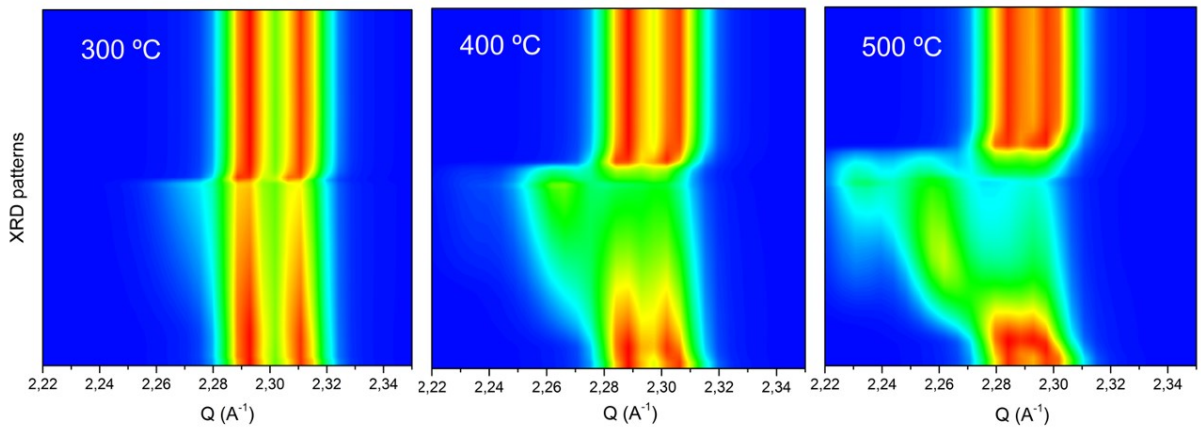

Figure 62 Main perovskitic peak of $LaCoO_3$ during reducing (bottom half) and oxidizing (upper half) pulses. Great visible structural changes occurred in this system, with the formation of a new phase.

Figure 62 displays 2D plots of the CO-O_2 pulse experiments on $LaCoO_3$ around the main doublet of the rhombohedral structure ((110) and (104) reflections). These experiments allowed to identify two regimes of temperatures where different extents of structural changes occur. Below 300°C, CO extracts oxygen atoms from the surface of the material. While no evident Q changes can be observed, the behaviour of the reflections suggests

reversible expansion/contraction of the lattice upon removal of oxygen by CO. Above 300°C, oxygen removal increasingly generates new reflections at lower angles belonging to the $La_3Co_3O_8$ brownmillerite structure [16], an oxygen deficient perovskite-related oxide. At 500 °C, it is clear that the rhombohedral structure of $LaCoO_3$ was completely lost in the CO pulse for ca. 2-3 s, however it was restored in the O_2 pulse. The appearance of the reflection at ca. 2.23 Å revelled the formation of the $La_2Co_2O_5$ phase [17], also an oxygen deficient perovskite-related structure. Despite these experiments, which removed the perovskite-type structure shortly, XRD data taken at every temperature before and after the pulse sequences indicate that the material did not lose substantial crystallinity.

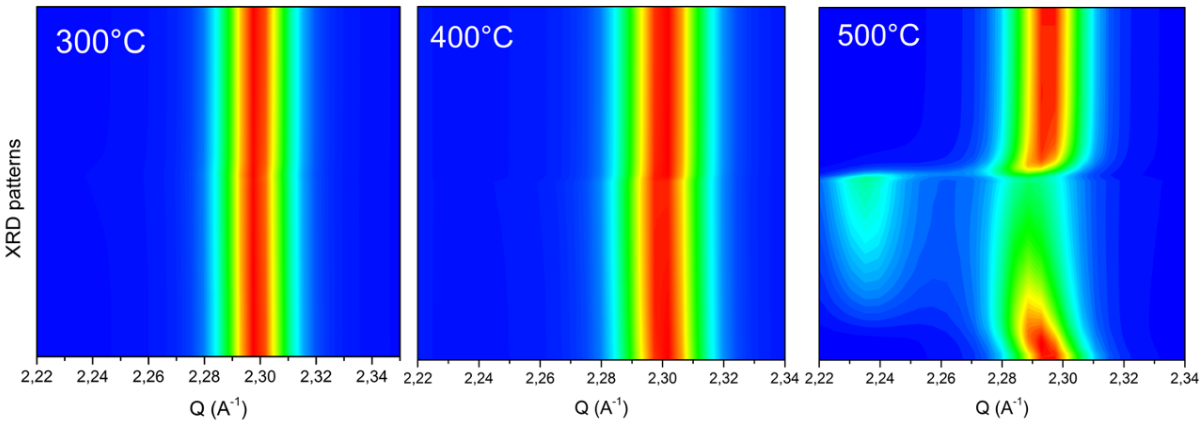

Figure 63 Main perovskitic peak of $La_{0.8}Sr_{0.2}CoO_3$ during reducing (bottom half) and oxidizing (upper half) pulses. Visible structural modification during reducing pulses only above 400 ºC.

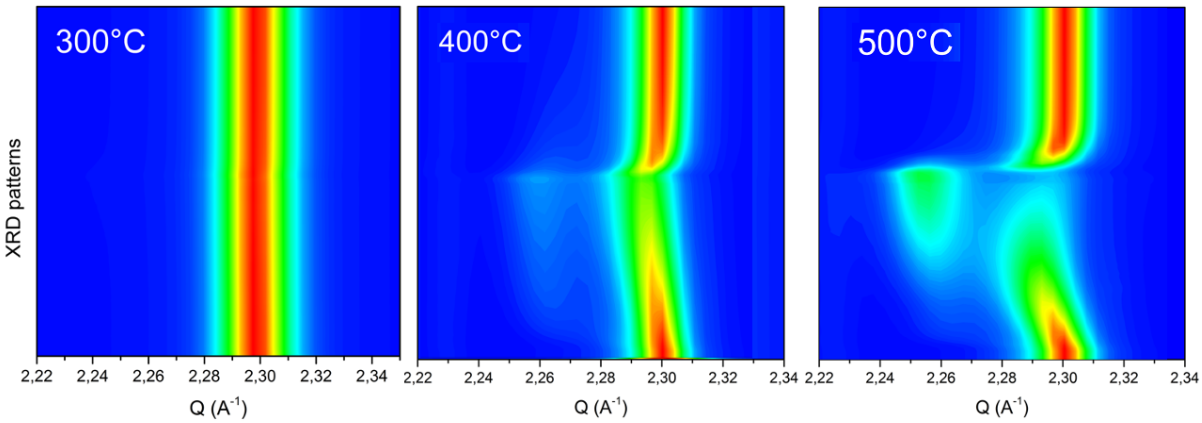

Figure 64 Main perovskitic peak of $La_{0.5}Sr_{0.5}CoO_3$ during reducing (bottom half) and oxidizing (upper half) pulses. Increasing the Sr content decrease the temperature reduction.

Substitution of La by 20% Sr (Figure 63) exhibited lower reducibility at low temperature and practically started to show structural changes only above 400°C. $La_{0.5}Sr_{0.5}CoO_3$ (Figure 64) exhibited less reduction propensity than $LaCoO_3$ at equal temperature suggesting that reducibility is not linear with Sr substitution.

With the new information from the *in situ* XRD is possible to link them to the MS. From the mass spectroscopy analysis it is possible to estimate the ability of the system $LaCoO_3$, and the Sr-doped perovskites, to oxidize the CO and correlating the data to the oxygen storage capacity. In Figure 65 is possible to see the OSC as function of Sr substitution at the three different temperatures.

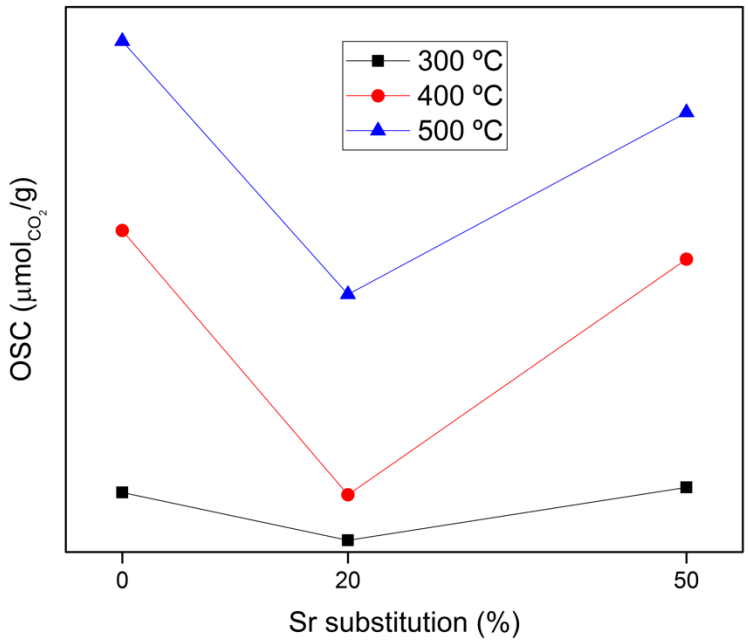

Figure 65 Oxygen Storage Capacity as function of the strontium substitution in $LaCoO_3$.

Moving from the un-doped system $LaCoO_3$ to the 20 % Sr substitution, the XRD data showed less reducibility, thus less ability to change during the reducing pulses. A possible explanation could be the changing of the crystallographic structure, in this case from the rhombohedral un-doped perovskite to the orthorhombic Sr-substituted. In this case, the only 20% of strontium inside the structure does not allow to maintain the same reducibility with the consequence of losing the ability to store oxygen, even at high temperature. Increasing the Sr content up to 50%, the system maintains the same crystallographic structure but the ability to create more surface vacancies permits to increase again the total OSC.

From the observation of this interesting new data, someone could state that the best OSC materials tested is the un-doped $LaCoO_3$, thanks to its good ability to reduce itself. The more accurate answer is: in which particular application the materials is needed? If the application required high working temperature, as a Fuel Electrode in SOC technology, the un-doped system $LaCoO_3$ is the worst choice due to its "softness" under reducing environment and high

temperature. The best choice will be the system with the 50% of Sr, that unified good OSC properties and strong structural behaviour under reducing environment.

6.4 Conclusion

The experiments showed in this chapter were devoted to the study of the reversible structural properties of selected perovskite-type oxides to redox pulsing as a function of temperature. This behaviour is closely related to catalytic properties. Four samples were fully characterized in this respect using high energy X-ray diffraction at beamline ID15A (ESRF): $LaCoO_3$, $La_{0.8}Sr_{0.2}CoO_3$, $La_{0.5}Sr_{0.5}CoO_3$ and $LaCo_{0.5}Fe_{0.5}O_3$ that are used as potential automotive exhaust catalysts or Electrode in SOC application.

The system $LaCo_{0.5}Fe_{0.5}O_3$ did not change from the structural point of view. From the *in situ* XRD data is clear that, during the CO oxidation reaction, no visible structural changes occurred. No other structural recombination was seen as possible precursor towards the CO evolution in CO2.

Different doping was chosen for the A-site with strontium: $LaCoO_3$, $La_{0.8}Sr_{0.2}CoO_3$ and $La_{0.5}Sr_{0.5}CoO_3$. Below 300°C, CO extracts oxygen atoms from the surface of the material. Above 300°C, oxygen removal increasingly generates new reflections at lower angles belonging to the $La_3Co_3O_8$ brownmillerite structure and at ca. 2.23 Å revelled the formation of the $La_2Co_2O_5$ phase.

Different Sr substitution led to different OSC properties, and the behaviour is not linear: the undoped $LaCoO_3$ showed the highest OSC performance but also the highest reducibility. If the application needs a stronger system able to resist at higher temperature, Sr substitution is fundamental, and its content will modify the OSC properties of the perovskite.

6.5 Bibliography

[1] M. A. Peña and J. L. G. Fierro, "Chemical structures and performance of perovskite oxides," *Chem. Rev.*, vol. 101, no. 7, pp. 1981–2017, 2001.

[2] A. Petric, P. Huang, and F. Tietz, "Evaluation of La–Sr–Co–Fe–O perovskites for solid oxide fuel cells and gas separation membranes," *Solid State Ionics*, vol. 135, pp. 719–725, 2000.

[3] M. Pacella *et al.*, "PGM-free CuO/$LaCoO_3$ nanocomposites: New opportunities for TWC application," *Appl. Catal. B Environ.*, vol. 227, no. November 2017, pp. 446–458, 2018.

[4] C. Zhou *et al.*, "NO oxidation catalysis on copper doped hexagonal phase $LaCoO_3$: A combined experimental and theoretical study," *Phys. Chem. Chem. Phys.*, vol. 16, no. 11, pp. 5106–5112, 2014.

[5] D. Ferri *et al.*, "Revealing the Dynamic Structure of Complex Solid Catalysts Using Modulated Excitation X-ray Diffraction," *Angew. Chemie*, vol. 126, no. 34, pp. 9036–9040, 2014.

[6] I. Alxneit, A. Garbujo, G. Carollo, D. Ferri, and A. Glisenti, "CuO/$La_{0.5}Sr_{0.5}CoO_3$: Precursor of efficient NO reduction catalyst studied by: Operando high energy X-ray diffraction under three-way catalytic conditions," *Phys. Chem. Chem. Phys.*, vol. 22, no. 34, pp. 18798–18805, 2020.

[7] Y. Lu *et al.*, "Operando XANES study of simulated transient cycles on a Pd-only three-way catalyst," *Catal. Commun.*, vol. 39, pp. 55–59, 2013.

[8] J. E. Tasca, C. E. Quincoces, A. Lavat, A. M. Alvarez, and M. G. González, "Preparation and characterization of $CuFe_2O_4$ bulk catalysts," *Ceram. Int.*, vol. 37, no. 3, pp. 803–

812, 2011.

[9] C. Marcilly, P. Courty, and B. Delmon, "Preparation of highly dispersed mixed oxides and oxide solid solutions," *J. Am. Ceram. Soc.*, vol. 53, no. 1, p. 56, 1970.

[10] N. Ni, S. J. Cooper, R. Williams, N. Kemen, D. W. McComb, and S. J. Skinner, "Degradation of (Lao.6Sro.4)o.95(Coo.2Feo.8)O3-δ Solid Oxide Fuel Cell Cathodes at the Nanometer Scale and below," *ACS Appl. Mater. Interfaces*, vol. 8, no. 27, pp. 17360–17370, 2016.

[11] M. Liu, M. Liu, D. Ding, K. Blinn, X. Li, and L. Nie, "Enhanced performance of LSCF cathode through surface modification," *Int. J. Hydrogen Energy*, vol. 37, no. 10, pp. 8613–8620, 2012.

[12] E. Zhao, Z. Jia, L. Zhao, Y. Xiong, C. Sun, and M. E. Brito, "One dimensional La 0.8Sr 0.2Co 0.2Fe 0.8O 3-δ/Ce 0.8Gd 0.2O 1.9 nanocomposite cathodes for intermediate temperature solid oxide fuel cells," *J. Power Sources*, vol. 219, pp. 133–139, 2012.

[13] R. A. De Souza and I. C. Fullarton, "Surface exchange of oxygen in mixed conducting perovskite oxides," *Solid State Ionics*, vol. 86–88, pp. 703–709, 1996.

[14] M. Oishi, K. Yashiro, K. Sato, J. Mizusaki, and T. Kawada, "Oxygen nonstoichiometry and defect structure analysis of B-site mixed perovskite-type oxide (La, Sr)(Cr, M)O3-δ (M=Ti, Mn and Fe)," *J. Solid State Chem.*, vol. 181, no. 11, pp. 3177–3184, 2008.

[15] K. T. C. Roseno, R. Brackmann, M. A. da Silva, and M. Schmal, "Investigation of LaCoO3, LaFeO3 and LaCoo.5Feo.5O3 perovskites as catalyst precursors for syngas production by partial oxidation of methane," *Int. J. Hydrogen Energy*, vol. 41, no. 40, pp. 18178–18192, 2016.

[16] P. Lacoo, "In situ X-ray powder diffraction study on flame-made undoped LaCoO3," pp. 567–568.

[17] O. H. Hansteen, "Crystal structure, thermal and magnetic properties of La Co O . Phase relations for LaCoO 3–d at 673 K," *J. Mater. Chem.*, pp. 3–10, 2007.

Chapter 7

"I shall either find a way or make one."

Hannibal

In the final chapter I would like to resume the technologies and strategies presented in this thesis that were chosen as possible solutions for a sustainable development: from the energy conversion to the air pollution. The aim is in demonstrating that smart strategies in defining composition, nano-composition, and structure can allow to obtain high performant heterogeneous catalysts that result disrupting in different field: the preferred application sectors are Solid Oxide Cells (SOCs) and Three Way Catalysts (TWCs).

First, SOCs have been illustrated with the aim to show how this technique is extremely efficient to transform chemical energy into electrical energy (Fuel Cell mode) and vice versa (Electrolyzer mode). From thermodynamics fundamental to the state of the art of the materials: a short walk to eventually, try to answer the question of why this incredible technology deserves to be investigated. From energy transformation to air pollution dilemma, the thesis describes the TWCs. This technology is fundamental to avoid harmful emissions from vehicles based on internal combustion engine. Nowadays it seems the rising age of electric car but the problems behind the use of batteries are significant. The Fuel Cell technology it is not a ready on market technology but can be helpful to solve the problems related to the save disposal of batteries. Moreover, the technology behind TWCs can be an extremely useful starting point to develop new materials which can be used in different applications (abatement of exhausts in stable plants, development of catalyst for highly demanding application). As a general consideration, the operative conditions for catalysts in TWC are usually more demanding than those required in stable plants: the know-how developed in the last 50 years can be extremely helpful to enrich the database of new materials that can benefit from an oscillating dis-equilibrium to perform in a better way and to exploit synergic mechanisms in complex reactions.

Two main aspects unify the research presented in this thesis: the care for environment and the idea of developing innovative materials by slight and careful modification of two Poly Cationic Oxides: spinel and perovskite systems. Care of environment: to demonstrate that progress is sustainable, that energy can be converted minimizing the generation of pollutants.

At first why are these catalysts preferred in this thesis? Spinel and perovskites are crystallographic structures tremendously simple but is a smart way elaborated by nature to arrange metal ions. It is possible to bestow to spinel and perovskite the specific behavior that a specific application need, adjusting with craftiness the composition. More important, it is possible to elaborate a starting material that can completely change his catalytic behavior, transforming itself in a new in situ catalyst.

In Chapter 3, $CuFe_2O_4$, $CuFeAlO_4$ and $CuAl_2O_4$ spinel materials were proposed as active and stable catalysts for the catalytic hydrogenation of CO_2 to CO, also known as the Reverse Water Gas Shift (RWGS) reaction. In this chapter, the activity of spinel oxides as catalysts for this reaction was investigated as a function of aluminum content. $CuFeAlO_4$ outperformed all other spinels studied in the range of temperatures (100 ºC–600 ºC). Further investigation of the catalysts with *in situ* XRD showed that $CuFeAlO_4$ spinel is the most balanced under reducing environment: enough to allow the Cu extraction without losing its structural integrity. Furthermore, XAS measurements of as-synthesized and activated spinel showed the presence of Cu^{1+} as amorphous phase, a good candidate as promoter for the CO_2 activation during RWGS. In all the cases, the activation process reveled the increasing of the performance due to the Cu extraction from the lattice. The key factor is the presence ($CuFeAlO_4$ – $CuAl_2O_4$) or not ($CuFe_2O_4$) of aluminum and its quantity. Indeed, the initial

synthesis of the catalyst is crucial to provide the desired properties. In spite of this, it is only by means of the combination of synthesis and reaction process that is possible to optimize the desired behavior.

In Chapter 4, different crystallographic structures containing Fe and Cu, inside *vs* supported on the surface, were proposed as active catalysts towards Three Way Catalyst reaction. The foundation and the question that drove this research was the following: "*are pulses conditions useful to activate the catalyst in TWC application?*" The answer is yes, but some precaution must be taken in account. Spinel system $CuFeAlO_4$, for its nature and composition, showed a remarkable ability towards the NO abatements only during pulses condition. During static condition, only CO was oxidized to CO_2. Different behavior was pointed out from the perovskitic system $LaFeO_3$: in the scenario where only the perovskite was used as catalyst, poor TWC performances were achieved, especially versus the NO. If the system is enriched with copper nanoparticles, thanks to the ability of copper to change easily through $Cu^{2+} \leftrightarrow Cu^{1+} \leftrightarrow Cu^{0}$, TWC performance is boosted reaching almost the 100 % of NO conversion at 450 ºC. Unfortunately, FT-IR measurements showed the presence of ammonia in the exhaust gases, probably caused by the slightly reducing condition used ($0 < \lambda < 0.9$).

In Chapter 5, the electrochemical characterization of the two spinels $CuFe_2O_4$ and $CuFeAlO_4$ was carried out. The system with only aluminum inside the lattice, $CuAl_2O_4$, was not considered due to its very low reducibility, thus performance in the water gas shift reaction as presented in Chapter 3. The two spinels were studied by means of the Electrochemical Impedance Spectroscopy probing throughout temperature variation and different fuel gases such hydrogen and carbon monoxide. In the previous Chapters 3 and 4, the ability of the two

system to reduce under hydrogen was evaluated and related to the aluminum content. Further investigation of the catalysts with *in situ* XRD showed that $CuFeAlO_4$ spinel is the most balanced under reducing environment: enough to allow the Cu extraction without losing its structural integrity. Furthermore, XAS measurements of as-synthesized and activated spinel showed the presence of Cu^{1+} as amorphous phase, a good candidate as promoter for the CO_2 and CO activation during RWGS and other reactions, such as those required in TWC. In all the presented cases, the activation process revelled the increasing of the performance due to the Cu extraction from the lattice. The key factor is the presence ($CuFeAlO_4$) or not ($CuFe_2O_4$) of aluminium and its quantity.

Table 10 Summary of the ASR values of $CuFe_2O_4$ and $CuFeAlO_4$ with H_2.

Temperature (°C)	600	650	700	750	800
$CuFe_2O_4$/YSZ/$CuFe_2O_4$ ASR (Ωcm^2) 10% wet H_2/Ar	64.44	29.85	16.13	6.85	3.93
$CuFeAlO_4$/YSZ/$CuFeAlO_4$ ASR (Ωcm^2) 10% H_2 wet/Ar	11.34	5.92	3.41	2.25	1.69

The same results were obtained in the electrochemical investigation, where the $CuFeAlO_4$ spinel overcome the $CuFe_2O_4$ performance, at all temperatures and with all the gases studied, Table 7 and Table 8.

Table 11 Summary of the ASR values of $CuFe_2O_4$ and $CuFeAlO_4$ with H_2 + CO.

Temperature (°C)	600	650	700	750	800
$CuFe_2O_4$/YSZ/$CuFe_2O_4$ ASR (Ωcm^2) 10% H_2 10% CO wet/Ar	38.34	20.27	9.97	4.35	2.74
$CuFeAlO_4$/YSZ/$CuFeAlO_4$ ASR (Ωcm^2) 10% H_2 10% CO wet/Ar	6.59	3.83	2.37	1.70	1.31

The ability of $CuFeAlO_4$ to maintain its structure beside the Cu extraction is the reason of its good activity, also toward the CO oxidation. In the course of the thesis it was showed how the Bode plots change with CO presence, a behavior confirmed by the appearing of a new process. In the spinel without aluminum ($CuFe_2O_4$) this peculiarity was not present because the system was not able to maintain the crystallographic structure intact at high temperature, thus its inability to activate and catalyze the CO oxidation. Another fact supporting this hypothesis is the activation energy of the cells studied in this thesis. In the cells containing the spinel with aluminum, the activation energies are lower compared to the spinel $CuFe_2O_4$. Moreover, the $CuFe_2O_4$ system presents almost the same activation energy (Table 9) with and without the presence of CO, as another confirmation that the system does not have sufficient stability to maintain the active site towards CO oxidation. On the contrary, the spinel with aluminum showed different activation energy and different ASR

with H_2 and CO. In this case, the structural integrity allowed by the presence of Al inside the structure, permits the system to maintain the active site for the CO oxidation and, furthermore, increments the performance.

Table 12 Activation energies of the tested cells with different gases and electrodes composition.

Sample (fuel)	Activation energy (eV)
$CuFe_2O_4$/YSZ (H_2)	1.14
CuFe2O4/YSZ (H_2 + CO)	1.10
$CuFeAlO_4$/YSZ (H_2)	0.77
$CuFeAlO_4$/YSZ (H_2 + CO)	0.66

In the last Chapter 6, the experiments showed were devoted to the study of the reversible structural properties of selected perovskite-type oxides to redox, pulsing as a function of temperature. This behaviour is closely related to catalytic properties. Four samples were fully characterized in this respect using high energy X-ray diffraction at beamline ID15A (ESRF): $LaCoO_3$, $La_{0.8}Sr_{0.2}CoO_3$, $La_{0.5}Sr_{0.5}CoO_3$ and $LaCo_{0.5}Fe_{0.5}O_3$ that are used as potential automotive exhaust catalysts or Electrode in SOC application.

The system $LaCo_{0.5}Fe_{0.5}O_3$ did not change from the structural point of view. From the *in situ* XRD data is clear that, during the CO oxidation reaction, no visible structural changes occurred. No other structural recombination was seen as possible precursor towards the CO evolution in CO2.

Different doping was chosen for the A-site with strontium: $LaCoO_3$, $La_{0.8}Sr_{0.2}CoO_3$ and $La_{0.5}Sr_{0.5}CoO_3$. Below 300°C, CO extracts oxygen atoms from the surface of the material. Above 300°C, oxygen removal increasingly generates new reflections at lower angles

belonging to the $La_3Co_3O_8$ brownmillerite structure and at ca. 2.23 Å revelled the formation of the $La_2Co_2O_5$ phase.

Different Sr substitution led to different OSC properties, and the behaviour is not linear: the undoped $LaCoO_3$ showed the highest OSC performance but also the highest reducibility. If the application needs a stronger system able to resist at higher temperature, Sr substitution is fundamental, and its content will modify the OSC properties of the perovskite.

As a general consideration the results obtained in this thesis fully demonstrate that the development and optimization of the materials is a process similar to the creation of a artwork: creativity and skill are placed on the palette and the scientist uses them to obtain a material with the desired behaviour.

List of Figures

Acknowledgments

2018 was the year when I started my PhD adventure. Everything that is alive, whether we want it or not, has an end. This is the conclusion of three years that gave me the opportunity to increase my scientific knowledge and gave me the chance to evolve as a human being. Me and my XXXIV cycles PhD mates will always be remembered as PhD students of the COVID-19. I endured for several months from being infected but, as a twist of fate, I resulted positive during the final drafting of the thesis. As a side effect of this disease, I completely lost the sense of taste and smell. Trust me, it is frustrating trying to eat and enjoy a simple orange and feel… nothing at all! This uncommon situation made me think of how important the flavors and fragrances are, in general: it is the taste of a particular food that conquers our heart, it is the perfume of a peculiar flower that allows us to remember that special experience… Normally we take them for granted but what would our life be without flavors and fragrances?

In these three years of PhD, there were some outstanding people who gave flavor to my experience, who spent their time helping or just sharing some pieces of their life with me.

My biggest acknowledgment is to Prof. Antonella Glisenti, who gave me the opportunity of creating my own path using her knowledge and wisdom. I am profoundly grateful to Antonella for giving me that freedom (always under her wing) which empowered me to grow in the scientific field. She has been both a mentor and a role model in many ways and I feel privileged to have worked alongside her.

I sincerely thank Dr. Davide Ferri, for giving me the opportunity to work in his group, for being a friendly and incredibly prepared supervisor during the countless chances that he gave to me. Most of my scientific experiences were possible only thanks to his kindness, open mind, and ability to see beyond the mere position.

A profound source of inspiration during the Ph.D. period, was the passion that drives Stefano Mercanzin in the challenges that he must face day by day. All my knowledge in the mechanics field, in the pragmatic part of the scientific world, is thanks only to him. I am grateful for all the moments shared with me, talking about science and life.

Walking alone is possible but together is way better. The IMPACT group will always be part of me, and I will always be part of the IMPACT group. Like dissolve like so the IMPACT group is composed of people as great as Antonella. My acknowledgment goes to Enrico, a brilliant future Dr. whose determination, friendship, and perseverance helped me during these years. I am sincerely thankful to Simone, another future Dr. who helped me with the electrochemical measurements and share with me the most stupid and expensive hobby. I would like to thank Dr. Elena that every day bringing calm and politeness to labs and the office. My gratitude to Dr. Giacomo, the "long date colleague", for the countless

opportunities of discussion that, in time, evolved in dialogue. And thanks to Jonny and Lorenzo, the future of the IMPACT group is on their robust shoulders.

If the goodness of a group is directly correlated to its supervisor, the ACS group at the PSI is not an exception. I am truly grateful to Filippo, Maneka, Miren, Dominik, Ivo and Martin. Every member of Davide's group accepted me as a "true" Swiss man!

Many thanks go to the beam scientists that helped me during measurements: the continuous support by Dr. M. Di Michiel, Dr. S. Checchia, and the team of the beamline ID15 at the ESRF is greatly appreciated; thanks to the team at SuperXAS beamline located in the Swiss Synchrotron Light Source, in particular to Dr. Adam Clark.

From the bottom of my heart, I would like to thank my family: my Mamma, my Papà, and my brother Paolo for always believing in me no matter what. My passion and devotion to science would not have been possible without their continuous encouragement. Grazie.

I am profoundly grateful to my second family for sharing with me the same path. Thanks, Elia for being you, thanks to Giacomo, Bruno, Giulia, and Grace for helping me with your presence and brotherhood, thanks *Alessia* for dancing with me like two parallel lines, thanks to Agne, Angelica, Anna, Deiv, Jack, Irene, Luca, Marty, Tommy, Nicola e Henry. The sun will rise again.

Thanks to all the people who took different paths in these three long years.